Degree project in Physical Geography and Quaternary Geology

Stockholms universitet

Twelve Years of Slush and Supraglacial Lakes On Petermann and C.H. Ostenfeld Glaciers from Supervised Classification

Luke Urso

Master's level 60 HE credits autumn term 2025–spring term 2026

Twelve Years of Slush and Supraglacial Lakes On Petermann and C.H. Ostenfeld Glaciers from Supervised Classification

Luke Urso

Department of Physical Geography
Examensarbete i naturgeografi och kvartärgeologi 60 HE credits (GE9011)
Series:
Masters programme in Polar Landscapes and Quaternary Climate (120 HE credits)
Autumn term 2025–spring term 2026
Supervisors: Nina Kirchner; Abhay Prakash
Examiner: Margareta Hansson
Assessor: Qiong Zhang

Cover photo: West Antarctic Peninsula (2020). Photo: Luke Urso

Stockholms universitet

Abstract

Supraglacial meltwater collects as slush and supraglacial lakes on Greenland's northern outlet glaciers and is a key control on the region's accelerating mass loss. Petermann Glacier hosts one of the largest remaining ice tongues in northern Greenland, while the ice tongue of neighboring C.H. Ostenfeld Glacier collapsed in 2003. Despite this, comparative study of these glaciers remains a gap in the literature, and no detailed inventory of surface meltwater on Ostenfeld exists. Here, a random-forest classifier is adapted from Antarctic ice-shelf methods and combined with a physically based lake-volume formulation to map supraglacial lake and slush area, lake-feature elevation, lake volume, and rapid drainage events on Petermann and Ostenfeld glaciers. Classification is carried out for twelve melt seasons (2014–2025) using Landsat 8/9 imagery composited into 2-day windows. The classifier returns 90.2% overall accuracy ($\kappa = 0.85$; macro $F_1 = 0.90$) across 2,556 unseen holdout pixels. Melt area displays strong interannual variability, exceeding baselines by factors of 13.3 at Petermann and 4.8 at Ostenfeld, with both glaciers experiencing peak area anomalies in 2023. Slush is the dominant area component, with median slush-to-lake ratios of 8.8 at Ostenfeld and 4.9 at Petermann. At Petermann, lake-maximum area, elevation, and volume share Pettitt change points between 2017 and 2020, concurrent with grounding-zone retreat and rising velocity. In 2024, despite a near-baseline melt area, Petermann produced the highest aggregate drainage volume (34.5 Mm^3) and the highest full-drainage count on record, reflecting 2023 melt carryover effects. JJA single-day peak 2 m air temperature accounts for 85% ($R^2 = 0.85$) of the year-to-year variance in Petermann combined-maximum area but only 25% ($R^2 = 0.25$) at Ostenfeld, while seasonal-mean temperature and downwelling shortwave are weak predictors at both, consistent with melt driven by short warm excursions on a cold-mean state at Petermann. The present work contributes the first detailed slush-area and lake-volume dataset for Ostenfeld Glacier. This study shows that surface-state carryover explains part of the divergence in surface-melt response under similar climate forcing.

Key words

Contents

Abbreviations

79N	Nioghalvfjerdsfjorden Glacier
AOI	Area of interest
CRS	Coordinate reference system
CV	Coefficient of variation
DEM	Digital elevation model
DOY	Day of year
EE	Google Earth Engine
EPSG	European Petroleum Survey Group (geodetic parameter dataset identifier)
ERA5	ECMWF Reanalysis 5
FAC	Firn air content
GrIS	Greenland Ice Sheet
JJA	June–July–August
MEaSUREs	Making Earth System Data Records for Use in Research Environments
MK	Mann–Kendall
$NDWI_{(ice)}$	Normalised difference water index over ice
NGrIS	North Greenland Ice Sheet (northern sector of the GrIS)
NSIDC	National Snow and Ice Data Center
OLS	Ordinary least squares
Ost, OST	C.H. Ostenfeld study area (abbrev.)
PFA	Perennial firn aquifer
Ptm, PTM	Petermann Glacier (abbrev.)
QA_Band	Quality Assessment Band
R^2	Coefficient of determination
RCP	Representative Concentration Pathway
RF	Random forest
RGB	Red–green–blue
SGL	Supraglacial lake
SLR	Sea-level rise
TOA	Top of atmosphere
WGS	World Geodetic System

1 Introduction

The Greenland Ice Sheet (GrIS) is the largest cryosphere contributor to global mean sea level rise (SLR) (Mouginot et al., 2019) and mass loss has accelerated in the last four decades (Mouginot et al., 2019; Khan et al., 2020). The northern sector of the GrIS (NGrIS) drains 40 % of the ice sheet by area and has experienced an accelerating mass loss regime over the last three decades (Hill et al., 2017; Rignot et al., 1997). Recent estimates put the NGrIS mass loss at 474 ± 30 Gt or 1.3 ± 0.1 mm in 2010–2018 (Mouginot et al., 2019), with eight of eight surveyed northern ice shelves showing widespread thinning, basal-melt acceleration, and grounding-line retreat (Millan et al., 2023; Wilson et al., 2017).

Surface meltwater is a major control on dynamic mass loss through (i) structural weakening via full column hydrofracture (Weertman, 1969; Benn et al., 2007; Scambos et al., 2009; Lai et al., 2020), (ii) injection of meltwater to the base through the rapid drainage of supraglacial lakes (Das et al., 2008; Banwell et al., 2013; Chudley et al., 2019; Christoffersen et al., 2018), (iii) and subglacial discharge of surface runoff through the grounding zone (Prakash et al., 2025; Washam et al., 2020; Cai et al., 2017), among other factors. Supraglacial lakes (SGLs) form when meltwater collects in topographic depressions on the glacier surface and are the dominant surface meltwater feature by volume (Moussavi et al., 2016; Dell et al., 2022); whereas slush (water saturated firn that has been wetted enough to lose its dry optical and thermal properties without forming a coherent surface pond) is the dominant surface melt feature by area (Dell et al., 2024; Glen et al., 2025b).

Petermann Glacier is a major marine terminating outlet glacier in the NGrIS and hosts one of the largest remaining ice shelves in the Northern Hemisphere (Münchow et al., 2014). Neighboring C.H. Ostenfeld Glacier lost its floating ice tongue in 2002–2003, and the drivers and long-term impacts of that collapse remain a gap in the literature (Hill et al., 2017).

1.1 Project Aims

The goal of the present work is to characterize supraglacial lake and slush area, elevation, lake volume, and lake-drainage events on Petermann and Ostenfeld glaciers during the 2014–2025 melt seasons to contribute to an improved understanding of NGrIS outlet glacier dynamics. This project will use the generated melt response data to achieve the following aims.

(i) Characterize inter-annual variability, multi-year structural shifts, and contrast the surface-meltwater dynamics of the study glaciers using June-July-August (JJA) mean and maximum melt response timeseries.

(ii) Report the spatial and temporal distribution of rapid lake-drainage events, and their volume.

(iii) Quantify melt response relationship to ERA5-Land 2 m air temperature and downwelling shortwave forcing.

(iv) Characterize the asymmetry in climate sensitivity between Petermann and Ostenfeld.

1.2 Thesis structure

The remaining sections take the following structure. The Background section presents the relevant literature on Greenland Ice Sheet mass loss, surface meltwater processes, Greenland floating ice tongues and subglacial discharge, and firn state. The Study Area section introduces Petermann and Ostenfeld glaciers. The Methods section sets out the remote-sensing data and the classification, volume-retrieval, and analysis workflow. The Results section reports the mapped catalogue, melt-area and lake-volume timeseries, anomaly and climate-forcing analyses, spatial structure of melt, and lake-drainage events. The Discussion interprets the results, defends the methodology, and revisits the four aims in a final Conclusions subsection.

2 Surface melt and mass loss

The GrIS contributed 13.7 $\pm$ 1.1 mm ($\approx$ 4930 $\pm$ 400 Gt) to global mean SLR between 1972 and 2018 (Mouginot et al., 2019). Mass loss has accelerated sixfold over that interval, from a near-balance gain of 47 ± 21 Gt yr^{-1} in 1972–1980 to a loss of 286 ± 20 Gt yr^{-1} in 2010-2018, with 66 $\pm$ 8 % of that attributed to glacier dynamics and 34 $\pm$ 8 % to surface mass balance (Mouginot et al., 2019; Khan et al., 2020). The dynamic component is concentrated at marine-terminating outlet glaciers, where fast-flowing fringe ice ($>$ 100 m yr^{-1}) thinned at 0.84 m yr^{-1} against 0.12 m yr^{-1} for slow-flowing ice in the same climatic setting (Pritchard et al., 2009; Joughin et al., 2010; Box and Decker, 2011). Under RCP 8.5, the largest marine terminating outlet glaciers are projected to add 9.1 to 14.9 mm by 2100 (Khan et al., 2020; Mouginot et al., 2019). Ocean thermal forcing of the marine-terminating margins is noted as a key driver of this change (Straneo and Heimbach, 2013; Cowton et al., 2018; Box and Decker, 2011; Washam et al., 2018). The role of surface meltwater processes represents an additional, increasingly documented control which motivates the present work.

2.1 Supraglacial lakes and slush

Meltwater from slush or supraglacial lakes at the surface increases both the likelihood of fracture initiation and the depth to which a fracture will propagate in a water-filled crevasse, the process of which is described mechanically as hydraulically assisted fracture, or hydrofracture (Weertman, 1969; Van Der Veen, 1998; Benn et al., 2007; Lai et al., 2020). Surface meltwater has been observed to propagate hydrofractures through the ice column and rapidly drain supraglacial lakes to the bed on a scale of hours (Das et al., 2008; Christoffersen et al., 2018; Chudley et al., 2019).

2.1.1 Supraglacial lakes

SGLs are seasonal meltwater pools that form on glacier surfaces and have been mapped extensively on the GrIS (Williamson et al., 2018; Glen et al., 2025b; Miles et al., 2017). In recent decades, the frequency of rapid and coupled lake drainage has increased, and expansion inland and to higher elevations has been documented (Christoffersen et al., 2018; Otto et al., 2022; Zhou et al., 2025). At Ryder Glacier, a 35-year record (1985–2020) documents the first observed coupled lake-drainage event in 2002 and an increase in single-lake drainage event frequency from 2000 onward (Otto et al., 2022). William-

son et al. (2018) identify 184 rapid drainage events during the 2016 melt season on a 12,000 km^2 area of west Greenland. Rapidly draining small lakes (< 0.125 km^2) accounted for only 5.1% of the lake water volume released during drainage events, but were associated with 105 additional moulin openings and 61.5% of the total post-drainage runoff delivered through lake-opened moulins (Williamson et al., 2018).

Rapid lake drainage destabilizes local stress regimes. *In situ* observations of a rapid partial drainage at a fast flowing west Greenland outlet glacier, show that a 1.25 km^2 lake containing 7.3×10^6 m^3 of water delivered 4.8×10^6 m^3 to the bed in ~5 h at a peak discharge of 924 m^3 s^{-1} (Chudley et al., 2019). The meltwater injection uplifted the local ice surface by 0.55 m, and produced a short term surface-velocity increase from 2.0 to 5.3 m day^{-1} at ~ 4 km downstream of the basin (Chudley et al., 2019). The change to shear and tensile stress regimes causes ice flexure in a wide area around rapid drainages as the ice mass adjusts (Christoffersen et al., 2018). Drainage induce flexure can open transient surface-to-bed pathways triggering cascading drainage of other lakes as far as 80 km apart, at elevations as high as 2000 m a.s.l., and as far as 135 km from the ice margin (Christoffersen et al., 2018).

Christoffersen et al. (2018) modelled a 9000 km^2 Kangerlussuaq-sector domain forced by 156 lakes and 663 observed drainage events in 2010, representing 0.43 km^3 of water transferred to the bed. Individual cascading events involved up to 124 lakes draining over several days, with lakes as far as 80 km apart linked through stress perturbations. For one event on 21 June, 26 lakes transferred 21×10^6 m^3 of water to the bed, producing modelled surface-velocity increases of >5% over 4750 km^2 despite basal-traction reductions of >5% over only 233 km^2; i.e., drainage events provoke the adjustment of a wide area of the glacier to compensate for the mass vacuum left by accelerated ice downstream of the event (Christoffersen et al., 2018). This mechanism is consistent with the increasingly coupled drainage observed at Ryder Glacier, where lakes expanded 5-15 km inland and 90–280 m upward between 1985 and 2020 and where coupled drainage recurred in most years during 2010–2020 (Otto et al., 2022).

2.1.2 Slush

Slush (water-saturated firn or snow) forms where meltwater production exceeds vertical drainage into firn pore space, especially where near-surface impermeable layers, ice slabs, or firn aquifers limit percolation, and refreezing further reduces local permeability. Slush increases the likelihood of hydrofracture (Lai et al., 2020) and can increase firn density and thickness in low-permeability layers, reducing future storage capacity (Glen et al., 2025a,b). Dell et al. (2024) found that slush accounted for 57% of mean January meltwater area across all Antarctic ice shelves, and that including the lower albedo of slush and ponded water increased modelled snowmelt by a factor of 2.8 across five representative ice shelves.

Slush can occupy a significantly larger area of the GrIS than SGLs but displays high interannual variability. In a ~5800 km^2 area of Russell–Leverett catchment in southwest Greenland, slush remained minor in the low-melt 2018 season, reaching a peak area of ~10 km^2 on 25 July, but expanded rapidly in 2019 from 14.9 km^2 on 3 July to 466 km^2 on 1 August, a factor of ~47 larger than the 2018 peak (Glen et al., 2025b). Its elevation range also shifted upward between years, from 800–1700 m a.s.l. in 2018 to 1200–2000 m a.s.l. in 2019, with the maximum mapped slush elevation increasing by ~200 m (Glen et al., 2025b). At continent scale, mean summer slush coverage between 2016-

2024 is mapped at ~2.9% (~50,400 km^2) of the GrIS, with ~40% of that area occurring over low-permeability ice slabs or firn aquifers (Glen et al., 2025a). Maximum slush extent ranged from 1.2% of the GrIS (20,500 km^2) in 2018 to 5.2% (90,300 km^2) in 2019, and the mapped slush area was four to nine times greater than the combined area of supraglacial lakes and streams in the same years (Glen et al., 2025a).

2.1.3 Remote sensing of supraglacial lakes and slush

At the spatial resolution of long-term optical remote sensing catalogs (10 to 30 m for Copernicus and Landsat respectively), SGLs tend to present as dark, delineated, flat-surfaced features with short transition boundary zones. Water has low red/NIR/SWIR reflectance and, for shallow supraglacial water, relatively high blue/green reflectance (controlled by depth-dependent attenuation, see Sec. 4.5) (Philpot, 1989; Moussavi et al., 2016). Threshold-based SGL classification exploits the contrast between pooled water and the surrounding glacial substrate. In Greenland studies this is commonly implemented with NDWI or NDWIice (Normalized Difference Water Index modified for Ice) thresholds.

Note that while the literature generally agrees on standard NDWI wavelengths between ~0.50–0.60 μm (green) and ~0.70–1.10 μm (NIR), NDWIice does not enjoy the same universality and several variants exist. This project uses the term NDWIice to refer to the normalised difference of 0.450–0.515 μm (blue, LS-08, -09 band 2) and 0.640–0.670 μm (red, LS-08, -09 band 4), as published by Dell et al. (2022, 2024).

SGLs can be reliably extracted with index thresholds. Miles et al. (2017) use a high NDWIice threshold of > 0.5 to extract high confidence lake pixels, while Williamson et al. (2018), using a dual Sentinel-2/Landsat 8 approach, set an NDWIice threshold of 0.25. Similar threshold ranges are used in more recent work, such as Glen et al. (2025b) who classify lakes pixels using NDWI > 0.24 and NDWIice > 0.25. In large scale studies, multi-threshold approaches add explicit preprocessing steps to mask cloud, rock, snow, and shadow and reduce the high rate of false positive commission error associated with threshold based approaches. Threshold approaches suffer commission error when preprocessing fails to mask concomitants (e.g., cloud shadow, and debris covered ice) or when extracting transitional classes (e.g. shallow water, slush, wet snow, blue ice). Kang Yang and Smith (2013) show this directly for Greenland supraglacial streams, where a spectral-shape method achieved 85.2 % success in slushy areas compared with only 52.9 to 59.4 % for simple NDWIice threshold approaches.

Random forest (RF) machine-learning algorithms are demonstrated to be effective and adaptive classifiers of both slush and SGLs, while also suffering lower error-of-commission rates when scenes are multi-class with cloud, rock, and shadow contamination (Dell et al., 2022, 2024). Dell et al. (2022) trained an RF classifier for Antarctic ponded water and slush and obtained expert validation accuracies of 84 % and 82 %, respectively, finding that 64 % of Roi Baudouin Ice Shelf surface meltwater was slush and 36 % ponded water during 2013–2020. Scaling an RF approach with Sentinel-2 imagery, Glen et al. (2025a) reported overall accuracy of 97.5 % ($\kappa = 0.85$), and F1-scores of 98.6 % for slush and 86.4 % for non-slush, showing a slight overprediction bias. The ability of RF approaches to class both slush and lakes across mixed, minimally preprocessed scenes makes it suitable for automated, large-scale workflows.

2.2 Subglacial discharge at marine-terminating margins

Recent work has demonstrated that surface runoff amplifies submarine melting of NGrIS ice tongues when drained subglacially to the fjord, but modeled discharge estimates vary (Cai et al., 2017; Prakash et al., 2023; Washam et al., 2020; Slater et al., 2019). Surface runoff is surface melt drained to the bed and is the primary component (90%-95%) of subglacial discharge along with basal melt (Mankoff et al., 2020; Karlsson et al., 2021). Estimates of subglacial discharge from 136 GrIS tidewater glaciers by Slater et al. (2022) and Mankoff et al. (2020) show that of the five glaciers with the largest mean JJA subglacial discharge volume, four are northern Greenland outlet glaciers, three have experienced ice tongue collapse, and one retains its ice tongue (Table 1). These estimates assume that essentially all Modèle Atmosphérique Régional (MAR) and Regional Atmospheric Climate Model, version 2 (RACMO2) modelled surface melt reaches the bed instantly. This represents a routing-efficiency assumption not yet directly tested in the literature. The Slater et al. (2022) and Mankoff et al. (2020) estimates for Petermann are approximately two to three times larger than those referenced elsewhere in the present work by Prakash et al. (2025), and Ciracì et al. (2023). The difference in estimates highlights the need for observational controls on surface runoff magnitude.

Table 1. Five largest modeled mean summer subglacial discharge (Q_{sg}) estimates of 136 Greenland tidewater glaciers. Glaciers 4-5 are located in northern Greenland (Fig. 1). Data attribution: values are routed runoff-subglacial discharge estimates derived from the Mankoff et al. (2020) Greenland liquid water discharge dataset, used and published in Slater et al. (2022) for plume/upwelling calculations.

Rank	Glacier	Mean JJA Q_{sg}
1	Jakobshavn Isbræ	1283 $m^3 s^{-1}$
2	Petermann Gletscher	877 $m^3 s^{-1}$
3	Zachariæ Isstrøm	774 $m^3 s^{-1}$
4	Nioghalvfjerdsfjorden / 79N	691 $m^3 s^{-1}$
5	Humboldt Gletscher	475 $m^3 s^{-1}$

2.3 Firn state, FAC, and meltwater retention

The fraction of summer surface meltwater that ends up as ponded lake versus saturated slush versus refrozen ice within the firn pack is a function of the firn air content (FAC), the available pore space, and the firn temperature and density profile, i.e., the firn state, (Dell et al., 2024; Alley et al., 2018; Vandecrux et al., 2020). Perennial firn aquifers and low permeability ice slab are documented as firn-state responses to warming on the GrIS. Perennial firn aquifers (PFAs) are year-round liquid-water bodies within the firn that store meltwater at depths of 5 to 50 m and can feed meltwater to the subglacial system. They form from a combination of moderate to high surface melt and high annual accumulation supplying enough pore space at depth to keep liquid water below the winter cold wave (Munneke et al., 2014). Low-permeability ice slabs form via refreezing of percolating melt at the percolation-zone surface. Ice slabs covered 64 800 to 69 400 km^2 of the GrIS in 2014 and have expanded the GrIS total runoff area by 26 ± 3 % since 2001, and are projected to contribute 7 to 33 mm to global sea-level rise by 2100 under RCP4.5 and 17 to 74 mm under RCP8.5 (MacFerrin et al., 2019). Almost any transect from the GrIS coast to the interior crosses either an ice-slab region, an aquifer, or both (Brils et al., 2024). Dell et al. (2024) establishes a link between FAC and surface

melt partitioning (i.e., the ratio of slush to lake area), showing that ice shelves with FAC > 21 m are characterized with minimal ponding and dominant slush, shelves with FAC < 14 m show dominant ponding, and intermediate FAC produces mixed regimes.

3 Study area

Petermann and C.H. Ostenfeld glaciers are neighboring marine terminating outlet glaciers on the northernmost coast of the GrIS and are the study area of the present project (Fig. 1). The glaciers are separated by ~ 200 km, terminating in adjacent fjord systems in the north-central NGrIS sector under broadly comparable Arctic-Atlantic forcing. Petermann retains a ~ 48 km floating tongue while Ostenfeld lost its tongue in 2002–2003 and has not recovered (Münchow et al., 2016; Millan et al., 2023). The following section offers an overview of the regional context followed by the relevant knowledge base of each glacier.

3.1 Regional Context

The northern sector of the Greenland Ice Sheet (NGrIS) contains four of the largest marine-terminating outlet glaciers on the GrIS (Petermann, Nioghalvfjerdsfjorden / 79N, Ryder, and C.H. Ostenfeld), together draining ~ 12 % of the GrIS (Hill et al., 2017; Rignot et al., 1997; Münchow et al., 2016; Wilson et al., 2017; O'Regan et al., 2021). The number of floating ice tongues in the NGrIS has reduced since observation began. Of those named above, Petermann, Nioghalvfjerdsfjorden / 79N, and Ryder still terminate in floating ice tongues while C.H. Ostenfeld lost its tongue in 2002–2003 and has not recovered (Millan et al., 2023).

3.2 Petermann Glacier

Petermann Glacier (~ 80.7°N, 60.5°W) is the largest marine-terminating outlet glacier in north-west Greenland by ice flux, drains ~ 4 % of the GrIS, and terminates in Petermann Fjord, draining to the Nares Strait, with fjord bathymetry resolved by multibeam and gravity-inverted models to typical depths of 600 to 1100 m and a grounding-zone bed at ~ 600 m below sea level (Münchow et al., 2016; Tinto et al., 2015; Wilson et al., 2017). Ice velocity through the grounding-zone is ~ 1090 to 1100 m yr^{-1}, the highest among the NGrIS marine-terminating glaciers (Hill et al., 2017, 2018a). Petermann glacier sits above the marine outlet of a paleofluvial mega canyon extending > 700 km to the ice sheet interior (Bamber et al., 2013).

The floating tongue retreated from 81 km to 48 km between 2010 and 2012 across two large calving events, the first delivering an ice island of 253 ± 17 km^2 (Falkner et al., 2011; Münchow et al., 2014; Reilly et al., 2019). The grounding line has retreated 4 to 7 km since 1992, concentrated in the central-sector after 2017 (Fig. 1) and following a 15 % velocity increase over 2015–2018 (Millan et al., 2022; Ehrenfeucht et al., 2024).

A heightened discharge and retreat phase began in 2017 after a period of terminus and grounding-zone stability (Li et al., 2021; Millan et al., 2022). In July 2017, Petermann calved an 8.9 km^2 iceberg which, while not comparative in area to the 2010–2012 calving, caused the front to lose contact with the eastern fjord wall (Li et al., 2021). Fol-

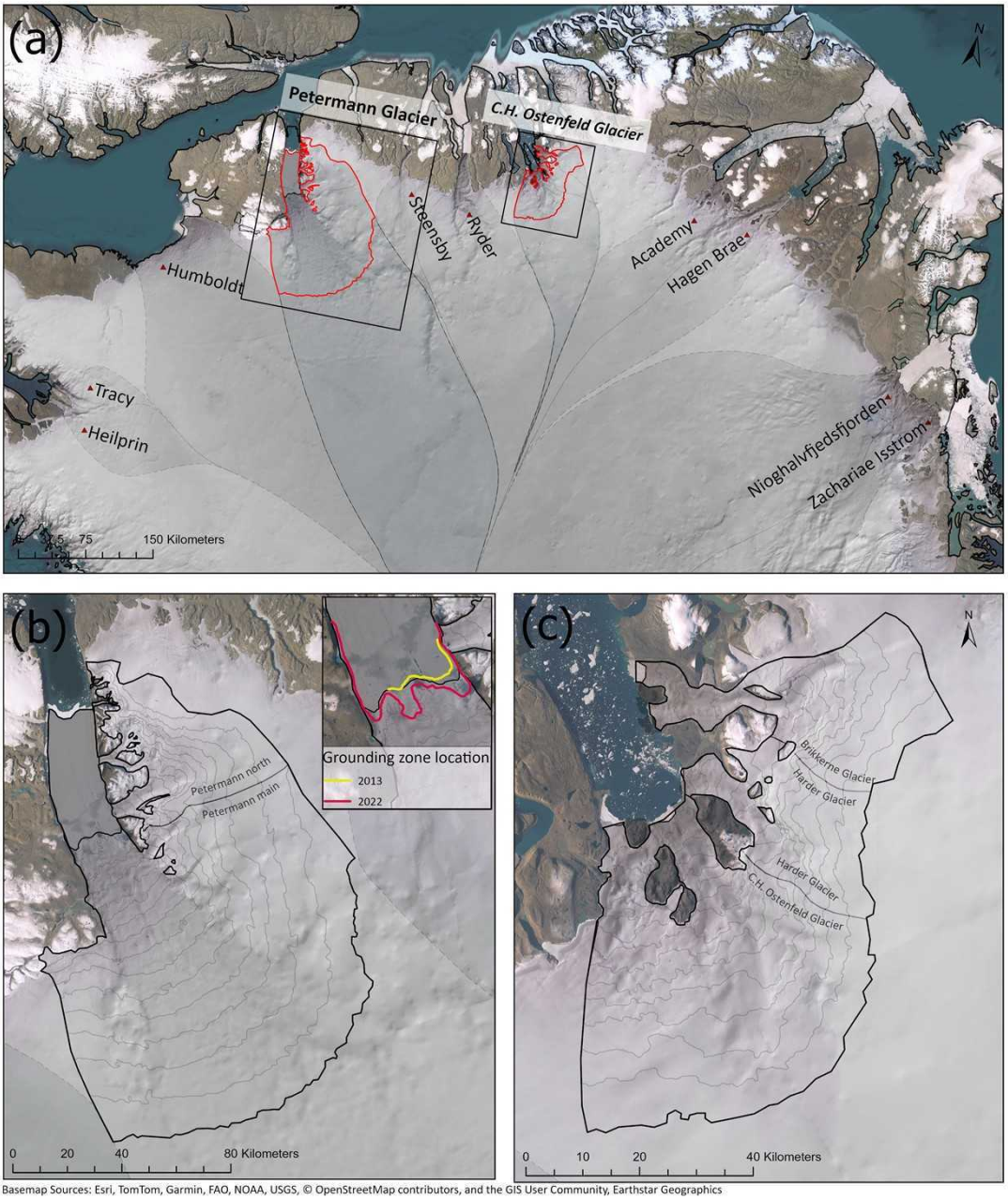

Figure 1. Study area map with major NGrIS basin outlines from Mouginot and Rignot (2019) over BedMachineV6. (a) Extent showing Petermann and Ostenfeld glaciers catchments and study area areas (red outline) and major NGrIS outlet catchments with labeled near terminus, (b) Petermann Glacier study area boundary with main and north catchments (labeled). Grounding zone locations are giving for 2013 (yellow line) and 2022 (red line). (c) Ostenfeld Glacier study area boundary with Harder and Brikkerne sub catchments labeled. Thin gray contour lines mark 100 m elevation bins in panels b and c. Greenland catchment boundaries from Mouginot and Rignot (2019) and Petermann grounding zone locations from Xi et al. (2026). *(CRS: EPSG:3413, WGS 84 / NSIDC Sea Ice Polar Stereographic North)*

lowing this calving, an episode of rapid retreat pushed the central grounding zone onto a retrograde bed (Li et al., 2021; Millan et al., 2022). Between 2017 and 2019, the central grounding-zone retreated more than 4 km, while the lateral sectors remained comparatively more stable (Ciracì et al., 2023; Millan et al., 2023). The ice tongue also became mechanically weaker during this period developing large longitudinal fractures, reducing lateral resistance and allowing the central trunk to respond to grounding-zone thinning and retreat with greater sensitivity. Surface elevation near the tidal grounding zone decreased by 22 m between 2011–2021, indicating a total thickness loss of 204 m (i.e., after subtracting 12 m in dynamic thinning, the observed surface elevation decrease represents the buoyant response to the loss of 192 m of basal thickness) (Ciracì et al., 2023). Winter velocities increased from approximately 1075 m yr^{-1} before the mid-2010s to about 1200 m yr^{-1} by 2018, after which speeds remained elevated (Millan et al., 2022).

At Petermann, the JJA subglacial discharge from the main subglacial channel is inferred to have increased from 149 m^3 s^{-1} to 301 m^3 s^{-1} over 2001–2022, an approximate doubling that coincided with grounding-zone retreat along the central tongue (Ciracì et al., 2023; Millan et al., 2022). Average basal-melt rates at the Petermann grounding zone currently exceed 17 m yr^{-1} with a JJA maximum between 80 to 100 m yr^{-1} and reach $>$ 150 m yr^{-1} at the crests of the basal channels (Rignot and Steffen, 2008; Washam et al., 2020; Ciracì et al., 2023). Modelling demonstrates that under RCP8.5, discharge at Petermann is projected to increase from 372 m^3 s^{-1} to 2754 m^3 s^{-1} (×7.4) with peak basal-melt rates rising to 181.5 m yr^{-1} (×7) (Cai et al., 2017; Prakash et al., 2025).

Additional Petermann research not directly drawn on here covers dynamic response to the 2010–2012 calving (Rückamp et al., 2019; Hill et al., 2018b), hypothetical breakup scenarios (Åkesson et al., 2022), fjord bathymetry (Jakobsson et al., 2020, 2018; Tinto et al., 2015), ice-ocean modelling (Prakash et al., 2023, 2022), and velocity reconstructions (Li et al., 2024, 2023).

3.3 C.H. Ostenfeld Glacier

C.H. Ostenfeld Glacier (~ 81.6°N, 45.2°W) is located in the north-central NGrIS sector and is the principal of three tributaries to Victoria Fjord (Box and Decker, 2011; Rignot et al., 1997). Ostenfeld drains a catchment of ~ 14 494 km^2 (~ 1.20 % of the GrIS surface area) and discharges ~ 2.32 km^3 yr^{-1} of ice, the fourth-largest discharge among NGrIS marine-terminating glaciers (Hill et al., 2017, 2018a; Mouginot et al., 2019). Its potential sea-level contribution has been estimated at ~ 3.9 cm of sea-level equivalent (Millan et al., 2023).

Brikkerne Glacier (~ 0.44 km^3 yr^{-1}, three branches entering Victoria Fjord ~ 15 km north of Ostenfeld) and Harder Glacier (~ 0.34 km^3 yr^{-1}, terminating adjacent to the present-day Ostenfeld front) drain to Victoria Fjord alongside Ostenfeld. Their drainage basins (2058 km^2 and 726 km^2 respectively) together total less than one-fifth of the Ostenfeld catchment; however, their former floating tongues merged with the Ostenfeld tongue, and they are included in the Ostenfeld study area on that basis (Hill et al., 2017, 2018a; Rignot et al., 1997). A substantial 90 × 10^6 m^3 subglacial outburst flood was observed to fracture the surface of Harder Glacier from below and decelerate the downstream glacier in 2014 (Bowling et al., 2025). Both Harder and Brikkerne are at present grounded-terminus outlet glaciers (Hill et al., 2018a). Published multi-beam

bathymetry for Victoria Fjord, acquired during the GEOEO North of Greenland 2024 expedition, will provide the first direct bathymetric constraints (Jakobsson et al., 2026).

Ostenfeld experienced a major loss of its floating ice tongue in 2002-2003. Pre-collapse, the floating extension exceeded 25 km in length and was extensively crevassed, fragmented, and detached from the fjord margins (Rignot et al., 1997). The ice-tongue collapse occurred over at an average retreat rate of ~ 3799 m yr^{-1}, with ~ 80 % of the floating extension lost in 2003 and a total floating-ice volume loss of 27 ± 2 km^3 since 1978 (Millan et al., 2023; Box and Decker, 2011). Subsequent terminus retreat continued at the much lower average rate of ~ 161 m yr^{-1} through 2015 (Hill et al., 2018a; Millan et al., 2023). By 2017, the Ostenfeld terminus was ~ 7.9 km wide and presented a residual floating ice tongue of ~ 1.5 km (Hill et al., 2017).

The dynamic response of Ostenfeld to the 2002–2003 tongue loss has been minimal. Grounding-line acceleration immediately after the collapse was < 8 % and lasted approximately three years, after which low-magnitude ice-flow deceleration occurred at the grounding line within the range of 2 to 28 %, and surface-elevation thinning rates increased only modestly between 2006 and 2014 (Hill et al., 2018a). Grounding-line ice velocities remained in the range of 770 to 800 m yr^{-1} after 2010 (Hill et al., 2018a), comparable to pre-collapse values (Rignot et al., 1997). The limited dynamic response has been attributed to the limited buttressing role of the former Ostenfeld ice tongue. The tongue had been detached from the fjord margins since at least the earliest aerial imagery in 1978, with sparse ice mélange after 1992, and is therefore unlikely to have provided substantial lateral resistance prior to its collapse (Hill et al., 2018a; Millan et al., 2023). Site-specific high-resolution work on Ostenfeld ice dynamics is sparse, and Ostenfeld has been included primarily as a single point in pan-GrIS or pan-NGrIS multi-glacier studies (Hill et al., 2017, 2018a; Mouginot et al., 2019; Millan et al., 2023). The surface-hydrology component of the Ostenfeld record has not been published prior.

4 Methods

4.1 Data

The remote-sensing inputs to this study are the entire Landsat 8 and Landsat 9 Top-of-Atmosphere (TOA) Collection 2 Level-1 catalogues over the period 2013 to 2025. 2013 is excluded from most analysis due to low coverage and retained only as additional ERA5-Land climate context, with the functional classified record beginning in 2014. Nine reflectance band inputs contribute to the classification and depth retrieval stages: the seven visible and near-infrared bands $B1$ to $B7$ are used as predictors and for the normalised difference water index over ice ($NDWI_{(ice)}$) following Dell et al. (2022) and Glen et al. (2025a); the panchromatic band $B8$ is used for the two-band depth retrieval (Pope et al., 2016; Moussavi et al., 2020) and the cirrus band $B9$ contributes to the cloud-masking step. The melt season used for scene selection, 1 May through 30 September, is defined intentionally broad to capture all potential melt and aligns with the definitions employed in similar GrIS surface melt inventories (e.g., Fitzpatrick et al., 2014; Wilson et al., 2017). It should be noted, however, that scenes from September are sparse due to late season solar elevation falling below the inclusion threshold, with the latest windows in the study not exceeding 6 September.

The area of interest (AOI) boundaries for Petermann and C.H. Ostenfeld glaciers (Fig. 1) are derived from the Greenland glacier-catchment polygons from Mouginot and Rignot (2019). In that dataset, Petermann comprises a north and main catchment with the north catchment bounding the north-western fjord wall and surrounding plateau (see Fig. 1). The Petermann catchment polygons are merged so that the full magnitude of runoff to the fjord is represented in the results. Likewise, the Ostenfeld boundary used here is derived from the C.H. Ostenfeld catchment combined with the smaller neighboring Brikkerne and Harder sub-catchments, with combined areas totaling less than one-fifth that of Ostenfeld.

The study area polygon boundaries are clipped to 1500 m elevation using the 30 m MEaSUREs Greenland DEM (Howat et al., 2014), which also supplies per-feature elevation attributes in later stages and the slope mask of Section 4.4.1. An elevation threshold is used to establish the interior boundary to enable reproducibility, inter-AOI and inter-data set comparison, and computational efficiency. The boundary elevation of 1500 m is set to exceed maximum lake elevations reported in Otto et al. (2022) by 200 m. Here, slush elevation maximums for NGrIS were not considered when establishing the elevation boundary. The fjord-facing margin of each AOI is redrawn to the minimum ice-tongue extent observed over 2014–2025 to remove seawater false-positives. Large nunataks and rocky coastal margins are manually excluded. Total AOI areas are 3516 km^2 at Ostenfeld and 15 087 km^2 at Petermann.

Climate data is retrieved from the ERA5-Land daily reanalysis (Muñoz-Sabater et al., 2021), as the daily 2 m air temperature T_{2m} and daily downward shortwave radiation $SW_{\downarrow}$ over each for the same 1 May to 30 September window across 2013 to 2025. JJA mean and per-year JJA maximum values are calculated per-year, per-AOI.

4.2 Workflow overview

The model training and classification method carried out here is based on the method for supervised classification of slush and SGLs on Antarctic ice shelves using Random Forest Machine learning developed by Dell et al. (2022, 2024) with additional modifications to the training data generation and classifier application proposed by Glen et al. (2025a). Lake depth is calculated here using the two-band radiative-transfer formulation of Philpot (1989), adapted for SGLs by Pope et al. (2016) and implementing the modifications for large scale automated depth retrieval developed by Moussavi et al. (2020). Modifications to these work established works are noted in relevant methods sections and an overview and justification of modifications is given in Section 6.2.

Classification is implemented in the Google Earth Engine (EE) JavaScript API (Gorelick et al., 2017) and produces the following key data products: (a) a stratified random-forest training pixel table from 14 pre-processed Landsat training scenes (Section 4.3), (b) classified mosaics per 2-day window with per-pixel lake depth covering 1 May to 30 September of each study year (Section 4.4), and (c) per-window vector shapefile exports of window footprint, slush, and lake polygons with lake depth and volume attributes. A schematic of the classification workflow is given in Fig. 2.

Following classification and export of class and volume data from EE, the analysis is implemented in Python. Per-window and per-block aggregation of slush area, lake area, lake volume, and elevation are made in Section 4.6.1. Trend and change-point tests on the annual JJA mean and maximum series are made in Section 4.6.2. An anomaly ana-

lysis against an algorithm-selected 3-year baseline is performed in Section 4.6.3. The climate-forcing, analog-pair, lag-1 residual, and recovery-rate analyses against ERA5-Land given in Section 4.6.4. The spatial persistency, maximum-melt, and persistent-lake products are derived in Section 4.6.5, and a per-lake drainage-event detection in Section 4.6.6. A coverage-correction projection that produces a scaled (observed + projected) processing set is described in Appendix E. A complete data and code inventory is provided in Appendix D.

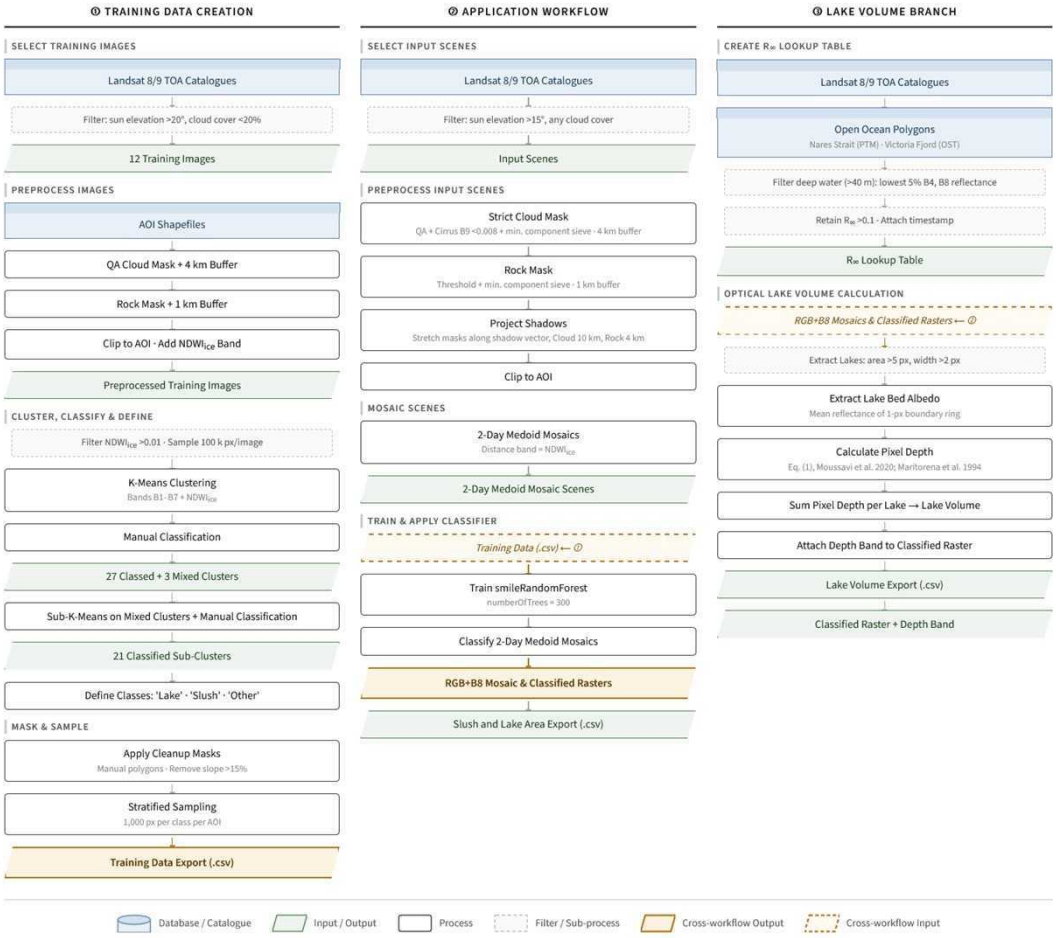

Figure 2. Diagram showing combined workflow for classified layer and volume data export from the EE API. Column (1) shows preprocessing, manual classification, and training data export; column (2) diagrams the classifier application workflow, highlighting training data input in orange; column (3) shows depth retrieval using $R_{\infty,i}$ lookup table and the column classified layers from the previous column. Diagram shows external inputs (blue), local inputs/outputs (green), filters (gray dashed line), processing steps (solid gray outline) and cross.

4.3 Training-data generation

4.3.1 Training-image selection and preprocessing

Training scenes are drawn from the Landsat-8 + 9 TOA catalogs and selected manually from a subset filtered by cloud cover $< 5\,\%$, solar elevation $> 20°$, and acquisition between 1 May and 30 September within the study years. From the filtered subset, 14 training scenes are selected, seven per AOI, with a 10:4 ratio of Landsat 8 to Landsat 9 scenes, a sensor proportion that approximates that of the combined catalog. Manual

selection of training scenes is carried out to ensure the full melt season and the full solar-elevation range is represented (solar elevation ranges from 21.5° to 32.0°), and are temporally distributed with at least one scene per month per AOI. Scenes with no or minimal cloud cover were preferred. The 14 training scenes are documented in Appendix A.

Training scenes are preprocessed following Dell et al. (2022), adapted here to accommodate Landsat collection 2 data format and with the additional inclusion of an $\mathrm{NDWI}_{(\mathrm{ice})}$ threshold sieve in the rock mask and the addition of a slope mask. The $B4$, $B5$, $B9$ band-ratio threshold rock mask from Moussavi et al. (2020) is applied with a 3 km buffer. An $\mathrm{NDWI}_{(\mathrm{ice})} > 0.35$ sieve is added to prevent high $\mathrm{NDWI}_{(\mathrm{ice})}$ pixels (i.e., wet pixels) from entering the rock mask. Cloud and cloud shadow are masked from the QA_PIXEL bitmask with an 8 km buffer. An additional slope mask derived from the MEaSUREs DEM removes pixels with slope > 15 % and prevents glacial terrain shadow contamination (i.e., shadows cast by a local mound or trough of the glacier) from being added to the training data. Scenes are clipped to the AOI boundary, an $\mathrm{NDWI}_{(\mathrm{ice})}$ band defined as $\mathrm{NDWI}_{(\mathrm{ice})} = (B2 - B4)/(B2 + B4)$ (Dell et al., 2022) is calculated per pixel and added, and the preprocessed scenes are exported as EE assets for clustering.

4.3.2 K-means clustering

Training-data pixels are grouped by a k-means unsupervised clustering algorithm based on $B1$ to $B7$ reflectance plus $\mathrm{NDWI}_{(\mathrm{ice})}$, adapted from Dell et al. (2022) by the addition of $\mathrm{NDWI}_{(\mathrm{ice})}$ as a k-means input band. A $\mathrm{NDWI}_{(\mathrm{ice})} > 0.1$ threshold value is used to select potentially "wet" pixels to cluster from the preprocessed training scenes (Dell et al., 2022). Training scenes are sampled at 100 000 pixels per scene. The k-means clustering algorithm groups the sampled pixels by similarity across the eight input bands ($B1$ to $B7$ and $\mathrm{NDWI}_{(\mathrm{ice})}$) and outputs between 5 and 70 clusters. Here, the initial k-means produced 30 main clusters across the 14-scene pool. Clusters were manually classified as either slush, lake, or other (see Section 4.3.3). Of the 30 main clusters, three large ambiguous clusters were identified and resampled at 10 000 pixels per cluster for a sub-clustering pass with an allowed cluster count between 8 and 40, returning a further 20 sub-clusters that were manually classified.

4.3.3 Manual classification rubric (lake / slush / other)

The k-means cluster IDs returned by EE are deterministic under a fixed random seed and are reproducible between scripts. Due to the challenge of classifying slush, an intermediary k-means cluster inspection program was developed using the EE user interface infrastructure. The inspection script isolates clusters, generates basic descriptive statistics on their spectral distribution, and loads higher resolution imagery for manual inspection if available; this was the primary tool used to classify clusters.

Each main cluster and each sub-cluster is assigned to one of three classes per AOI: lake, slush, or other. The other class functions as a pool of high-confidence negative-examples for the RF of pixels that are unambiguously neither lake nor slush (e.g., dry ice, blue ice, firn, snow, dirty ice, and residual cloud or terrain-shadow pixels). Clusters are defined per-AOI because individual clusters can express as different surfaces between the two glacier environments. The lake class is spectrally well grouped, with strongly peaked $\mathrm{NDWI}_{(\mathrm{ice})}$ signatures and narrow transition zones, and is assigned by inspection

of the per-cluster band-mean profile together with cross-reference against Sentinel-2 $NDWI_{(ice)}$ and EE high-resolution catalogs where available (2016 onward).

Slush clusters lie along a transition between ponded water on the wet end and firn or ice on the dry end and hence a classification framework to maintain class consistency and limit subjective bias is used to interpret ambiguous clusters. Each candidate cluster is scored on seven physical and spectral criteria with a score of +1 for positive support, 0 for no signal, and −1 for negative support, giving a total slush signal in the range −7 to +7:

(1) mottled texture indicative of early saturation;

(2) no visible ice grain, which rules out blue ice;

(3) proximity to ponded melt water;

(4) location in shallow, low-relief, trough or bowl topography;

(5) lineation (if present) perpendicular to topographic contours;

(6) elevation consistent with the seasonal timing of the scene;

(7) cluster-mean $NDWI_{(ice)}$ greater than approximately 0.115, matching the slush threshold used by Dell et al. (2022) and Bell et al. (2017).

A signal greater than +3 is taken as strongly indicating slush and a signal of +3 or less assigns it to other.

4.3.4 Stratified sampling

Of the 30 main clusters, 14 were expressed identically in both AOIs. Seven clusters were unambiguously slush on Petermann and unambiguously ice on Ostenfeld. Nine clusters were ambiguous on both AOIs and the six smallest were excluded from the training data, following the Glen et al. (2025a) approach for ambiguous clusters. Three large ambiguous clusters were passed through the sub-k-means and the resulting 20 sub-clusters were classed under the rubric of Section 4.3.3. The cluster counts for final training data classes are given in Appendix A.

Per-AOI clusters then contribute to a stratified random pixel sample of 1000 pixels per class per AOI, for a total of $3 \times 2 \times 1000 = 6000$ pixels in the deployed training table. Per-class stratification preserves the equal-weight balance across lake, slush, and other and per-AOI stratification preserves the spectral diversity of the two glacier environments without weighting either by area or by raw cluster count.

4.4 Application

4.4.1 Two-day mosaics

For each AOI and each study year the full Landsat 8 + 9 TOA archive in the 1 May to 30 September window is assigned into contiguous non-overlapping 2-day windows. Within each window all scenes intersecting the AOI are filtered to solar elevation $> 15°$. This threshold is relaxed from the $> 20°$ training-scene filter so that late-season returns are not lost. Scenes are ranked by the intersection area of the raw scene footprint with

the AOI polygon. The top nine scenes per window are retained for preprocessing in order to bound the per-window compute cost without limiting window footprints. All cloud-cover values are accepted into the per-window scene set because the per-pixel cloud and cloud-shadow masks handle pixel-level rejection downstream.

Preprocessing is applied to input scenes prior to mosaicking. Input scenes are corrected with the rock mask used in training scene preprocessing (Moussavi et al., 2020) (with the $\mathrm{NDWI}_{(\mathrm{ice})} > 0.35$ sieve retained). The rock buffer reduced to 1 km. Application cloud masking uses all QA_PIXEL cloud and confidence bits, and an additional $B9$ threshold of < 0.008 for cirrus masking. The union of the $B9$ and QA_PIXEL bit mask detections is passed through a 24-pixel minimum-connected-component sieve to remove minor detections. Cloud pixels are buffered by 5 km. Buffer sizes are reduced from training scene preprocessing to account for the more efficient masking allowed by preprocessing per scene prior to building the window composites. Buffered cloud footprints are stretched a fixed 8 km distance along a per-scene shadow vector, computed from the solar azimuth and solar elevation in the scene metadata.

The retained scenes within each 2-day period are merged into a per-window composite using a medoid mosaic function. Medoid-mosaics are multi scene composites where pixels are selected from input scenes by computing the median value at each raster cell for a given selector-band. Here, the real pixel with the closest-to-median $\mathrm{NDWI}_{(\mathrm{ice})}$ value is selected for the 2-day mosaics. The actual coverage of the AOI for each window is stored as a binary footprint band in the per-window layer prior to classification. Pixels with $\mathrm{NDWI}_{(\mathrm{ice})} \geq 0.1$ are passed to the classifier.

Table 2. Summary of classified shapefiles and unique 2-day windows for Petermann and Ostenfeld by total and adjusted counts to illustrate data volume. Here, *n* files refers to the total number of shapefiles exported from EE, where there are between one and three shapefiles per classified window representing either classified lake, slush, or window coverage footprint. Unique 2-day windows are represented in the "n footprints" column, as footprints are generated for all windows with coverage, while classified lake and slush layers are only generated when present.

Period	Season	AOI	n files	n footprints	n possible windows
2013-2025	1 May – 30 Sep.	Ptm.	2041	738	988
		Ost.	1762	654	988
		Total	3803	1392	1976
2014–2025	1 May – 6 Sep.	Ptm.	1990	719	768
		Ost.	1718	635	768
		Total	3708	1354	1536

4.4.2 Random-forest classifier

Classification uses a random forest implemented on the 6000-pixel stratified training table of Section 4.3.4, with the eight per-pixel features, $B1$ to $B7$ and $\mathrm{NDWI}_{(\mathrm{ice})}$ as predictors, returning a class label per pixel for lake, slush, or other. The hyperparameters used in the classifier are: $N_{\mathrm{trees}} = 300$, variables per split set to the EE default of $\lfloor \sqrt{p} \rfloor = 2$ for $p = 8$, minimum leaf population of 1, bag fraction of 0.632, and unlimited tree depth.

Per-window classified rasters carry four bands at 30 m resolution: (1) a classification band with values {1 = lake, 2 = slush, 3 = other}, (2) a binary AOI-footprint mask recording window coverage, (3) the mean reflectance in the red band $B4$, and (4) the mean

reflectance in the panchromatic band $B8$, both taken over a one-pixel ring around each lake polygon (A_d^{B4} and A_d^{B8} are used as lakebed-albedo proxies in the depth calculation; see Section 4.5). The per-window classified rasters are stored as EE assets and serve as the input to the depth retrieval and vector exports.

4.4.3 Validation

Classifier accuracy is reported on a per-pixel holdout drawn from 10 Landsat scenes that are not present in the training pool: four Ostenfeld scenes (Vi01–Vi04) and six Petermann scenes (Vi05–Vi10), aggregated to 2556 reference pixels. Each holdout pixel is labelled by inspection against the per-scene Landsat RGB and $\mathrm{NDWI}_{(\mathrm{ice})}$ composite, against Sentinel-2 imagery on the same date or within ± 1 day where available, and against the high-resolution EE basemap, applying the same per-AOI classification logic and slush rubric used to label clusters in Section 4.3.3. Per-class metrics are reported in the form used by Glen et al. (2025a), namely precision, recall, F_1, and support per class together with overall accuracy and Cohen's κ. Classifier accuracy metrics for the deployed model are reported in full in Section 5.1.2.

4.5 Lake-volume retrieval

During classification, a `B4_ring` band and `B8_ring` band are calculated for each lake using a dilate function in EE. The classified water mask is dilated by one native pixel and the TOA reflectance in bands $B4$ and $B8$ is retained as lake ring masks in the exported classified rasters. In a separate step, per-pixel depth is calculated and attached as band data to the classified lake layers. Lake and slush pixels are converted to polygons using a > 5 connected-component function to extract melt features as objects. The footprint mask is separately vectorized. Each output feature is tagged with window identifiers. Mean and maximum depth and volume per lake object are assigned as attributes before export as class shapefiles.

Per-pixel lake depth is retrieved from per-window TOA reflectance using the two-band radiative-transfer formulation of Philpot (1989) as applied to supraglacial lakes by Pope et al. (2016) and adapted for automated cryosphere application by Moussavi et al. (2020). For each lake pixel and each band $i \in \{B4, B8\}$,

$$z_i = \frac{\ln(A_{d,i} - R_{\infty,i}) - \ln(R_{w,i} - R_{\infty,i})}{g_i}, \tag{1}$$

where $R_{w,i}$ is the observed TOA reflectance of the lake pixel in band i, $A_{d,i}$ is the lake-bed albedo, $R_{\infty,i}$ is the reflectance of optically deep water, and g_i is the two-way diffuse attenuation coefficient (Maritorena et al., 1994). The per-pixel depth z is reported as the mean of z_{B4} and z_{B8} and is capped at $z_{\max} = 20\,\mathrm{m}$ to suppress runaway values from optically saturated pixels. The two attenuation coefficients are fixed at $g_{\mathrm{red}} = 0.80$ and $g_{\mathrm{pan}} = 0.36$ as in Pope et al. (2016), and are not fitted per lake due to time constraints.

Following Moussavi et al. (2020), lake-bed albedo is estimated per lake and per band from the mean TOA reflectance of the one-pixel ring around each lake. This is based on the assumption that the lake margin can be used as proxy for lake bed albedo beneath the water column. The deep-water reflectance $R_{\infty,i}$ is built per AOI from polygons over open-ocean in Nares Strait (Petermann) and off shore of Victoria Fjord mouth (Ostenfeld). Deep water reflectance is stored in a lookup table, constructed by taking the lowest

5 % of TOA reflectance values for $B4$ and $B8$ across all Landsat 8 + 9 scenes intersecting the deep-water polygons. Only values with $R_{\infty,i} < 0.1$ (true optically deep water) are retained in the table along with date, time, and pixel coordinates. The lookup table is queried at depth retrieval for the classified lakes and returns the closest $R_{\infty,i}$ value in space and time for each depth calculation. Per-lake volume is the sum of pixel depth multiplied by the per-pixel area of 900 m^2, i.e. $V_{\text{lake}} = \sum_{i=1}^{n} z_i A_{\text{pixel}}$.

The systematic uncertainty introduced by the four free parameters of the depth retrieval (g_{red}, g_{pan}, A_d^{B4}, A_d^{B8}) is quantified by perturbation tests on six representative lakes (three at Ostenfeld and three at Petermann, spanning the per-lake area and depth distributions). Each parameter is independently perturbed by ± 20 % at 2 % steps with the other three held fixed, and the joint ± 20 % perturbation of A_d^{B4} and A_d^{B8} is run as the worst-case lake-bed-albedo bias case. The per-lake volume change ranges are reported in Section 5.1.3 and the per-lake systematic uncertainty is approximately 15 to 25 %, dominated by g and A_d^{B8}; AOI-aggregated volumes are tighter than this because per-pixel errors partially cancel.

4.6 Post-processing and analysis

4.6.1 Per-window and per-block aggregation

Elevation attributes ($\text{elev}_{\text{mean}}$, elev_{min}, elev_{max}) are attached to each 2-day window lake and slush shapefile, drawn from the MEaSUREs DEM. Per-window shapefiles are then aggregated into contiguous 5-window blocks anchored to a fixed 1 May start each year, giving a per-block temporal resolution of 10 day and a per-AOI annual block count between 8 and 12 depending on the number of valid 2-day windows in each year. Per-block aggregates of slush area, lake area, lake volume, and elevation are computed from the constituent per-window polygons and are the reporting basis for all annual statistics in the thesis. The JJA mean and JJA maximum of each metric are then taken per AOI per year over all valid blocks falling within the JJA window, producing per-AOI annual time series of $n = 12$ for the 2014–2025 record. Per-window footprints with coverage below 10 % of the AOI are excluded from all per-AOI annual statistics.

The per-window data are retained alongside the per-block data and serve as the input to the drainage-event detection of Section 5.10. The 2-day scale preserves the rapid drainage signals.

4.6.2 Trend and change-point tests

The non-parametric Mann-Kendall trend test (Mann, 1945) is performed on annual JJA mean and maximum series ($n = 12$, 2014-2025) for all melt metrics (combined area, slush area, lake area, lake-mean and lake-maximum elevation, and lake-mean and lake-maximum volume). The Mann-Kendall test reports effect size (Kendall's τ), two-tailed p-value, and Sen slope. The Hamed-Rao modification of the Mann-Kendall test (Hamed and Ramachandra Rao, 1998) is performed to correct for first-order autocorrelation and derive variance-inflation factor. The non-parametric Pettitt change-point test (Pettitt, 1979) is performed per series and the test statistic K, the inferred change-point year, and the two-tailed p-values are reported. At $n = 12$, effect sizes are reported as primary and p-values as secondary.

4.6.3 Anomaly analysis vs algorithm-selected baseline

Per-year anomalies of area, elevation, and lake volume are reported against an algorithm-selected 3-year baseline window per AOI, with the baseline selected on the observed combined-maximum area series. The candidate windows are all contiguous 3-year intervals in the 2014–2025 record. A window is eligible when (i) every year contributes at least three valid 5-window blocks, (ii) when each year shows per-window AOI footprint coverage of at least 20 %, and (iii) when no year in the window exceeds the 75th percentile of the per-AOI combined-maximum-area distribution. Eligible windows are ranked by the coefficient of variation (CV) of the per-year combined-maximum area within the window, and the window with the lowest CV is selected as the baseline. Ties within 0.02 CV are broken by lowest baseline mean, then by lowest CV, then by highest mean coverage, and finally by earliest start year. The same baseline window is then applied identically to every area, elevation, and volume metric so that the resulting percent and fold-change anomalies are comparable. The algorithm selects 2017–2018-2019 at Ostenfeld and 2016–2017–2018 at Petermann.

Baseline sensitivity is tested by comparing anomalies across four reference period definitions.

a) Algorithm (CV): a 3-year window selected by lowest coefficient of variation, after excluding years above the 75th percentile of combined-maximum. Biased towards the lowest-melt years of the record.

b) Record median: the median combined-maximum across all 12 years (2014–2025).

c) Pre-2020 mean; the mean of 2014–2019, taken as a reference period before melt intensified.

d) Full-record mean; the mean across the entire 2014–2025 record.

Results of the sensitivity test are reported in Section 5.5.

4.6.4 Climate forcing, hysteresis, and recovery-rate analyses

Climate variables: Daily ERA5-Land 2 m temperature T_{2m} and downward shortwave $\mathrm{SW}_{\downarrow}$ over the 1 May to 30 September window are aggregated to four annual predictors per year: $T_{2m,\mathrm{JJA,mean}}$, $T_{2m,\mathrm{JJA,max}}$, $\mathrm{SW}_{\downarrow,\mathrm{JJA,mean}}$, and $\mathrm{SW}_{\downarrow,\mathrm{JJA,max}}$. This aggregation mirrors the JJA mean and JJA maximum aggregation used for the melt-response series in Section 4.6.2. Per-AOI Pearson R^2 and Sen slope are reported for each predictor against each annual melt-response metric, alongside the two-tailed p-value and the AOI-fixed-effect pooled-AOI fit. For each AOI and each predictor–response pair, the climate–melt OLS fit is a univariate ordinary least squares (OLS) regression,

$$y_i = \beta_0 + \beta_1 x_i + \varepsilon_i. \tag{2}$$

Here y_i is the annual melt-response metric in year i, x_i is the corresponding annual ERA5 predictor, and ε_i is the regression error term. The fitted value $\hat{y}_i$ gives the climate-predicted response and the residual $r_i = y_i - \hat{y}_i$ is retained as the climate-corrected melt response.

Analog Years: Analog pair analysis is used here to identify years with similar external forcing and to compare their melt metrics for climate-corrected response. The assump-

tion is that between analog years with equivalent forcing, the variation in melt response not explained by climate originates from an internal state variable, e.g., glacial dynamics, firn state, or surface preconditioning. The screen runs independently per AOI over the 66 unordered year pairs available from the 12-year record, and within each AOI it is repeated for every combination of ERA5 predictor and melt-response metric. The four ERA5 predictors are $T_{2m,\mathrm{JJA,mean}}$, $T_{2m,\mathrm{JJA,max}}$, $\mathrm{SW}_{\downarrow,\mathrm{JJA,mean}}$, and $\mathrm{SW}_{\downarrow,\mathrm{JJA,max}}$. They are tested against six annual area metrics, six annual elevation metrics, and two annual lake-volume metrics, giving 56 (predictor, response) combinations per AOI.

Within each combination the climate–melt OLS fit of Eq. 2 is applied to the per-year predictor and per-year melt response, retaining the climate-corrected melt response r_i. Predictor values and climate-corrected melt responses are then converted to z-scores using the in-sample mean and standard deviation,

$$z_x(i) = \frac{x_i - \bar{x}}{\sigma_x}, \qquad z_r(i) = \frac{r_i - \bar{r}}{\sigma_r}$$

where $\bar{x}$ and σ_x are the sample mean and standard deviation of the predictor across years and $\bar{r}$ and σ_r are the sample mean and standard deviation of the climate-corrected melt response across years. A year pair (i, j) is flagged as analog within that combination when the predictor z-scores are close together and the climate-corrected response z-scores are far apart,

$$|z_x(i) - z_x(j)| < 0.5 \quad \text{and} \quad |z_r(i) - z_r(j)| > 1.0. \tag{3}$$

Both thresholds, 0.5 SD on the predictor difference and 1.0 SD on the residual difference, are held fixed across all combinations rather than rescaled to a percentile of the within-combination distribution. A given year pair within an AOI can accumulate up to 56 flags across the combinations it satisfies, and the per-pair flag count is used to rank candidates. The most-flagged pairs are reported in Section 5.7 and interpreted in Section 6.6.

Lag-1 residuals: Lag-1 residual-correlation analysis computes the Spearman rank correlation of the current-year climate-corrected melt response from Eq. 2 against the prior-year raw melt-response,

$$\rho_{\mathrm{lag1}} = \mathrm{Spearman}(r_i,\ y_{i-1}), \tag{4}$$

where r_i is the climate-corrected melt response in year i and y_{i-1} is the raw melt-response metric in year $i - 1$. Within each AOI the test runs across every (predictor, response) combination used in the climate–melt OLS fits, giving $n = 11$ paired years over the 12-year record. A positive ρ_{lag1} indicates that years with positive climate-corrected melt response tend to follow years of above-average raw melt response, which is interpreted as a state-dependence or carryover signal in the surface system. Spearman ρ_{lag1} values for the seven retained melt metrics are reported in Section 5.7, with the six elevation metrics and the lake-mean-volume metric computed but omitted from the table for readability. The lag-1 residual correlation is statistically distinct from raw-series autocorrelation, which is what the Hamed-Rao Mann-Kendall modification of Section 4.6.2 tests for.

Recovery-rate: Recovery rate is used here to quantify how quickly surface meltwater recovers following a low melt year and how much of that recovery is and is not explained by climate forcing. Specifically, the test measures the rate at which melt metrics increase from a low-melt trough to a high-melt peak, defined using JJA combined mean melt area. The simple linear regression slope of combined mean area against year is the recovery rate in km^2/yr. A cold-to-warm growth cycle is defined as a contiguous run of years from a local low (trough) in the per-AOI JJA combined-mean area to the next local high (peak). The recovery-rate slope is the OLS slope of combined-mean area on year over the trough-to-peak window.

The two cycles retained per AOI are 2017–2019 (3 years) and 2020–2023 (4 years), held at identical calendar windows to permit direct comparison. Seven alternative trough-to-peak window combinations per AOI satisfy the candidate criteria. The sensitivity to cycle-boundary choice is documented in the appendix. Slope uncertainty is the 2.5th to 97.5th percentile of 2000 non-parametric bootstrap resamples of the year-area pairs within each cycle window. At $n = 3$–4 per cycle the slopes are descriptive comparisons rather than significance tests. Climate-corrected slopes are computed by taking residuals of the per-AOI annual combined-mean area against ERA5 predictors over the full $n = 12$ record under three correction models (single-predictor T_{mean}, single-predictor T_{max}, and two-predictor $T_{\text{max}} + \text{SW}_{\text{mean}}$) and refitting the OLS slope on year over each cycle window. Predictor count is capped at two given $n = 12$ per AOI. The $T_{\text{max}} + \text{SW}_{\text{mean}}$ model pairs the empirically dominant single predictor (T_{max}) with the approximately orthogonal radiative term. $\text{SW}_{\downarrow,\text{max}}$ is not used because no single-predictor combination involving it returns $p < 0.10$. Per-AOI rather than pooled fits are used because pooling washes out the inter-glacier asymmetry in climate sensitivity.

4.6.5 Spatial products

Four spatial products are derived from the per-window classified rasters. Per-cell 30 m persistency rasters are built per AOI and per class (lake, slush, combined wet) by dividing, at each grid aligned 30 m cell, the per-cell number of valid windows classified as that class by the per-cell number of valid windows over the 2014–2025 record (Section 6.7). Annual maximum-melt block maps are produced by selecting, per AOI and per study year, the single 5-window block with the largest combined-area sum and exporting it as a categorical raster of lake, slush, and other (Section 5.9). Annual maximum-melt RGB medoid mosaics are exported as the Landsat RGB composite of the maximum-melt block per AOI per year, providing visual context alongside the categorical block maps. Persistent-lake polygons are derived from the per-class persistency rasters by selecting cells with a persistency score > 25, passing the selection through a minimum-100-connected-component sieve, converting to vector polygons with a 300 m buffer, and merging polygons that share > 15 % of their perimeter with a larger neighbour. The resulting polygons serve as the basin definition for the per-lake drainage detection of Section 4.6.6.

4.6.6 Drainage-event detection

For each persistent-lake polygon a per-window lake-volume time series is constructed by summing the per-pixel depth-derived volume (Section 4.5) over the lake-polygon pixel set, restricted to windows in which the polygon is observed. A drainage event is recorded between two consecutive observations of the polygon when the pre- to post-observation

lake volume drops by at least 40 % and the elapsed gap between the two observations is at most 5 windows (10 day). The gap length between the pre- and post-drainage observation is retained as a per-event confidence score, with shorter gaps meaning to higher confidence. Events are classified as full when the volume drop is at least 80 % and as partial when the drop is between 40 % and 80 %. Chain events are flagged in a separate field when two or more persistent-lake polygons drain within the same window or within ± 1 window of each other. Per-event drainage volume is the pre-event minus post-event lake volume, and aggregate annual drainage volumes per AOI are the sum of per-event drainage volumes over events with start dates within the JJA window of that year. Auxiliary per-lake observation-fraction series are retained as a filter at the reporting stage to exclude events where the per-window polygon coverage is too low to support a robust pre- to post-observation volume comparison.

5 Results

5.1 Mapped catalogue and data confidence

The mapped catalogue spans the twelve melt seasons from 2014 through 2025, with 2013 retained only for ERA5 climate context (Section 5.6). The melt season is defined as 1 May to 30 September, although Landsat returns from September are sparse owing to low solar angles at these latitudes. A total of 3,803 per-window classified shapefiles were produced (2,041 at Petermann and 1,762 at Ostenfeld), corresponding to 1,392 unique 2-day windows out of a possible 1,976. Two related metric families are used throughout the analysis. The per-window (2-day) metrics are the higher temporal resolution input used for drainage-event analysis. The per-block metrics, which are aggregates of five classified windows (10-day) anchored to a fixed 1 May start each year, are the reporting basis for all annual JJA mean and maximum statistics and time-series analysis. A per-AOI catalogue summary giving the number of valid 2-day windows, the number of 10-day blocks per year, and the mean per-window AOI footprint coverage per year is provided in Table 3. Per-year maximum-melt mosaics for each AOI are presented later in Section 5.9.

Table 3. Per-AOI catalogue summary, 2014–2025, for Ostenfeld (Ost) and Petermann (Ptm). *Blocks* is the number of valid 10-day blocks per year (5-window aggregate, anchored to 1 May). *Coverage* is the mean per-window AOI footprint coverage averaged across the year. The 10 % coverage threshold used for inclusion is met by every year of the record. Petermann 2017 (0.72) and Petermann 2021 (0.77) are the two single weakest years; both remain above the threshold and are flagged as low-coverage years.

	Ost		Ptm	
Year	Blocks	Coverage	Blocks	Coverage
2014	9	0.89	9	0.86
2015	9	0.86	9	0.88
2016	9	0.95	10	0.85
2017	8	0.77	9	0.72
2018	8	0.87	9	0.81
2019	8	0.80	8	0.81
2020	9	0.85	10	0.85
2021	9	0.89	9	0.77
2022	9	0.97	9	0.95
2023	9	0.92	8	0.85
2024	10	0.92	10	0.91
2025	9	0.98	9	0.86
Mean	8.8	0.89	9.1	0.84

5.1.1 AOI footprint coverage

Mean JJA per-window AOI footprint coverage was consistently high at both glaciers across 2014–2025, ranging from 0.77 to 0.98 at Ostenfeld and from 0.72 to 0.97 at Petermann. The two weakest years are Petermann 2017 (0.72) and Petermann 2021 (0.77); both remain above the 10 % inclusion threshold (Section 4.6.1) and are flagged in later sections as low-coverage years. Coverage is reported visually in the bottom-row panels of Fig. 3.

5.1.2 Random-forest classifier accuracy

The aggregate confusion matrix (Fig. 4) gives an overall accuracy of 0.902, Cohen's κ of 0.847, and a macro F_1 of 0.895. Per-class recall is high and balanced across the three classes: lake 0.898 (985 of 1,097), slush 0.889 (878 of 988), and other 0.941 (443 of 471); per-class precision is 0.965, 0.897, and 0.797 respectively, giving per-class F_1 of 0.930, 0.893, and 0.863 (Table 4). Mean per-scene overall accuracy is 0.910 (range 0.872–0.990), with Ostenfeld scenes averaging 0.916 and Petermann scenes 0.906. The two largest off-diagonal terms both involve the slush–other transition (true slush predicted as other, 7.9 %; true other predicted as slush, 5.1 %), reflecting the documented difficulty of the slush–firn / slush–ice boundary in optical imagery (Dell et al., 2024). Lake confusion is minor in all directions (lake as slush 7.0 %, slush as lake 3.2 %, lake as other 3.2 %, other as lake 0.8 %), so per-pixel lake area and volume retrievals are tightly constrained by the classifier. Visual assessment can be carried out using the spatial melt maps presented in Section 5.9.

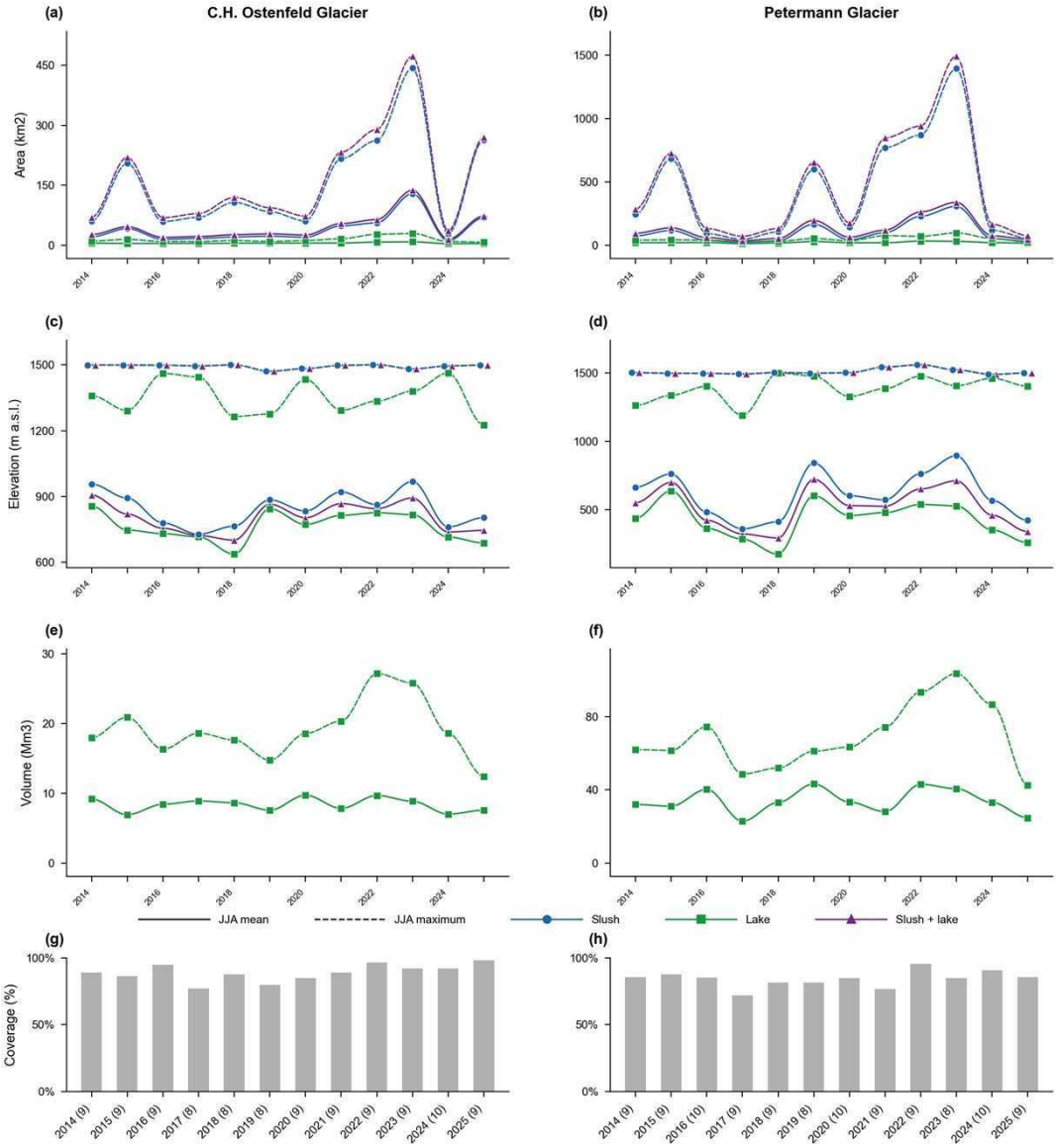

Figure 3. Mean (solid line) and maximum (dashed line) June-July-August (JJA) melt area (a, b), melt-feature elevation (c, d), and lake volume (e, f) for C.H. Ostenfeld Glacier (left column) and Petermann Glacier (right column), 2014-2025. Solid lines show the annual JJA mean and dashed lines show the annual JJA maximum; colors distinguish slush (blue), lake (green), and combined slush + lake features (purple). Elevation panels show area-weighted mean elevation and maximum feature elevation. Panels (g) and (h) show mean JJA AOI footprint coverage for Ostenfeld (left) and Petermann (right), with the number of contributing 5-window blocks per year given in parentheses in the x-axis year labels. Annual statistics use only blocks within the JJA day-of-year window and apply a minimum AOI footprint coverage threshold of 10 % for metric aggregation; the coverage bars report the mean JJA footprint coverage before that threshold is applied.

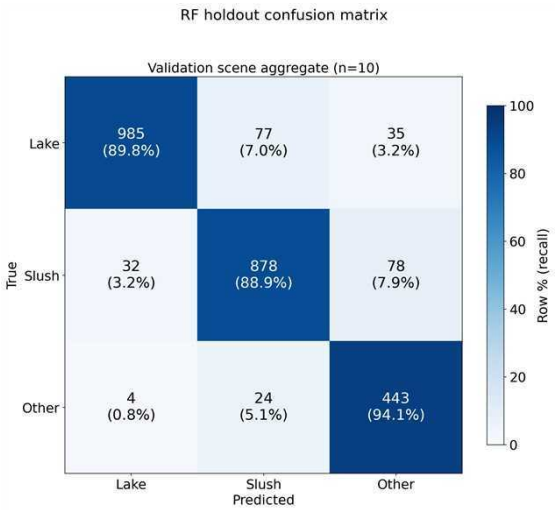

Figure 4. Aggregate macro confusion matrix for the random-forest classifier across the ten validation scenes (2,556 holdout pixels). Cell values are pixel counts with row percentages (per-class recall) shown in parentheses; the color scale shows the row percentage.

Table 4. Aggregate per-class confusion summary across the ten validation scenes (2,556 holdout pixels). The dominant error mode is the slush–other transition; lake confusion is minor in all directions.

Class	Support	Recall	Precision	F_1	Main misclassification
Lake	1,097	0.898	0.965	0.930	as slush (7.0%), as other (3.2%)
Slush	988	0.889	0.897	0.893	as other (7.9%), as lake (3.2%)
Other	471	0.941	0.797	0.863	as slush (5.1%), as lake (0.8%)
Overall	2,556	accuracy 0.902; κ 0.847; macro F_1 0.895			

5.1.3 Volume-retrieval sensitivity

Lake volumes are retrieved using the Pope et al. (2016) and Moussavi et al. (2020) two-band depth formulation applied to the red ($B4$) and panchromatic ($B8$) bands, with deep-water reflectance (R_∞) sourced from a per-AOI lookup over Nares Strait and Victoria Fjord. To quantify the systematic uncertainty introduced by the depth-formula constants, each of the four free parameters was perturbed by $\pm 20\,\%$ for six representative lakes. The diffuse attenuation coefficient g produces an asymmetric volume change of 25 % to $-16.7\,\%$ under a $\pm 20\,\%$ perturbation, reflecting the inverse depth–g relationship. The panchromatic-band lakebed albedo A_d^{B8} produces a 13 to 26 % volume change (lake-dependent), while the red-band albedo A_d^{B4} produces only 5 to 10 % because $g_{\text{red}} = 0.80$ exceeds $g_{\text{pan}} = 0.36$ and damps the red-band sensitivity. Compounding both albedo perturbations together yields a 18 to 34 % volume change (Fig. 5).

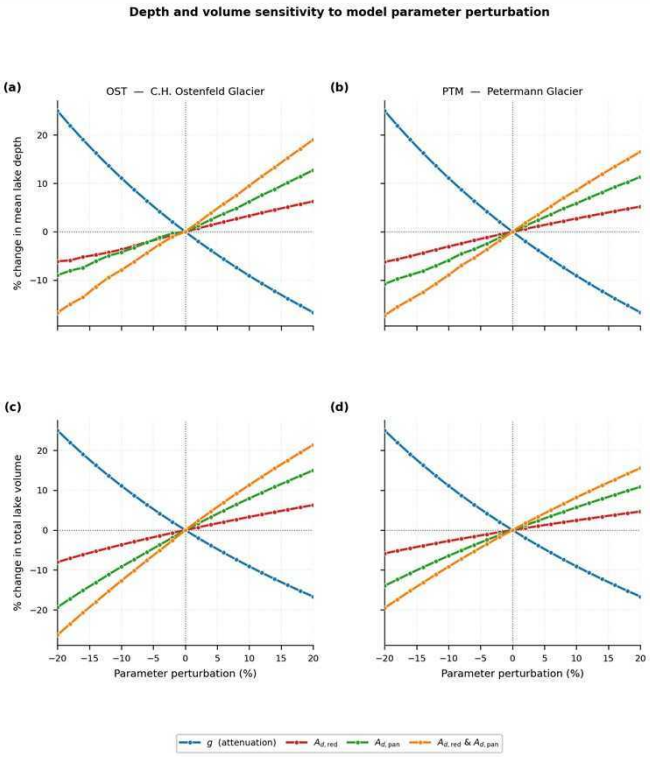

Figure 5. Per-lake volume sensitivity to $\pm 20\,\%$ perturbation of the depth-formula constants g (attenuation coefficient), A_d^{B4} (red-band lakebed albedo), A_d^{B8} (panchromatic-band lakebed albedo), and the two albedos perturbed together (A_d both). Each line is one of six representative lakes; markers show the volume change at the perturbation level on the x-axis.

5.2 Melt area, elevation, and lake volume timeseries

Annual JJA mean and maximum slush, lake, and combined area, the mean and maximum melt-feature elevation, and the lake-volume time series are shown in Fig.3. All annual values reported here are derived from the per-window direct measurements aggregated to the 10-day-block reporting basis. Across the record, both glaciers are dominated by inter-annual variability rather than a smooth secular trend. Two recent low-melt years stand out visually: Petermann 2025 has a combined-maximum area of 77 km^2, the lowest of the post-2017 portion of the record, while Ostenfeld 2024 has a combined-maximum area of 36 km^2, the lowest of the entire 12-year record and a factor of thirteen

below the Ostenfeld 2023 peak of 473 km^2. The largest single-year area at either glacier is Petermann 2023 with a combined maximum of 1495 km^2. Per-AOI per-variable annual JJA values are provided in Table 5.

Table 5. Annual JJA values per AOI, 2014–2025, observed processing, for Ostenfeld (Ost) and Petermann (Ptm). *C. max* is JJA combined-maximum area (km^2); *L. max* is JJA lake-maximum area (km^2); *C. mean elev* is JJA combined-mean melt-feature elevation (m a.s.l.); *L. max vol* is JJA lake-maximum volume Mm^3 (million m^3). Bold values are the per-AOI per-metric maxima across the record.

	C.H. Ostenfeld				Petermann			
Year	C. max	L. max	C. mean elev	L. max vol	C. max	L. max	C. mean elev	L. max vol
2014	69.8	10.7	906.5	18.0	284.6	41.2	550.1	62.1
2015	220.0	15.0	819.9	20.9	727.2	44.1	699.1	61.6
2016	69.2	9.5	755.2	16.3	132.7	40.8	422.0	74.6
2017	79.4	9.5	722.2	18.6	71.6	27.3	321.8	48.7
2018	119.8	12.1	701.1	17.6	133.5	31.2	292.4	52.0
2019	93.8	9.7	864.6	14.7	653.3	53.9	722.1	61.2
2020	72.9	12.0	802.8	18.6	177.4	36.2	528.8	63.4
2021	232.9	16.6	867.7	20.4	847.7	76.5	524.2	74.4
2022	289.6	**27.6**	844.2	**27.2**	941.9	71.2	650.7	93.6
2023	**473.5**	**29.7**	**893.4**	25.8	**1494.5**	**98.1**	**710.7**	**103.6**
2024	36.3	9.6	738.2	18.6	165.5	54.6	459.4	86.7
2025	270.7	7.7	745.9	12.4	77.1	27.1	339.6	42.7

5.2.1 Trend and change-point tests

Mann-Kendall. The Mann-Kendall (MK) trend test was applied to every per-AOI per-variable JJA series ($n = 12$ years; 28 observed series in total) (Table 6). No series attains $p < 0.05$ at this record length. Reported in τ magnitude, the strongest individual signals are: Ostenfeld slush-maximum area ($\tau = +0.364$, $p = 0.115$, the closest to significance in the dataset); Ostenfeld slush mean, combined mean, and combined maximum area ($\tau = +0.333$, $p = 0.150$); and Petermann lake-maximum area, elevation, and volume, all returning $\tau = +0.242$, $p = 0.304$. No series in the observed dataset returns a τ magnitude exceeding +0.364, and all directional signals are positive at $|\tau| \geq 0.2$.

Pettitt change-point. The Pettitt change-point test, like MK, returns $p > 0.05$ for every observed series (Table 7). Reported as descriptive K statistics and inferred change-point years rather than as significance, the change points cluster coherently in time. At Ostenfeld, the slush mean / maximum and combined mean / maximum area series all infer a shift after 2020 ($K = 21$, $p = 0.29$), while Ostenfeld lake series cluster after 2023 ($K = 16$–20, $p = 0.36$–0.62). At Petermann, the slush and combined area series locate the shift after 2018 ($K = 17$, $p = 0.54$), the lake-maximum area series after 2020 ($K = 21$, $p = 0.30$), the lake-maximum elevation after 2017 ($K = 24$, $p = 0.169$, the strongest individual elevation Pettitt signal in the dataset), and the lake-maximum volume after 2019 ($K = 20$, $p = 0.36$). The temporal convergence at Petermann among lake-maximum area, elevation, and volume in 2017–2020 is the focus of Section 5.4.

Table 6. Mann-Kendall trend test results for observed JJA melt area, melt-feature elevation, and lake volume, OST and PTM glaciers. Per year statistics derived from observed values, footprint coverage threshold 10%. τ = Kendall's tau; S = Mann-Kendall statistic; z = standardised test statistic; ns = not significant ($p > 0.05$). $n = 12$ for all series (2014–2025). Elevation values in m a.s.l.; volume values in Mm^3.

			JJA Mean				JJA Maximum			
Var.	AOI	Series	τ	S	z	p	τ	S	z	p
Melt Area										
	C.H. Ostenfeld Glacier (OST)									
		Slush	+0.333	22	1.44	ns 0.150	+0.364	24	1.58	ns 0.115
		Lake	+0.182	12	0.75	ns 0.451	+0.091	6	0.34	ns 0.732
		C.	+0.333	22	1.44	ns 0.150	+0.333	22	1.44	ns 0.150
	Petermann Glacier (PTM)									
		Slush	+0.121	8	0.48	ns 0.631	+0.152	10	0.62	ns 0.537
		Lake	+0.091	6	0.34	ns 0.731	+0.182	12	0.75	ns 0.451
		C.	+0.121	8	0.48	ns 0.631	+0.152	10	0.62	ns 0.537
Melt-Feature Elevation										
	C.H. Ostenfeld Glacier (OST)									
		Slush	−0.061	−4	−0.21	ns 0.837	−0.152	−10	−0.62	ns 0.537
		Lake	−0.182	−12	−0.75	ns 0.451	−0.030	−2	−0.07	ns 0.945
		C.	−0.061	−4	−0.21	ns 0.837	−0.152	−10	−0.62	ns 0.537
	Petermann Glacier (PTM)									
		Slush	+0.030	2	+0.07	ns 0.945	+0.152	10	+0.62	ns 0.537
		Lake	−0.121	−8	−0.48	ns 0.631	+0.242	16	+1.03	ns 0.304
		C.	−0.061	−4	−0.21	ns 0.837	+0.152	10	+0.62	ns 0.537
Lake Volume										
	C.H. Ostenfeld Glacier (OST)									
		Lake	−0.152	−10	−0.62	ns 0.537	+0.061	4	+0.21	ns 0.837
	Petermann Glacier (PTM)									
		Lake	−0.030	−2	−0.07	ns 0.945	+0.242	16	+1.03	ns 0.304

Table 7. Pettitt's change-point test results for observed JJA melt area, melt-feature elevation, and lake volume, OST and PTM glaciers. Per year statistics derived from observed values, footprint coverage threshold 10%. K = Pettitt test statistic; CP = estimated change-point year (year after which shift occurs); ns = not significant ($p > 0.05$). $n = 12$ for all series (2014–2025). Elevation values in m a.s.l.; volume values in Mm^3.

			JJA Mean			JJA Maximum		
Variable	AOI	Series	K	CP year	p	K	CP year	p
Melt Area								
	C.H. Ostenfeld Glacier (OST)							
		Slush	21	2020	ns 0.291	21	2020	ns 0.290
		Lake	20	2023	ns 0.361	16	2023	ns 0.621
		C.	21	2020	ns 0.291	21	2020	ns 0.291
	Petermann Glacier (PTM)							
		Slush	17	2018	ns 0.545	17	2018	ns 0.539
		Lake	14	2021	ns 0.759	21	2020	ns 0.300
		C.	17	2018	ns 0.545	17	2018	ns 0.539
Melt-Feature Elevation								
	C.H. Ostenfeld Glacier (OST)							
		Slush	14	2015	ns 0.753	17	2018	ns 0.535
		Lake	16	2023	ns 0.624	12	2017	ns 0.877
		C.	12	2015	ns 0.875	17	2018	ns 0.535
	Petermann Glacier (PTM)							
		Slush	17	2018	ns 0.535	18	2017	ns 0.482
		Lake	14	2023	ns 0.755	24	2017	ns 0.169
		C.	15	2018	ns 0.684	18	2017	ns 0.482
Lake Volume								
	C.H. Ostenfeld Glacier (OST)							
		Lake	12	2023	ns 0.879	15	2020	ns 0.687
	Petermann Glacier (PTM)							
		Lake	9	2018	ns 0.991	20	2019	ns 0.359

Hamed-Rao autocorrelation correction. The Hamed-Rao modified MK was applied to all twenty-eight observed series to test the robustness of the standard MK to lag-1 autocorrelation (Fig. 6). Zero significance changes were detected, with twenty-seven of twenty-eight series returning a variance-inflation factor of 1.00, indicating no measurable lag-1 autocorrelation in the raw annual aggregates. The single exception, Petermann area lake-mean, returns variance inflation of 0.36 (anti-correlation, which slightly lowers the MK p from 0.73 to 0.57). The lag-1 Spearman $\rho = 0.682$ flagged in Section 5.7 is a residual autocorrelation (current-year residual against prior-year raw response) and is statistically distinct from raw-series autocorrelation.

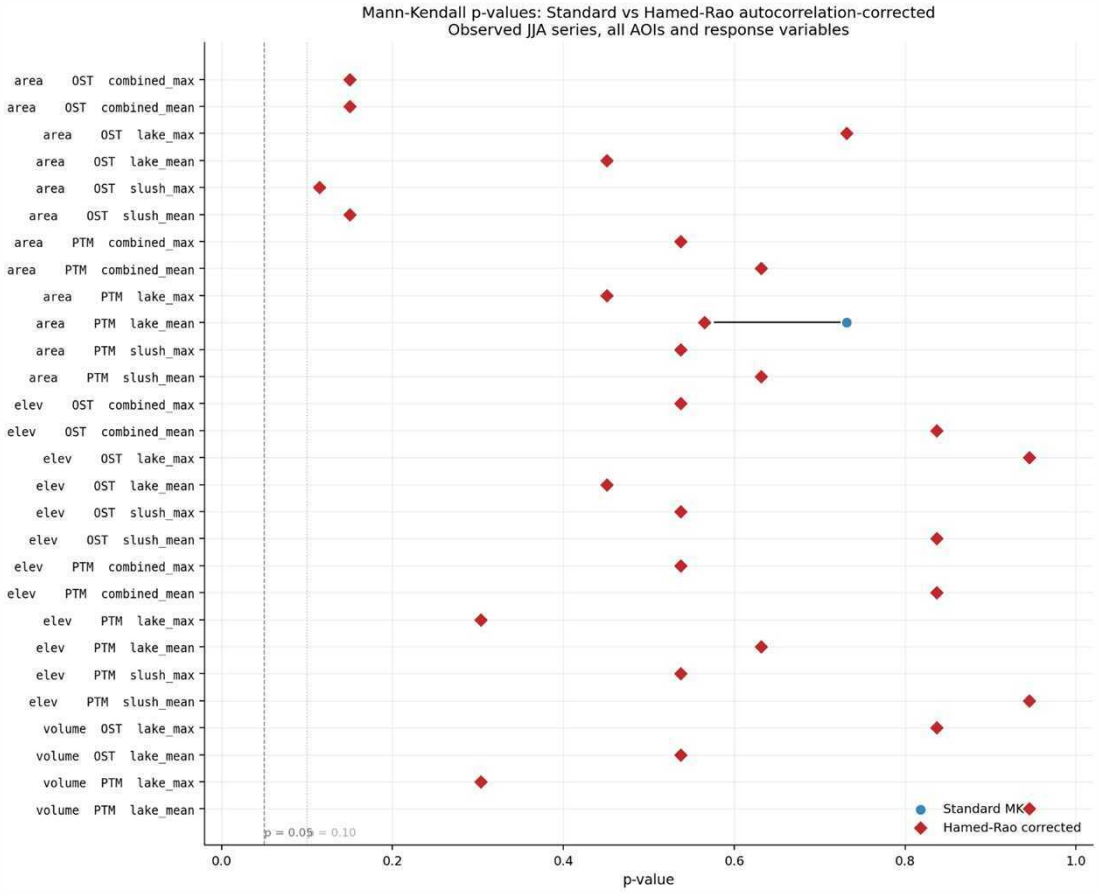

Figure 6. Comparison of p-values from the standard Mann-Kendall test (blue circles) and the Hamed-Rao autocorrelation-corrected modification (red diamonds) for all 28 observed JJA time series, spanning three response variables (area, elevation, volume), two areas of interest (Ostenfeld, Petermann), and multiple surface categories (lake, slush, combined; maximum and mean). Vertical dashed lines indicate significance thresholds at $p = 0.05$ and $p = 0.10$. For 27 of 28 series, corrected p-values are identical to the standard values. The only series showing a with shift is Petermann area lake_mean (black line), where anti-correlation in the ranked data reduces the corrected variance and lowers p from 0.73 to 0.57, without altering the significance classification.

5.3 Slush-to-lake ratio

The ratio of JJA maximum slush area to JJA maximum lake area, computed annually per AOI from 10-day blocks, ranges from 1.4 to 34.2 at Ostenfeld and from 1.8 to 15.5 at Petermann (discussed further in Section 6.6). Ostenfeld 2025 is a single extreme outlier with a ratio of 34.2, driven by a highly slush-dominant melt season (slush-maximum = 263 km^2 against lake-maximum = 7.7 km^2). Petermann peaks at 15.5 in 2015 and

Ostenfeld at 14.8 in 2023. Both glaciers have lower ratios in low-melt years: Petermann 2017 (1.8) and Ostenfeld 2024 (3.0) are the cleanest anchors. High slush dominance (ratios near 14) is reached at both glaciers in the high-melt 2023 season (Ostenfeld 14.8, Petermann 14.2). Across all twelve years, the median slush-to-lake ratio is 8.8 at Ostenfeld and 4.9 at Petermann, indicating that combined area is dominated by slush in every year at Ostenfeld, whereas at Petermann the slush:lake ratio varies between low-melt parity and high-melt slush dominance.

5.4 Period of interest, 2017 Petermann lake dynamics

Three Petermann lake-maximum series (area, elevation, and volume) share positive Mann-Kendall τ and Pettitt change points clustered in the 2017–2019 window (Table 6, Table 7). The convergence is discussed in Section 6.5.

5.5 Anomaly analysis, and baseline selection

Baseline selection Baseline windows for the anomaly analysis were selected automatically by ranking all contiguous 3-year windows on (i) at least three valid 5-window blocks per year, (ii) per-window AOI footprint coverage of at least 20 % per year, and (iii) no year above the 75th-percentile combined-maximum area, with eligible windows ranked by lowest coefficient of variation. The selected window is 2017-2018-2019 at Ostenfeld and 2016-2017-2018 at Petermann (Table 8). The same baseline window is applied to every area, elevation, and volume metric in this section so all anomalies are mutually comparable. Because the algorithm by design excludes high-melt years, the selected baseline is dominated by the lowest-melt years of the record, and recent-year anomalies are reported relative to a low baseline.

Table 8. Baseline-period means by AOI and metric family, for Ostenfeld (Ost) and Petermann (Ptm). All rows use the same 3-year baseline per AOI (2017–2018–2019 Ost, 2016–2017–2018 Ptm). Values in km^2 for area, m a.s.l. for elevation, and Mm^3 (million m^3) for volume.

Family	AOI	comb. max	comb. mean	slush max	slush mean	lake max
Area (km^2)	Ost	97.67	25.80	87.25	20.48	10.43
Area (km^2)	Ptm	112.62	50.74	82.41	32.64	33.11
Elev (m a.s.l.)	Ost	1488.88	762.63	1488.88	792.64	1328.74
Elev (m a.s.l.)	Ptm	1497.01	345.40	1497.01	416.99	1363.76
Volume (Mm^3)	Ost	–	–	–	–	17.01
Volume (Mm^3)	Ptm	–	–	–	–	58.44

The sensitivity of the major 2023 anomaly to baseline choice is given in Table 9 and shown in Fig. 7. The four baseline definitions are described in Section 4.6.3. Ostenfeld anomalies are robust across all four baseline definitions (×2.8-fold to ×4.9-fold for 2023), while the Petermann 2023 fold-anomaly varies between ×3.1-fold and ×13.3-fold depending on which reference period is used. Petermann 2023 was 3–13× the pre-high-melt-regime baseline, with the ×13.3 figure being the most baseline-dependent number in the dataset.

Table 9. Sensitivity of the 2023 melt anomaly to baseline choice, for Ostenfeld (Ost) and Petermann (Ptm). Ostenfeld anomalies are robust across all four baseline definitions. The Petermann 2023 ×13.3 anomaly is the most dependent on the algorithm-selected baseline. Bold values are the Petermann 2023 fold anomalies under each baseline definition.

Baseline	Ost base (km^2)	Ptm base (km^2)	Ost 2023 fold	Ptm 2023 fold
Algorithm (CV)	98	113	×4.9	×**13.3**
Pre-2020 mean	109	334	×4.4	×**4.5**
Record median	107	231	×4.4	×**6.5**
Full-record mean	169	476	×2.8	×**3.1**

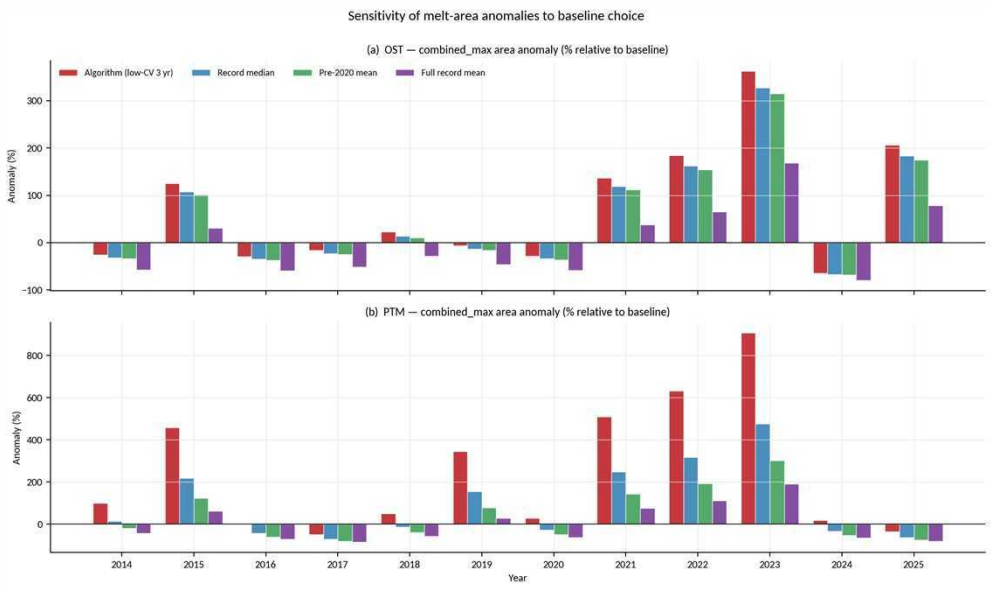

Figure 7. Annual combined-maximum area anomaly (%) relative to four alternative baseline definitions for Ost. (a) and Ptm. (b). The algorithm-selected baseline (red) produces the largest Ptm. anomalies. The full-record mean (purple) produces the most conservative estimates. Pre-2020 mean (green) and full record median (blue) are consistently between the CV and record mean poles. Ost. anomalies follow the same pattern but are more consistent across all definitions with less variation from baseline choice.

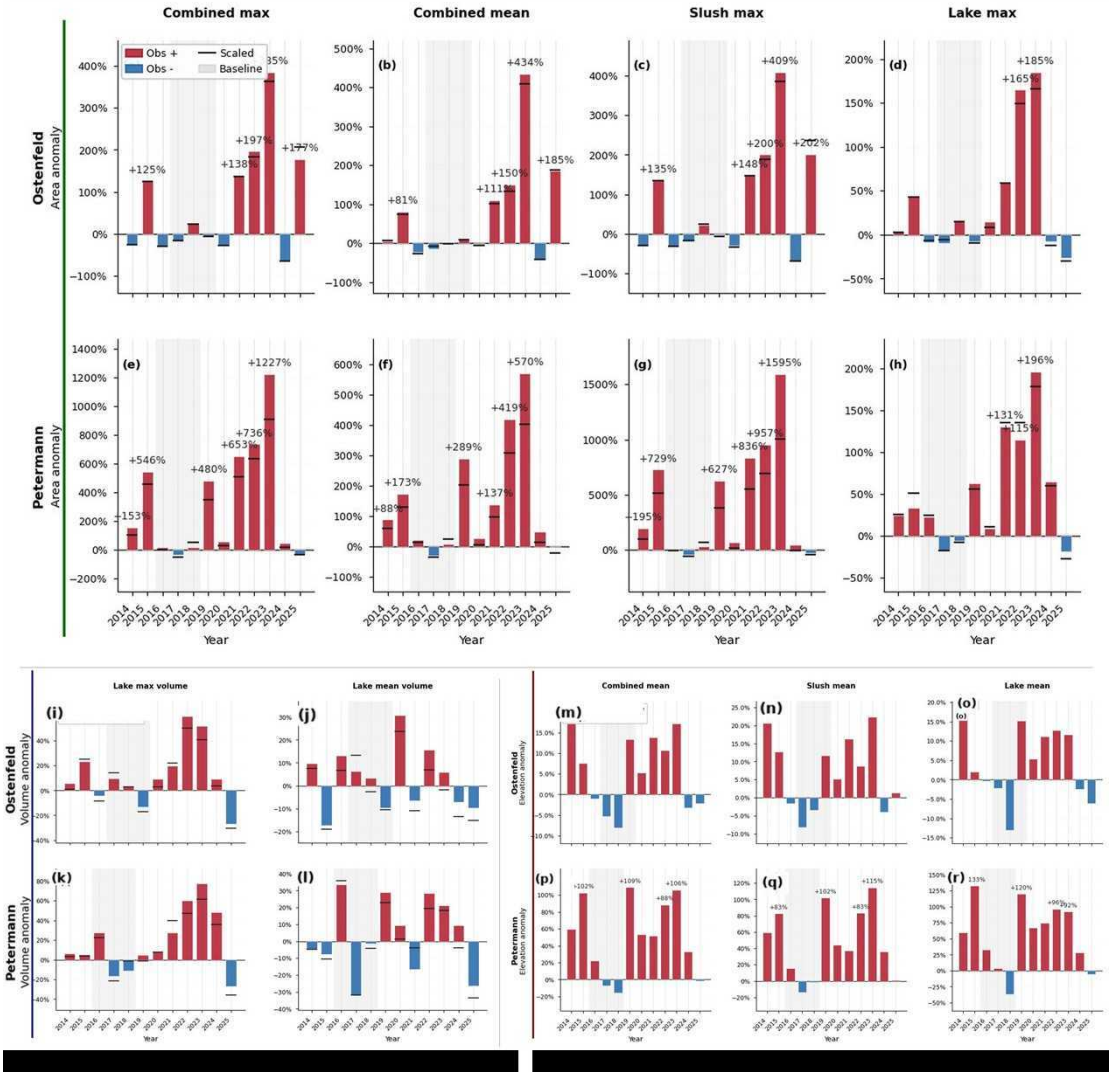

Figure 8. Annual JJA area anomalies, volume anomalies, and elevation anomalies relative to the lowest coefficient of variance baseline (2017–2019 Ostenfeld, 2016–2018 Petermann), for Ostenfeld (top rows) and Petermann (bottom rows). Colored bars show the positive anomaly (red) and negative anomaly (blue). The baseline window is shaded grey. ***Area anomalies (a–h)*** are given for combined-maximum area (a, e), mean area (b, f), maximum slush (c, g), and lake area (d, h). Petermann combined-maximum area anomaly (e) in 2023 is +1227%, followed by near-baseline melt area in 2024 with a moderate Petermann lake-area anomaly (h). Ostenfeld combined-maximum area (a) is +385% above baseline, and moderately below baseline in 2024. ***Volume anomalies (i–l)*** are measured in maximum (i, k) and mean (j, l) annual volume. The lake-maximum drained volume peaks in 2023 and 2022 at both Petermann and Ostenfeld. Mean-volume anomaly distribution is more sporadic. ***Elevation anomalies (m–r)*** at Petermann 2015, 2019, and 2023 reach roughly twice the baseline mean. The Ostenfeld anomalies are smaller in relative terms because the Ostenfeld baseline mean elevation is higher and maxima extend beyond study area boundary in most years. A black tick mark at each year marks scaled anomaly (not discussed). For scaled data see appendix E.

5.5.1 Annual area anomalies

Combined-maximum area. The two AOIs share the 2022–2023 high-melt regime but diverge sharply in 2024 (Ostenfeld collapses, Petermann partially recovers) and again in 2025 (Ostenfeld rebounds to ×2.8, Petermann falls below baseline). The area anomalies are shown in panels (a)–(h) of Fig. 8 for four metrics (combined maximum, combined mean, slush maximum, lake maximum). Annual combined-maximum area anomalies are shown in Table 10.

Table 10. Annual combined-maximum area anomalies relative to the algorithm-selected baseline (% and fold-change), for Ostenfeld (Ost) and Petermann (Ptm). Baseline years (italicised) are shown for completeness; their per-row deviations are by construction smaller than non-baseline rows. Bold values are the single most extreme positive (Ptm 2023) and negative (Ost 2024) anomalies in the table.

Year	Ost	Ptm
2014	−28.5% (×0.71)	+152.7% (×2.53)
2015	+125.3% (×2.25)	+545.7% (×6.46)
2016	−29.2% (×0.71)	*+17.8%* (×1.18)
2017	*−18.7%* (×0.81)	*−36.4%* (×0.64)
2018	*+22.6%* (×1.23)	*+18.6%* (×1.19)
2019	*−3.9%* (×0.96)	+480.1% (×5.80)
2020	−25.4% (×0.75)	+57.5% (×1.58)
2021	+138.5% (×2.38)	+652.7% (×7.53)
2022	+196.5% (×2.97)	+736.4% (×8.36)
2023	**+384.8% (×4.85)**	**+1227.1% (×13.27)**
2024	**−62.8% (×0.37)**	+47.0% (×1.47)
2025	+177.1% (×2.77)	−31.5% (×0.69)

Combined-mean area. For combined-mean area the strongest anomalies are: Petermann 2023 +569.9%; Petermann 2022 +419.1%; Petermann 2019 +288.5%; Ostenfeld 2023 +434.2%; Ostenfeld 2025 +185.1%; Ostenfeld 2022 +149.8%.

Slush-lake decomposition. The combined-maximum area anomaly is dominated by the slush component at both AOIs (Fig. 8, panels (c), (d), (g), and (h)). Petermann slush-maximum 2023 anomaly is 1594.5 % (×16.95), set against Petermann lake-maximum 2023 of 196.3 % (×2.96). At Ostenfeld 2023, slush-maximum anomaly is 408.7 % (×5.09) vs lake-maximum 184.7 % (×2.85). At every year above the 50 % anomaly threshold, the slush component carries two-to-five times the magnitude of the lake component. This is consistent with the slush-to-lake ratio observation in Section 5.3 that slush is the largest melt area component at both glaciers, more strongly at Ostenfeld.

The 2024 Petermann divergence is notable. Combined-maximum 47.0 % is a low-positive year, but lake-maximum is 65.0 % (high) while slush-maximum is 44.4 % (low). The combined-maximum metric averages these two opposing signals to a small positive number. This is the area component of the 2024 Petermann area-versus-drainage decoupling described later in Section 5.10.

The 2025 Ostenfeld asymmetry shows the converse behavior, with a combined maximum anomaly of 177.1 %, indicating a strongly positive deviation. This response is mainly controlled by a slush-maximum anomaly of 202.0 %, while the lake-maximum anomaly drops to −26.1 %, constituting the lowest single-year lake-area anomaly ob-

served at Ostenfeld. Consequently, during the 2025 rebound phase, slush constitutes the dominant temporary storage component at Ostenfeld.

5.5.2 Lake-volume and elevation anomalies

The same baseline window (2017–2019 Ostenfeld, 2016–2018 Petermann) is applied to volume for cross-family consistency with the area subsection. Annual lake-volume anomalies are shown in Table 11; the matching volume-anomaly panels are shown in Fig. 8 panels (i)–(l).

Petermann single-year volume anomaly is +77.3% (×1.77). This is the volume component of the Petermann 2023 anomaly but represents a smaller multiple of the baseline (×1.77) than the corresponding combined-maximum area anomaly (×13.3). The volume anomaly is dampened relative to the area anomaly because lake-volume scales more slowly than slush + lake area.

For lake-mean volume the year-to-year spread is much smaller. The largest positives are Petermann 2016 *+33.4%* (baseline year), Petermann 2019 +28.9%, Petermann 2022 +28.4%; negatives are Petermann 2017 *−32.1%* (baseline year), Petermann 2025 −26.3%, Ostenfeld 2015 −17.3%.

Table 11. Annual lake-maximum volume anomalies relative to the algorithm-selected baseline (% and fold-change), for Ostenfeld (Ost) and Petermann (Ptm). Ptm 2023 is the strongest single-year volume anomaly; Ptm 2024 is the year of the largest area-vs-volume divergence (high volume despite low combined-area) Largest anomalies are bold.

Year	Ostenfeld		Petermann	
2014	+5.6%	(×1.06)	+6.2%	(×1.06)
2015	+23.0%	(×1.23)	+5.4%	(×1.05)
2016	−4.1%	(×0.96)	*+27.7%*	(×1.28)
2017	*+9.6%*	(×1.10)	*−16.7%*	(×0.83)
2018	*+3.7%*	(×1.04)	*−11.0%*	(×0.89)
2019	*−13.3%*	(×0.87)	+4.7%	(×1.05)
2020	+9.3%	(×1.09)	+8.5%	(×1.09)
2021	+19.7%	(×1.20)	+27.3%	(×1.27)
2022	**+59.7%**	**(×1.60)**	+60.2%	(×1.60)
2023	+51.7%	(×1.52)	**+77.3%**	**(×1.77)**
2024	+9.3%	(×1.09)	**+48.4%**	**(×1.48)**
2025	−26.9%	(×0.73)	−27.0%	(×0.73)

Elevation anomalies Elevation anomalies (Table 12) are reported on the same baseline window as the area and volume products. At Ostenfeld the slush-maximum and combined-maximum series sit within ±1.5 % of the 1500 m AOI boundary across every year of the record (range 1471 to 1501 m); the implications of this for interpretation are discussed in Section 6.3. Mean elevations carry the interpretable signal at both sites, with the matching anomaly panels shown in Fig. 8 panels (m)–(r); annual Petermann values are given in Table 12.

Petermann combined-mean elevation anomalies are high in 2015, 2019, and 2023, with combined-means close to or greater than twice the baseline (102.4 %–109.1 %; ×2.02–×2.09). The slush-mean behaves similarly, with its strongest anomalies in 2023, 2019,

and 2022 (83.2 %–114.5 %). Lake-mean elevations peak in 2015 and 2019 (119.9 %–132.7 %; ×2.20–×2.33), consistent with mid-elevation lakes reaching high absolute elevations against a small baseline mean (273.8 m, dominated by the low-melt 2016–2018 window). Because that baseline mean is small, percent anomalies can appear inflated; Table 12 therefore reports both % anomalies and absolute m values.

Ostenfeld combined-mean elevation anomalies are smaller in relative terms (−13.1 % to 18.9 %) because the Ostenfeld baseline mean (762.6 m) is larger and the year-to-year spread is narrower. The strongest positive years are 2014 (18.9 %), 2023 (17.1 %), 2021 (13.8 %); the strongest negative is 2018 (−8.1 %, baseline year). The Ostenfeld signal is the counterpart to the Petermann "melt-elevation expansion" but is smaller in fractional terms.

Table 12. Petermann (Ptm) annual JJA mean-elevation anomalies (observed only) relative to the 2016–2018 baseline. Combined-mean, slush-mean, and lake-mean reach roughly twice the baseline in the strongest years (2015, 2019, 2023). Both the percent anomaly and the absolute value (m a.s.l.) are shown because the small baseline-period mean inflates the relative anomalies.

	Combined mean		Slush mean		Lake mean	
Year	%	m a.s.l.	%	m a.s.l.	%	m a.s.l.
2014	+59.3	550.1	+59.2	663.9	+59.3	436.3
2015	**+102.4**	699.1	+82.5	761.0	**+132.7**	637.2
2016	*+22.2*	421.9	*+15.3*	480.7	*+32.6*	363.2
2017	*−6.8*	321.8	*−13.8*	359.4	*+3.8*	284.3
2018	*−15.3*	292.4	*−1.5*	410.8	*−36.5*	174.0
2019	**+109.1**	722.1	**+101.9**	842.0	**+119.9**	602.2
2020	+53.1	528.8	+44.2	601.2	+66.7	456.4
2021	+51.8	524.2	+36.9	571.0	+74.4	477.4
2022	+88.4	650.7	+83.2	763.9	+96.3	537.5
2023	**+105.8**	710.7	**+114.5**	894.5	+92.5	527.0
2024	+33.0	459.4	+36.0	567.0	+28.5	351.8
2025	−1.7	339.6	+0.9	420.5	−5.5	258.7

5.6 Climate forcing

5.6.1 Per-AOI Pearson correlations

For each AOI, OSL fits of annual JJA melt-response metrics against aggregated ERA5-Land JJA predictors are summarized by Pearson R^2 and two-tailed p-values. The strongest statistical result in the dataset is the per-AOI coupling between JJA maximum (single-day peak) ERA5-Land 2 m air temperature (T_{2m} JJA max) and JJA maximum melt response at Petermann. Petermann combined-maximum area regressed against T_{2m} JJA maximum gives $R^2 = 0.85$ ($p = 2.2 \times 10^{-5}$), Petermann slush-maximum area $R^2 = 0.85$ ($p = 2.3 \times 10^{-5}$), and Petermann lake-maximum area $R^2 = 0.69$ ($p = 8.4 \times 10^{-4}$). Petermann lake-maximum volume against T_{2m} JJA maximum sits just above the conventional threshold ($R^2 = 0.32$, $p = 0.053$). Petermann slush-maximum and combined-maximum elevation against T_{2m} JJA maximum give $R^2 = 0.36$ ($p = 0.039$). The corresponding Ostenfeld relationships are weaker in comparison. Ostenfeld combined-maximum area $R^2 = 0.25$ ($p = 0.10$), Ostenfeld lake-maximum area $R^2 = 0.28$ ($p =$

0.08), and Ostenfeld lake-maximum volume $R^2 = 0.16$ ($p = 0.19$). One negative trending result is the Ostenfeld T_{2m} mean against slush-maximum elevation ($r = -0.794$, $p = 0.002$). Interpretation is discussed in Section 6.3.

JJA mean predictors are weaker than JJA maximum predictors. At Petermann, T_{2m} JJA mean against combined-maximum area returns $R^2 = 0.04$ ($p = 0.51$), set against $R^2 = 0.85$ for the peak-temperature predictor. Downwelling shortwave predictors (SW↓ JJA mean and max) are also weaker than T_{2m} at both AOIs, with all 28 SW combinations returning $p > 0.10$. The inter-glacier asymmetry in the peak-temperature regressions is interpreted in Section 6.3. The condensed 28-combination $R^2 + p$ table covering all four predictor families, both AOIs, and the seven response variables is provided in Table 13. Scatter plots for (T_{mean}, T_{max}), (SW_{mean}, SW_{max}) against all maximum melt metrics are given in appendix B.

Table 13. ERA5-Land R^2 summary, $n = 12$ years (2014–2025), per-AOI OLS regression of each JJA response on each JJA climate predictor, for Ostenfeld (Ost) and Petermann (Ptm). Cells are R^2; significance: *** $p < 0.001$, ** $p < 0.01$, * $p < 0.05$, no mark $p \geq 0.05$. The four predictor families are JJA mean and JJA maximum 2 m air temperature (T_{mean}, T_{max}) and downwelling shortwave (SW_{mean}, SW_{max}). The seven responses are slush, lake, and combined area (each with mean and max), plus lake volume max. Ptm peak-temperature couplings (column 2) are the strongest results in the dataset; Ost shows weaker and noisier coupling on the same axes.

	Ost				Ptm			
Response	T_{mean}	T_{max}	SW_{mean}	SW_{max}	T_{mean}	T_{max}	SW_{mean}	SW_{max}
Slush mean (km^2)	0.00	0.22	0.00	0.01	0.04	0.67**	0.07	0.05
Slush max. (km^2)	0.01	0.25	0.01	0.02	0.04	0.85***	0.08	0.12
Lake mean (km^2)	0.01	0.30	0.04	0.02	0.10	0.36*	0.06	0.05
Lake max. (km^2)	0.00	0.28	0.01	0.08	0.10	0.69***	0.00	0.11
Combined mean (km^2)	0.00	0.23	0.00	0.01	0.04	0.66**	0.07	0.05
Combined max. (km^2)	0.01	0.25	0.01	0.03	0.04	0.85***	0.08	0.12
Lake max. vol (Mm^3)	0.01	0.16	0.03	0.09	0.07	0.32	0.01	0.12

5.6.2 ERA5 climate context

The Petermann JJA T_{2m} maximum ranges from 0.7 °C (2013) to 4.6 °C (2023); the 2024 (1.5 °C) and 2025 (1.4 °C) values sit at the cool end of the record, consistent with the post-2023 melt collapse in Fig. 3. The Ostenfeld JJA T_{2m} maximum ranges from 3.1 °C (2013) to 7.7 °C (2021); 2024 (3.8 °C) and 2025 (4.2 °C) are mid-low. Petermann JJA T_{2m} mean stays negative throughout the record (−4.7 to −1.8 °C). Annual JJA mean and maximum T_{2m} at both AOIs are shown in Fig. 9; the matching downward-shortwave context figure is provided as supplementary.

5.7 Analog pair, lag correlation, and recovery rate analysis

Analog pairs. Analog pair analysis finds years with similar climate forcing but different melt response. A flagged pair indicates that, despite similar climate (predictor) conditions, the melt response of the two years deviated from the climate–melt OLS fit (Eq. 2, Section 4.6.4) by a substantial amount, meaning the climate-corrected melt responses differ strongly. Larger flag counts mean the same pair recurs across more

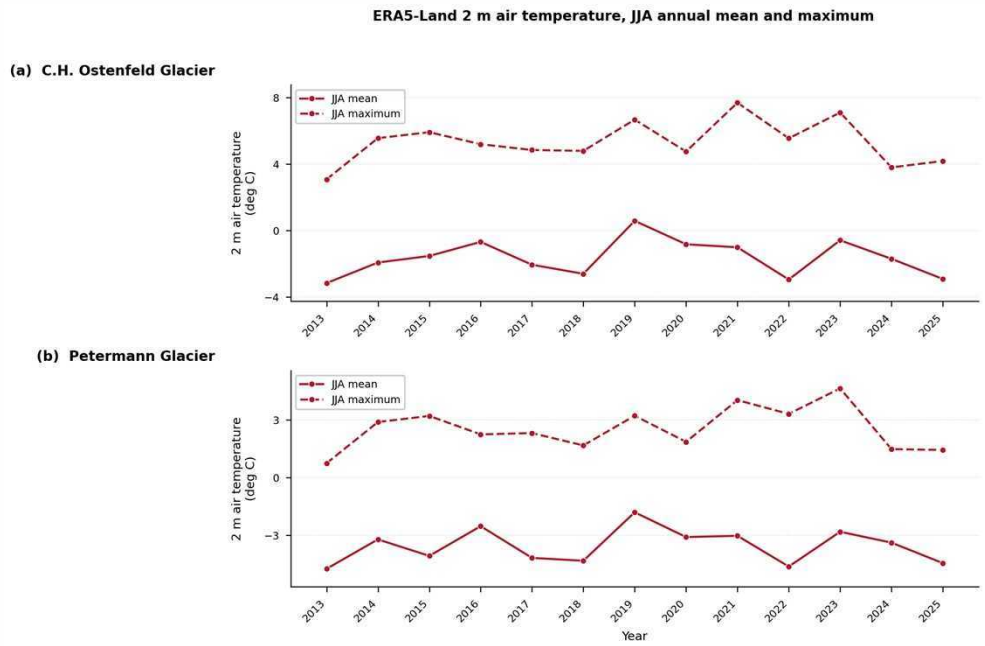

Figure 9. ERA5-Land annual JJA mean and maximum 2 m air temperature (T_{2m}) at Ostenfeld (top) and Petermann (bottom) for 2013–2025. Petermann remains below 0 °C in JJA mean across the entire record.

predictor / response combinations. A pair was flagged when the absolute difference in predictor z-score was less than 0.5 SD and the absolute difference in climate-corrected response z-score exceeded 1.0 SD (Eq. 3, Section 4.6.4). A total of 846 pair flags were produced across the 56 AOI-specific combinations. The most-flagged pairs, where the count is the number of predictor / response combinations in which the pair was flagged, are Petermann 2021–2023 (32 flags, the most-flagged pair in the dataset), Petermann 2018–2022 (26), Ostenfeld 2016-2023 (26), Petermann 2023-2025 (24), Petermann 2016–2023 (24), and Ostenfeld 2019–2023 (24). The top-five analog-pair scatter is interpreted in Section 6.6. The top-fifteen most-flagged pairs are shown in Table 14.

Lag-1 residual correlation. The Spearman rank correlation between the current-year climate-corrected melt response (Eq. 2) and the prior-year raw response was computed for $n = 11$ years, separately for each AOI / predictor / response combination (Table 15). One coefficient is significant at $p < 0.05$. Petermann area against T_{2m} JJA maximum as predictor, with lake-maximum area as response, returns $\rho_{\text{lag1}} = 0.682$ ($p = 0.021$). Two further Petermann area combinations are near-significant. T_{2m} JJA maximum against Petermann slush-maximum and combined-maximum area both return $\rho_{\text{lag1}} = 0.555$ ($p = 0.077$). All Ostenfeld lag correlations have $p > 0.21$.

5.8 Recovery-rate analysis

Recovery rates are the trough-to-peak OLS slopes of annual JJA combined-mean melt area versus year, computed on the raw series and on the climate-corrected melt response from the per-AOI climate–melt OLS fits (Eq. 2). Per-AOI fits give Petermann T_{max} $R^2 = 0.66$ (adj. 0.62) and T_{max} + SW_{mean} $R^2 = 0.69$ (adj. 0.62). Ostenfeld T_{max} $R^2 = 0.23$ (adj. 0.15) and T_{max} + SW_{mean} $R^2 = 0.26$ (adj. 0.09). Cycle slopes under raw, T_{mean}-, T_{max}-, and T_{max} + SW_{mean}-corrected fits are summarised in Table 16 and shown in Fig. 10.

Table 14. Top 15 most-flagged analog pairs in the hysteresis screen, for Ostenfeld (Ost) and Petermann (Ptm). A pair (year a, year b) is flagged within a predictor / response combination when the predictor is similar ($|\Delta z_{\mathrm{met}}| < 0.5$ SD) but the climate-corrected response differs ($|\Delta z_{\mathrm{resid}}| > 1.0$ SD). Count is the number of (predictor, response) combinations in which the pair was flagged (maximum 56 per AOI). 2023 appears in 8 of the top 15 pairs.

Rank	AOI	Year a	Year b	Flags
1	Ptm	2021	2023	32
2	Ost	2016	2023	26
3	Ptm	2018	2022	26
4	Ost	2019	2023	24
5	Ptm	2016	2023	24
6	Ptm	2023	2025	24
7	Ost	2016	2022	22
8	Ost	2020	2023	20
9	Ost	2020	2025	20
10	Ptm	2021	2025	17
11	Ost	2016	2021	16
12	Ost	2015	2017	14
13	Ost	2017	2018	14
14	Ost	2018	2023	13
15	Ost	2023	2024	13

Table 15. Lag-1 residual Spearman correlation between current-year climate-corrected melt response (Eq. 2) and the prior-year raw response, for Ostenfeld (Ost) and Petermann (Ptm). $n = 11$. Cells are Spearman ρ_{lag1}, marked with * at $p < 0.05$ and unmarked at $p \geq 0.05$. Petermann slush, combined and lake area maxima against T_{max} are the strongest positive results, with lake maximum the only signal with conventional significance ($\rho_{\mathrm{lag1}} = +0.682, p = 0.021$).

	Ost				Ptm			
Response	T_{mean}	T_{max}	$\mathrm{SW}_{\mathrm{mean}}$	$\mathrm{SW}_{\mathrm{max}}$	T_{mean}	T_{max}	$\mathrm{SW}_{\mathrm{mean}}$	$\mathrm{SW}_{\mathrm{max}}$
Slush mean (km^2)	−0.14	+0.22	−0.14	−0.15	−0.11	+0.36	+0.17	+0.10
Slush max. (km^2)	−0.09	−0.03	−0.11	−0.26	+0.07	+0.55	+0.36	+0.15
Lake mean (km^2)	+0.25	+0.41	+0.28	+0.29	−0.15	−0.05	−0.14	−0.05
Lake max. (km^2)	+0.35	+0.31	+0.39	+0.22	+0.35	**+0.68***	+0.29	+0.22
Combined mean (km^2)	−0.14	+0.25	−0.14	−0.10	+0.00	+0.36	+0.17	+0.10
Combined max. (km^2)	−0.04	−0.01	−0.13	−0.23	+0.15	+0.55	+0.36	+0.25
Lake max. vol (Mm^3)	+0.20	+0.36	+0.22	+0.08	+0.41	+0.24	+0.35	+0.38

Across both AOIs, cycle slopes vary with the choice of climate correction (Table 16, Fig. 10). At Ostenfeld, the cycle 1 slope is small and positive in the raw and T_{mean} fits (3.4 and 3.3 $\mathrm{km}^2\ \mathrm{yr}^{-1}$, respectively) but is negative under T_{max}-based correction (−9.5 and −14.4 $\mathrm{km}^2\ \mathrm{yr}^{-1}$ for T_{max} and T_{max} + $\mathrm{SW}_{\mathrm{mean}}$, respectively). Ostenfeld cycle 2 remains positive under all fits (raw 34.6 $\mathrm{km}^2\ \mathrm{yr}^{-1}$, corrected 27.7 to 28.3 $\mathrm{km}^2\ \mathrm{yr}^{-1}$ under T_{max}-based models). At Petermann, both cycles remain positive under all fits. Cycle 1 decreases from 80.7 $\mathrm{km}^2\ \mathrm{yr}^{-1}$ (raw) to 46.7 $\mathrm{km}^2\ \mathrm{yr}^{-1}$ (T_{max}-corrected), and cycle 2 decreases from 96.9 $\mathrm{km}^2\ \mathrm{yr}^{-1}$ (raw) to 39.6 $\mathrm{km}^2\ \mathrm{yr}^{-1}$ (T_{max}-corrected).

Table 16. Recovery-rate slopes ($\mathrm{km}^2\ \mathrm{yr}^{-1}$) for the two cycles at each AOI, under raw and three climate-corrected fits, for Ostenfeld (Ost) and Petermann (Ptm).

AOI	Cycle	Years	Raw	T_{mean}	T_{max}	T_{max} + $\mathrm{SW}_{\mathrm{mean}}$
Ost	1	2017–2019	+3.4	+3.3	−9.5	−14.4
Ost	2	2020–2023	+34.6	+34.6	+27.7	+28.3
Ptm	1	2017–2019	+80.7	+53.3	+46.7	+34.5
Ptm	2	2020–2023	+96.9	+98.7	+39.6	+47.3

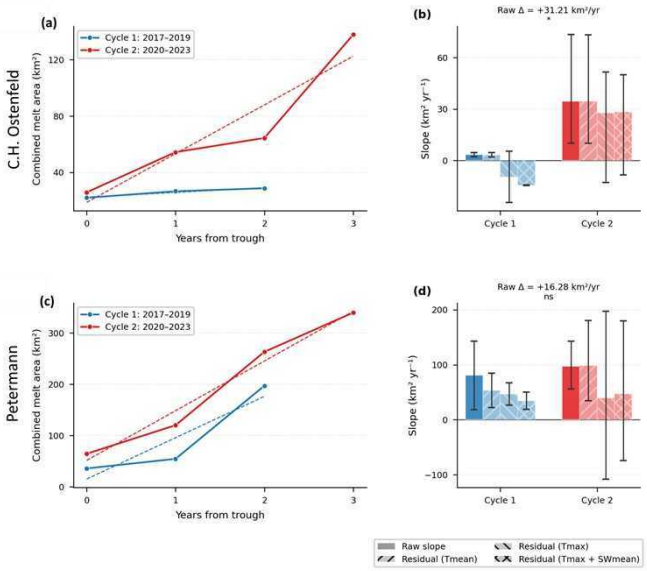

Figure 10. Recovery-rate analysis for annual JJA combined-mean melt area at (a–b) C.H. Ostenfeld Glacier and (c–d) Petermann Glacier. Panels (a) and (c) show the two trough-to-peak windows (cycle 1 covers 2017–2019 and cycle 2 covers 2020–2023) as years since the cycle trough, with dashed lines indicating OLS fits. Panels (b) and (d) summarise cycle slopes ($\mathrm{km}^2\ \mathrm{yr}^{-1}$) for raw area and for the climate-corrected melt response after removing linear associations with ERA5 T_{mean}, T_{max}, and T_{max} + $\mathrm{SW}_{\mathrm{mean}}$. Error bars are 95 % bootstrap CIs. Annotated Δ values indicate the raw difference in slope between cycles (cycle 2 minus cycle 1), with significance as marked.

5.9 Spatial structure of melt

Persistency scores. Both slush and lakes are persistent in the southwest and unrepresented in the northeastern sectors of both study areas Fig 11. Slush occurs over a wider area of both study area but is less persistent year-to-year while lakes are strongly confined, recurring over a smaller area with high persistency (Fig. 11).

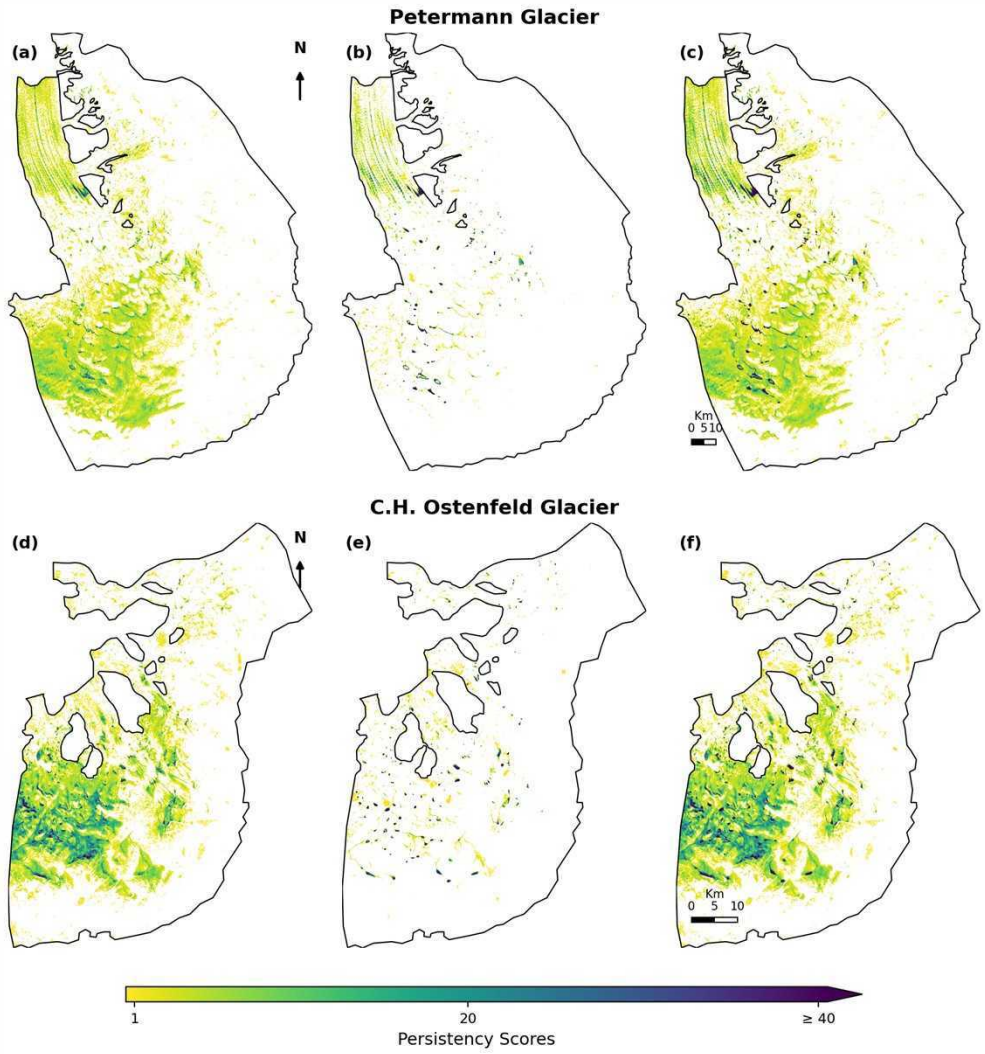

Figure 11. Melt persistency heatmap for Petermann (top row), and Ostenfeld (bottom row) for slush ((a), (d)), lakes ((b), (e)), and combined ((c), (f)). Pixel value is the count of 2-day windows in 2014–2025 in which the pixel was classified as lake, or slush. Values have been normalized to 40 and symbolized yellow (low) to purple (high). AOIs are not to scale, see scale bars. Persistent melt at both glaciers occupies a western to southwestern zone in each study area, while the eastern interior remains underrepresented across the twelve years. *(CRS: EPSG:3413, WGS 84 / NSIDC Sea Ice Polar Stereographic North)*

Classified block maps. The annual maximum-melt block maps (Fig. 12, Fig. 13) contrast clearly between high-melt years (2019, 2022 at Petermann; 2023 at Ostenfeld) and low-melt years (2017, 2024), and highlight the extreme 2023 melt extent on Petermann.

RGB medoid mosaics. The annual maximum-melt RGB composites (Fig. 14, Fig. 15) provide a visual reference alongside the classified block maps and the quantitative time series (Fig. 3), illustrating the inter-annual range in melt extent at both glaciers.

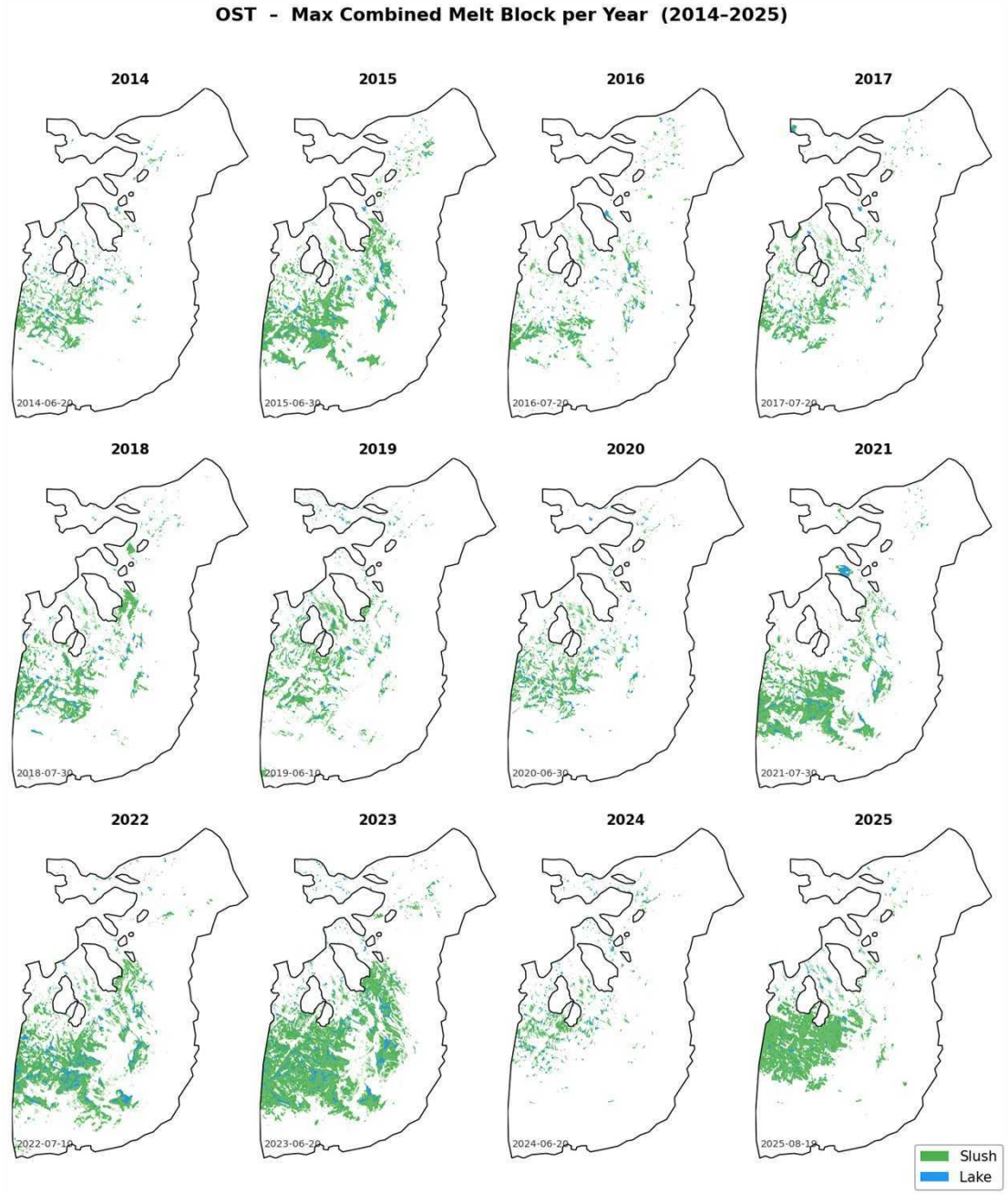

Figure 12. The 10-day block for each study year with maximum lake (blue) and slush (green) by combined area for Ostenfeld, 2014–2025. Each panel shows 10-day block vectors overlaid on the study area polygon. The block start date for each year is printed along the panel bottom. *(CRS: EPSG:3413, WGS 84 / NSIDC Sea Ice Polar Stereographic North)*

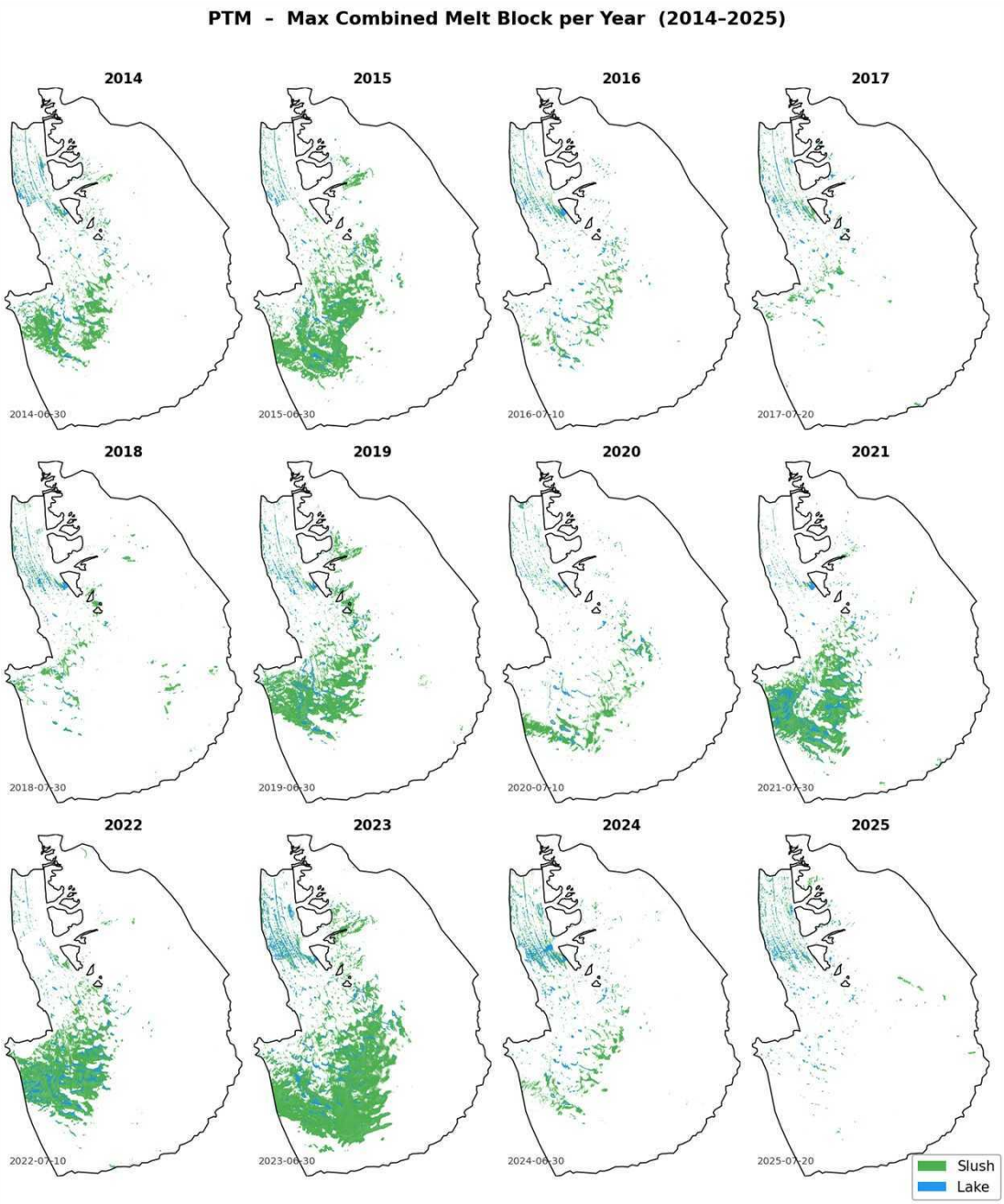

Figure 13. The 10-day block for each study year with maximum lake (blue) and slush (green) by combined area for Petermann, 2014–2025. Each panel shows 10-day block vectors overlaid on the study area polygon. The block start date for each year is printed along the panel bottom. *(CRS: EPSG:3413, WGS 84 / NSIDC Sea Ice Polar Stereographic North)*

Figure 14. Annual JJA maximum-melt RGB medoid mosaics for Ostenfeld, 2014–2025. Each panel shows the median pixel reflectance over the 2-day window with the maximum combined area in that year. *(CRS: EPSG:3413, WGS 84 / NSIDC Sea Ice Polar Stereographic North)*

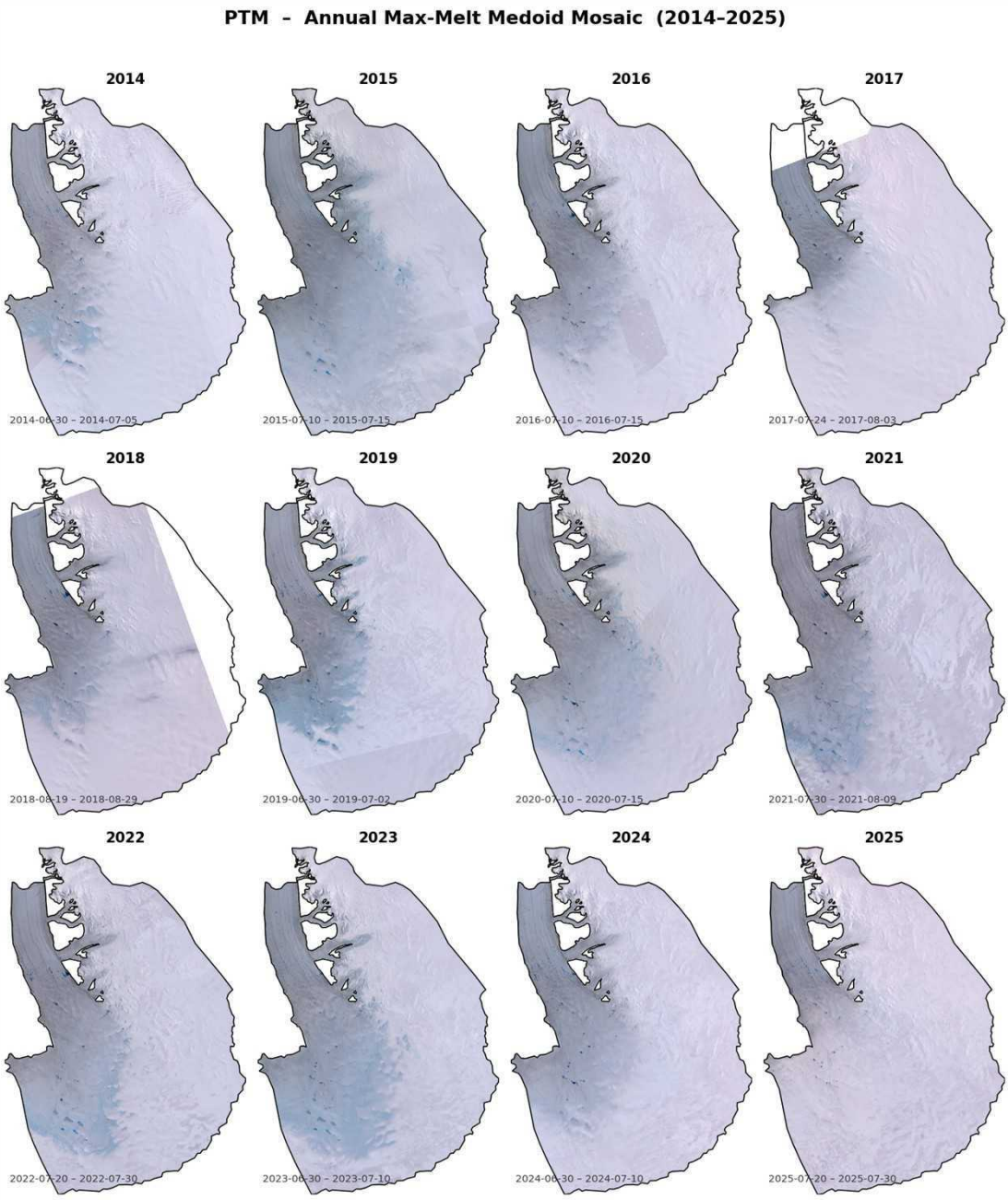

Figure 15. Annual JJA maximum-melt RGB medoid mosaics for Petermann, 2014–2025. Each panel shows the median pixel reflectance over the 2-day window with the maximum combined area in that year.*(CRS: EPSG:3413, WGS 84 / NSIDC Sea Ice Polar Stereographic North)*

5.9.1 Persistent-lake spatial inventory

The persistent-lake inventory (Section 4.6.5) identifies 57 lakes at Petermann and 46 at Ostenfeld; of these, 29 and 22 have at least one full drainage event over the record respectively, while the remainder show no recorded full drainage (Fig. 16).

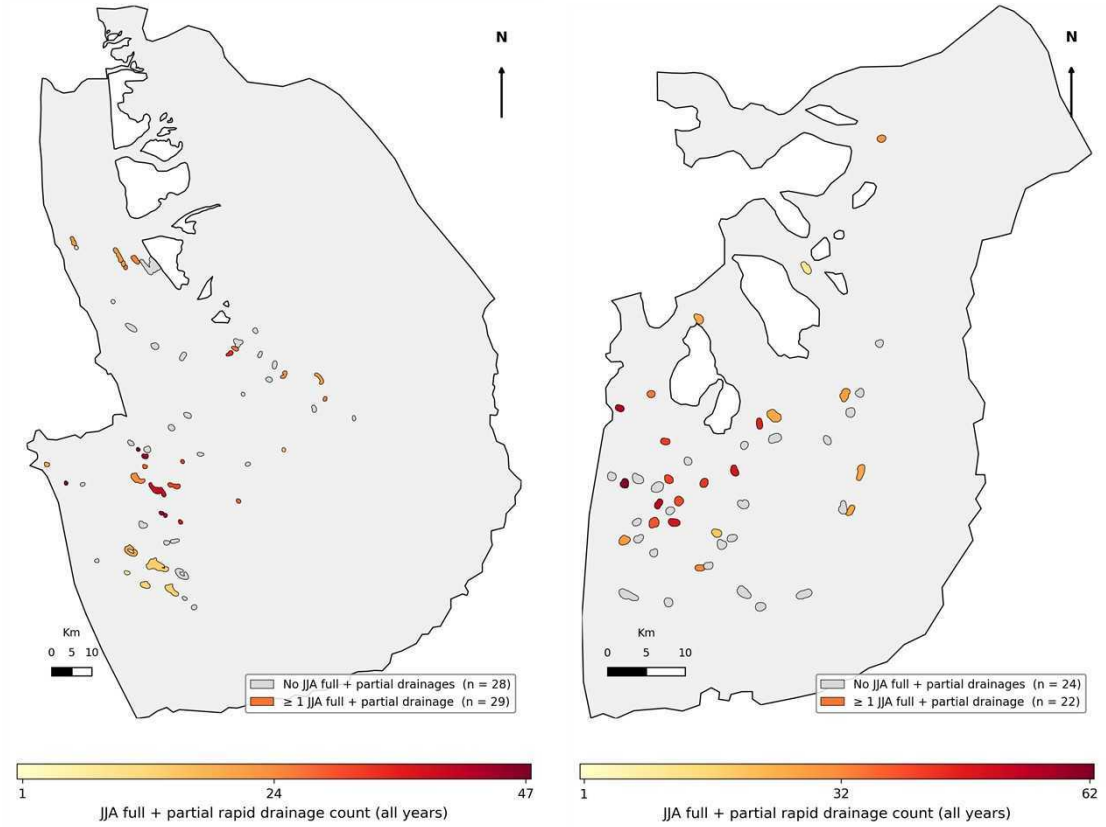

(a) Petermann (b) Ostenfeld

Figure 16. Persistent lakes colored by the number of drainage events recorded over 2014–2025, shown for (a) Petermann and (b) Ostenfeld. Lake counts include full and partial drainage, where a full drainage represents more than 80% volume loss and partial drainage represents between 40% and 80% volume loss.

5.10 Drainage events

Drainage events were detected using the algorithm of Section 4.6.6.

5.10.1 Annual event counts and volumes

A total of 1,744 drainage events were detected across both AOIs over 2014–2025 (Ostenfeld: 396 full + 440 partial = 836; Petermann: 392 full + 516 partial = 908). Annual full-drainage counts at Petermann range from a minimum of 10 (2017) to a maximum of 69 (2024), with 35, 41, 26, 10, 23, 21, 40, 15, 38, 49, 69, and 25 events for years 2014 through 2025 respectively. Aggregate annual drainage volume at Petermann, integrated over all detected events, ranges from 2.5 Mm^3 (2017) to 34.5 Mm^3 (2024), with the year-by-year sequence 18.6, 14.6, 19.0, 2.5, 5.7, 9.7, 26.8, 11.5, 16.4, 21.3, 34.5, and 8.2 Mm^3. At Ostenfeld the corresponding aggregate volumes are smaller (2017:

3.0 Mm^3; 2022: 10.3 Mm^3, the Ostenfeld peak; 2024: 10.1 Mm^3). Per-AOI annual drainage event counts (full plus partial) and DOY-resolved drainage volumes are shown in Fig. 17 and Fig. 18; annual counts and aggregate volumes per AOI are shown in Table 17.

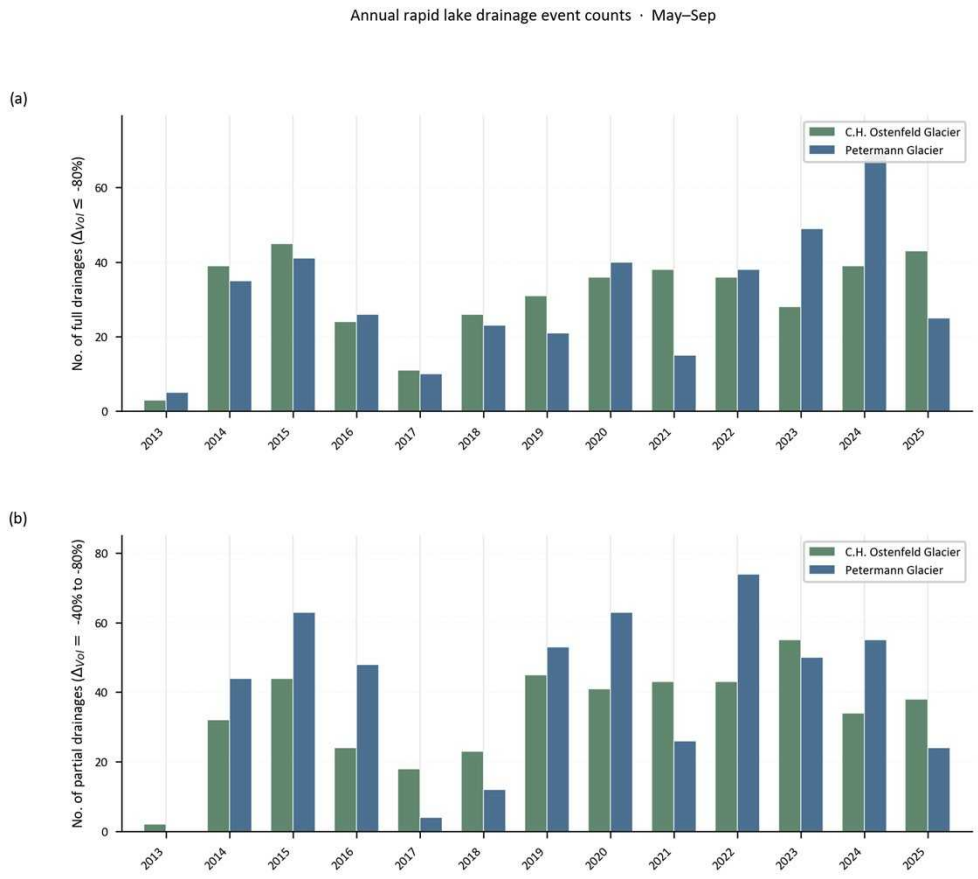

Figure 17. Count of full (a) and partial (b) rapid supraglacial lake drainage events for Ostenfeld (green) and Petermann (blue) per May-September melt seasons between 2014 and 2025. Full drainages are defined as ≥ 80% decrease in volume between observations. Partial drainages are defined as between 40%–80% decrease in volume between observations.

5.10.2 Petermann 2024 area-vs-drainage decoupling

Petermann 2024 had a JJA combined-maximum area of only 165 km^2 (a low-melt year, ×1.47 the algorithm-selected baseline) but produced the highest aggregate drainage volume of the entire record (34.5 Mm^3), the highest event count (124 total events), and the highest full-drainage count (69) at either AOI. A weaker but related decoupling occurred in 2020, where Petermann combined-maximum area was 177 km^2 (near baseline) but aggregate drainage volume was 26.8 Mm^3, the third-highest of the record. Both 2020 and 2024 follow immediately after a high-melt peak year (2019 and 2023 respectively). The largest individual drainage in the record is at Petermann lake P004, 2023-08-29 to 2023-09-04, with a single-event volume loss of 1.06 Mm^3. The 2020 and 2024 decoupling is discussed further in Section 6.7.

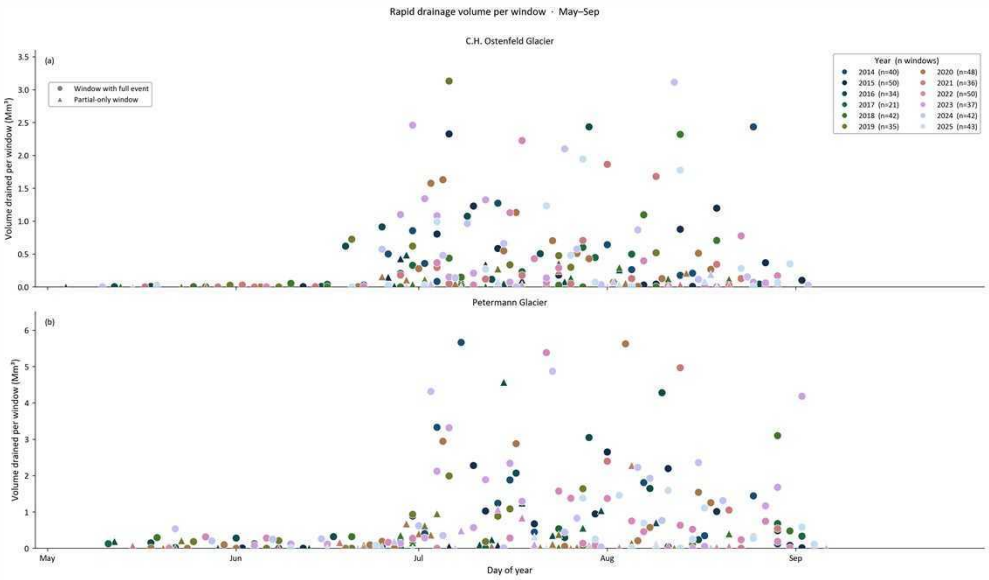

Figure 18. All windows by drainage volume and day of year for Ostenfeld (a), and Petermann (b). Windows with rapid drainages (circles) and windows with only partial drainages (triangles) are colored by according to year. Full drainages are defined as ≥ 80% decrease in volume between observations. Partial drainages are defined as between 40%–80% decrease in volume between observations. Windows where drained volume = 0 are not shown. Count of plotted windows per year is given alongside year color in legend. The volume unit is millions of cubic meters (Mm^3).

Table 17. Annual drainage-event counts and aggregate event volume per AOI, 2014–2025, for Ostenfeld (Ost) and Petermann (Ptm). *Full* drainages lose ≥ 80 % of basin volume; *Partial* drainages 40 to 80 %. *Vol.* is the per-year sum of event volume losses (Mm^3 (million m^3)). Ptm 2024 is the single highest year of the record on every drainage axis (events, full count, aggregate volume) despite a near-baseline combined-area year, the area-vs-drainage decoupling discussed in Section 5.10.2

	Ost				Ptm			
Year	Events	Full	Partial	Vol. (Mm^3)	Events	Full	Partial	Vol. (Mm^3)
2014	71	39	32	7.6	79	35	44	18.6
2015	89	45	44	9.0	104	41	63	14.6
2016	48	24	24	6.4	74	26	48	19.0
2017	29	11	18	3.0	14	10	4	2.5
2018	49	26	23	5.9	35	23	12	5.7
2019	76	31	45	6.8	74	21	53	9.7
2020	77	36	41	8.4	103	40	63	26.8
2021	81	38	43	6.1	41	15	26	11.5
2022	79	36	43	**10.3**	112	38	74	16.4
2023	83	28	55	8.1	99	49	50	21.3
2024	73	39	34	10.1	**124**	**69**	55	**34.5**
2025	81	43	38	7.8	49	25	24	8.2
Total	836	396	440	89.4	908	392	516	188.8

5.10.3 Seasonal timing of drainage

Drainage events span late June to early-September, with median day-of-year (DOY) in mid-July to early August. Mann-Kendall trend tests on five timing metrics per AOI (first-event DOY, first full-event DOY, median DOY, volume-weighted median DOY, and 90th-percentile DOY) over 2014–2025 return no significant trends across all ten tests (all $p > 0.13$). The strongest non-significant directional signals are Petermann median DOY trending later ($\tau = +0.32$, $p = 0.16$) and Ostenfeld 90th-percentile DOY trending later ($\tau = +0.35$, $p = 0.13$). First-event DOY is essentially flat at both AOIs ($\tau \approx 0.0$–0.05). Hamed-Rao corrected p-values match the standard p-values to within rounding for nine of ten tests, confirming that no autocorrelation caveat is required. The absence of an early-onset trend suggests that the drainage season has not shifted significantly in either direction. The Petermann median trending later is consistent with the slush-dominated melt regime delaying lake formation into late summer. The timing distributions are interpreted in Section 6.7.

5.11 Summary of main results

Slush is the dominant melt feature by combined area at both glaciers in every year of the record. The median slush-to-lake area ratio is 8.8 at Ostenfeld and 4.9 at Petermann. Neither site approaches parity between the two classes in any single year. Three independent lake-maximum measures at Petermann (area, elevation, and volume) each show a positive directional shift with Pettitt change points concentrated in the 2017–2020 window, the strongest cross-variable signal in the dataset. Both glaciers reached their highest melt extent in 2023. At Petermann the combined-maximum area reached 1495 km^2 (×13.3 the algorithm-selected baseline) and at Ostenfeld 474 km^2 (×4.9). In 2024, Petermann produced the highest aggregate drainage volume and full-event count of the record (34.5 Mm^3 and 69 full events) despite a near-baseline combined area of 165 km^2. The same decoupling between surface melt extent and drainage delivery recurred at smaller magnitude in 2020, the year after the previous melt peak.

6 Discussion

6.1 Overview

The chapter is organised around the four aims set out in Section 1.1. The methodology applied in this work is adapted from established sources, and the rationale for the major modifications is provided in Section 6.2. The statistical framing is also given there because no Mann-Kendall or Pettitt test reaches $p < 0.05$ at $n = 12$, so the surface-melt signals reported throughout are interpreted from effect sizes and the agreement of independent measures rather than from formal significance.

The overarching interpretive thread is the contrast in climate sensitivity between the two glaciers. The single-day summer maximum 2 m air temperature explains $R^2 = 0.85$ of Petermann combined-maximum area but only 0.25 of the same response at Ostenfeld, placing the two sites in separate forcing regimes despite lying only ~ 200 km apart (Section 6.3). Slush is the dominant temporary surface store at both glaciers (Section 6.4). The strongest multi-variable signal in the trend dataset is a 2017–2020 period

of interest at Petermann, contemporaneous with documented dynamic change at the grounding zone (Section 6.5). 2023 is the largest melt year of the record at both glaciers (Section 6.6), and 2024 produced the highest aggregate drainage volume at Petermann despite a near-baseline melt area (Section 6.7). Limitations and follow-on work are summarised in Section 6.8, and the four aims are revisited in Section 7.

6.2 Methodology support

Several modifications were made to apply the classifier, which was developed for Antarctic ice shelves (Dell et al., 2022), to the grounded-ice setting of northern Greenland. Likewise, merging the classifier and lake volume retrieval (Moussavi et al., 2020; Pope et al., 2016) with drainage event detection required further modifications. This section provides justification for processing-level changes to cloud masking, shadow handling, and mosaic construction (Section 6.2.1), and classification level changes to the training data generation (Section 6.2.2). Finally, Section 6.2.3 establishes the support for the statistical tests carried out by the present work.

6.2.1 Preprocessing

Cloud, rock, and topographic shadows on ice are a significant source of false-positive water classifications in automated optical SGL and slush mapping (Moussavi et al., 2020; Dell et al., 2024; Tuckett et al., 2025; Mahagaonkar et al., 2024). The Dell et al. (2022) random-forest method was developed for ice shelves, where low elevation and relatively smooth surface topography mean that glacial terrain shadows are neither prominent nor spatially persistent across a study period. On the grounded ice of Petermann and Ostenfeld, terrain shadows are a persistent source of classification error because surface undulations cast shadows at the same locations under similar solar angles across years. The slope mask introduced in Section 4.3.1, which removes pixels with slope $> 15\,\%$ from the training data, controls this error source without meaningful loss of true slush or lake pixels since both are flow-state features strongly constrained by low-gradient topography.

Temporal resolution in similar scale, automated random-forest studies ranges from 5 days (Glen et al., 2025b), to 15 days (Dell et al., 2022). Here, increased temporal resolution is required for high confidence rapid lake drainage detection, as noted by Fitzpatrick et al. (2014) and supported by *in situ* observations demonstrating that rapid drainage occurs on the scale of hours (Chudley et al., 2019). The adaptions listed and justified below were made to the preprocessing workflow to increase the area available for mosaiking and allow for the 2-day resolution achieved here.

Cloud masking: Landsat surface-reflectance products can be unreliable over high-albedo snow and ice, particularly where aerosol retrieval fails (Pons et al., 2025; USGS, 2024), and many glacial remote sensing and supraglacial-lake mapping studies instead use uncorrected Level 1 top-of-atmosphere reflectance products (e.g., Pope et al., 2016; Moussavi et al., 2020; Tuckett et al., 2025). A consequence is that the QA-band cloud flags underperform relative to lower-albedo land surfaces, and cirrus cloud in particular can be confused with ice reflectance. The $B9 < 0.008$ cirrus threshold applied in Section 4.4.1 addresses this gap and is based on the strict cirrus-band correction from Jiang et al. (2024).

Shadow projection: The cloud shadow masking in similar studies is accomplished with

multiband thresholds (e.g., Moussavi et al., 2020; Mahagaonkar et al., 2024) and large buffers around detected clouds (e.g., Dell et al., 2024). Here, cloud-shadow masking is achieved with a non-standard shadow vectors projection function. Standard cloud shadow projection stamps the cloud footprint at discrete intervals along the solar-azimuth vector at distances approximating a maximum cloud height parameter. In development testing this stamp-based implementation required higher per-scene compute cost and per-scene tuning of the maximum-height parameter than the fixed-stretch alternative. The fixed 8 km shadow stretch developed here (Section 4.4.1) has uniform compute cost across scenes and masks the shadows of detected clouds without per-scene tuning.

Mosaiking: The choice of medoid mosaics over quality mosaics (which select the highest pixel value per cell) follows from the preference for contamination reduction. Quality mosaics are used in the source method (Dell et al., 2024, 2022). However cloud-shadow pixels express anomalously high $NDWI_{(ice)}$ values that a maximum-value selector would preferentially retain. The shorter compositing window used here increases sensitivity to transient contamination and makes the median-proximity selection of the medoid preferable.

6.2.2 Classification and analysis

The addition of $NDWI_{(ice)}$ as an input band to the k-means clustering stage (Section 4.3.2) was motivated by the observation that clusters defined on reflectance bands alone did not cleanly separate the slush class in the training scenes. Slush clusters were characterized by lower reflectance here than reported in Antarctic studies (Dell et al., 2022, 2024). The disparity can potentially be attributed to prevalence of ice algae in the study area and the role of topographic factors (e.g., slope, aspect, elevation) on snow crystal reflectance (Saydi and Ding, 2020). It is also consistent with Greenland slush-line studies in which the slush signal transitions from uniform to heterogeneous mix of snow, slush, streams, and exposed ice along a wider spectrum than in Antarctic mapping (Greuell and Knap, 2000; Machguth et al., 2023). Furthermore, the $NDWI_{(ice)}$ modification is corroborated by work published during the course of this project from Glen et al. (2025a) who adopt $NDWI_{(ice)}$ as a cluster input in their nine-year inventory.

6.2.3 Statistical framing

The statistical tests used here (lag-1, anomaly analysis, analog pairs and recovery rate) are implemented as process-diagnostic comparisons rather than as stand-alone proof of trend given the twelve-year annual record. The anomaly analysis gives a reproducible baseline for comparing melt-area, elevation, and volume anomalies across metrics. This is following remote-sensing stability work in which deviations from a local reference state identify unusually large responses (White et al., 2020). Analog pairs similarly test climate-forcing, comparing years with similar ERA5 temperature and shortwave conditions to isolate melt-response differences not explained by external forcing. This is consistent with climate-analog approaches (Yegorova et al., 2025; Richardson et al., 2024). The lag-1 residual correlation is interpreted as a memory or preconditioning indicator rather than as raw series autocorrelation. The basis for this test comes from critical-slowing and resilience studies where increased memory and slower recovery indicate reduced system responsiveness (Boers and Rypdal, 2021; Boers, 2018), though the application here is more cautious because $n = 12$ and firn state is inferred from the surface record rather than measured. The recovery-rate tests quantify how rapidly

melt metrics rebound from low to high years and how much of the rebound remains after climate correction, adapting established recovery-rate and resilience metrics to the glacier surface-melt context (Veraart et al., 2012; Smith and Boers, 2023).

The anomaly analysis (Section 4.6.3) is supported by baseline sensitivity tests outlined in Section 5.5. Sensitivity of reported anomalies to baseline window choice is given in Fig. 7 and Table 9, and the Petermann 2023 fold-anomaly is the most baseline-sensitive result in the dataset (×3.1 to ×13.3 across baseline definitions, Table 9). The algorithm-selected baseline is retained as the primary reporting basis because the selection criteria (low coefficient of variation, minimum coverage, exclusion of extreme years) are reproducible and physically motivated.

Additionally, it should be noted that none of the Mann-Kendall or Pettitt tests reach $p < 0.05$ at $n = 12$ (Section 5.2.1, Table 6, Table 7). Hence, many of the arguments here rely on effect sizes, the agreement of independent measures, and the physical consistency rather than on formal significance. The record is short, the two glaciers behave differently, and several of the strongest signals appear at Petermann alone. These features determine both what can be claimed and what is left to later work.

6.3 Peak-temperature forcing and the contrast between the two glaciers

The regressions in Section 5.6 (Eq. 2) identify the daily maximum, not the seasonal mean, as the temperature variable that best tracks melt. At Petermann, JJA maximum 2 m air temperature explains $R^2 = 0.85$ of combined-maximum area and the same fraction of slush-maximum area, falling to $R^2 = 0.69$ for lake-maximum area (Table 13, Fig. 19). The seasonal-mean temperature explains almost none of the same variance ($R^2 = 0.04$ for combined-maximum area), and downwelling shortwave is weak at both glaciers (Fig. 20). A control by peak temperature rather than accumulated warmth fits the behavior of slush, which the Greenland literature reports as the most melt-sensitive surface class. Glen et al. (2025b) record a slush area roughly 47 times larger in a warm summer than in the preceding cool one. Daily slush-limit mapping in western Greenland likewise shows that the slush limit can rise quickly early in the melt season before plateauing (Machguth et al., 2023; Greuell and Knap, 2000). Slush is therefore characterized by quick response to warming, which supports the single warmest day of the season as a strong predictor for slush area, as observed here. However, Machguth et al. (2023) infer that enough melt energy was available to raise the slush limit by a further ~ 300 m, but the limit stalled at the upper margin of near-surface ice slabs, indicating an additional firn state control on slush to explain climate residual slush response.

Ostenfeld is the warmer of the two sites, with JJA maximum temperatures between 3.1 and 7.7 °C against 0.7 and 4.6 °C at Petermann (Fig. 9). Yet, its melt area responds weakly and noisily to that forcing ($R^2 = 0.25$ for combined-maximum area, Fig. 19). This is explained when incorporating mean metrics as a baseline for maxima. Petermann has a colder mean, with JJA mean temperature between −4.7 and −1.8 °C across the record, so melt there can be interpreted as episodic and tied to short warm excursions that the maximum captures and the mean does not.

Ostenfeld is warmer than Petermann and its slush sits closer to the 1500 m AOI elevation cap, so the elevation series saturates against the study-area ceiling. Part of its weak and

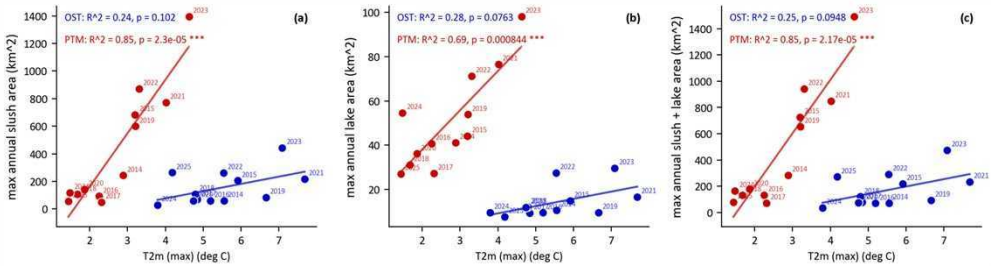

Figure 19. Ostenfeld + Petermann scatter of JJA maximum 2 m temperature against JJA maximum melt (a) area for slush, lake, and combined classes. Petermann (red) traces a tight steep relationship, while Ostenfeld (blue) is markedly flatter and noisier on the same axes.

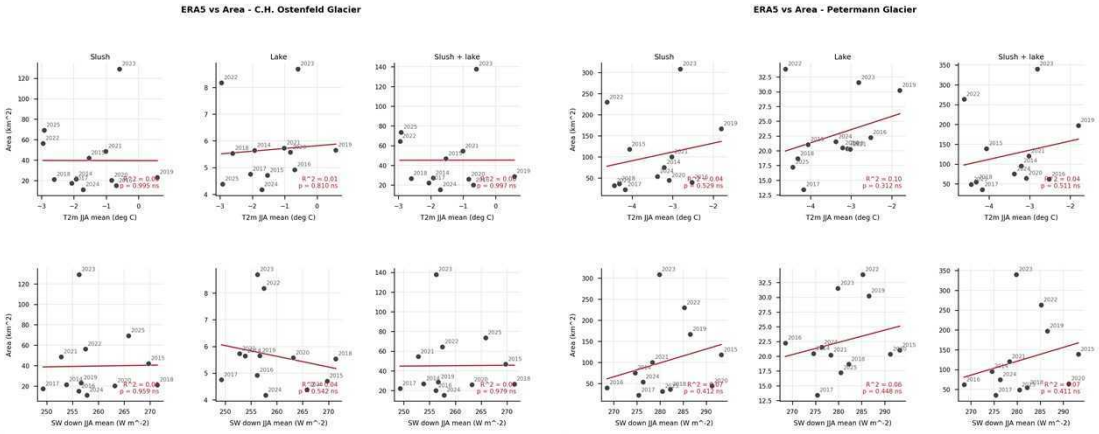

Figure 20. Annual melt area metrics at Ostenfeld (left) and Petermann (right) against ERA5-Land JJA mean 2 m temperature (top row) and JJA mean downwelling shortwave radiation (bottom row).

even negative response is therefore likely an artifact of a too-restrictive AOI boundary rather than a physical signal. The Ostenfeld slush-maximum series spans only 1471 to 1501 m across all twelve years, sitting within ± 1.5 % of the boundary in every year, and the resulting combined-maximum elevation anomalies are bounded between -1.2 % and 0.8 %, which suggests little beyond the fact that the AOI ceiling is too low. The negative correlation between Ostenfeld mean temperature and slush-maximum elevation ($r = -0.79$, Section 5.5.2) should be interpreted the same way. A cold-mean but warm-peak year pushes the slush limit against the ceiling, compressing the upper end of the elevation response and producing an apparent inverse signal. The 1500 m study-area boundary is a significant limitation for slush elevation analysis at Ostenfeld, and a wider AOI would be the first step in any follow-on work at that site.

6.4 Slush as the dominant surface meltwater store

Slush carries most of the combined melt area at both glaciers across the record. The median ratio of slush-maximum to lake-maximum area is 8.8 at Ostenfeld and 4.9 at Petermann. Neither glacier reaches parity and at Ostenfeld the ratio reaches 34.2 in 2025 (Section 5.3, Fig. 21, 15, 14). The slush term also carries the anomaly more strongly. In every year above the 50 % combined-area anomaly threshold the slush component is two to five times the lake component (Fig. 8 panels (a)-(h)), and the 2025 Ostenfeld recovery is almost entirely slush, with slush-maximum area at 202 % of baseline while lake-maximum area fell to -26 % (Section 5.5.1). Slush dominance by area agrees with the wider Greenland literature, where mapped slush is four to nine times the combined area

of lakes and streams (Glen et al., 2025a), and confirms a pattern established for the firn percolation zone of the southwest GrIS(Glen et al., 2025b). Recent field measurements show meltwater can move laterally through slush over ice slabs at 1.3 to 15.1 m h^{-1}, and the visible slush limit may lie below the true runoff limit where subsurface flow continues beyond what optical imagery can detect (Clerx et al., 2022).

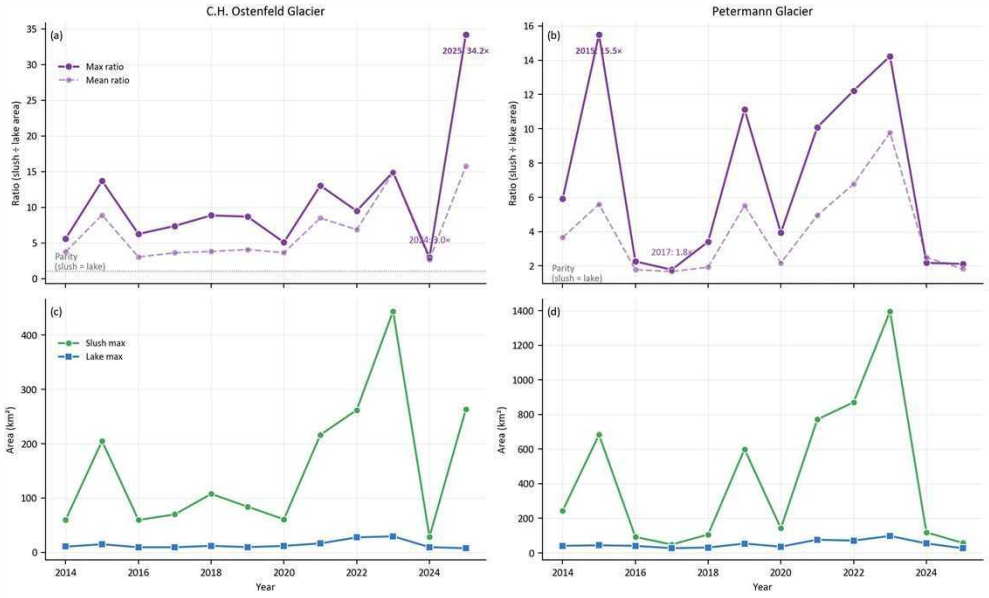

Figure 21. (a, b) Annual time series of JJA slush:lake area ratio showing both mean (dashed line) and maximum (solid line) for (a) C.H. Ostenfeld and (b) Petermann. (c, d) Annual maximum lake (blue line) and slush (green line) area (km^2) for (c) Ostenfeld, and (d) Petermann. High and low years are noted in the ratio panels with their magnitudes. Low years are 2024 (3x) for Ostenfeld and 2017 (1.8x) for Petermann. High years are 2025 (34.2x) for Ostenfeld and 2015 (15.5x) for Petermann.

Slush area is highly variable across years and between study areas (Fig. 3, 21, 9). Ostenfeld stays slush-dominated regardless of the melt intensity, while Petermann varies between near 1:1 in cool years, with a ratio of 1.8 in 2017, and clear slush dominance in warm years, with a maximum ratio of 15.5 in 2015. Dell et al. (2024) show that firn pore space exerts a first-order control on surface meltwater formation. The Greenland evidence additionally supports antecedent snowpack, firn permeability, and low-permeability ice slabs in the percolation zone (MacFerrin et al., 2019; Brils et al., 2024). Ostenfeld's persistent slush dominance suggests that meltwater is absorbed as slush preferentially to collecting in lakes, indicating its firn state as distinct from Petermann's. On Petermann, the larger year-to-year variation suggest a less stable firn and potential ice-slab system, where similar melt inputs can alternately be stored as slush, pond as lakes, or route downstream. Firn state is not quantified here, so these interpretations are given as inference from the surface record rather than a direct test.

At the visible runoff limit in southwest Greenland, Tedstone et al. (2025) found that ~ 84 % of available melt refroze as superimposed ice above ice slabs, showing that low-permeability firn can both promote runoff and still retain a large fraction of melt locally. For Petermann and Ostenfeld, this means the dominant temporary surface store is unlikely to be deep ponded water alone. Whether mapped slush ultimately refreezes, remains stored, ponds, or routes downstream depends on firn and slab state as much as on the surface area classified as meltwater (Vandecrux et al., 2020; Tedstone and Machguth, 2022).

The melt persistency heatmaps show that slush is less spatially confined than lakes, with a significantly larger area and lower per-pixel scores indicating a reduced likelihood to form in the same locations year to year, while lakes are strongly confined to basins where core pixels recur every year (Fig. 11). This illustrates the relative control of topography on the distribution of each feature. Additionally, the southwestern spatial bias of persistent melt (Fig. 11) suggests slope aspect exerts control on melt distribution across both study areas. In high-melt years slush expands across the western sectors (Petermann 2019, 2022, and 2023, and Ostenfeld 2022, 2023, and 2025) yet is still underrepresented in the northeast portions as demonstrated by the annual maximum melt blocks and mosaics (Fig. 13, Fig. 12, Fig. 15, and Fig.14).

6.5 The post-2017 Petermann lake regime

The strongest multi-variable signal in the trend analysis is at Petermann, where lake-maximum area, elevation, and volume share the same sign and place their Pettitt change points inside the 2017 to 2020 window (Fig. 22). The change point in lake-maximum elevation after 2017 is the strongest elevation signal in the dataset (Section 5.4). No individual test reaches significance at $n = 12$, so this is reported as a period of interest defined by the agreement of three physically related but methodologically separate measures, and not as an established trend. The shift corresponds to the climatic warm peaks of the same period (Fig. 9), though the cool 2024 and 2025 seasons argue against monotonic warming. More notably, the 2017 shift aligns with the onset of both significant retreat and thinning at the grounding zone (Section 3.2).

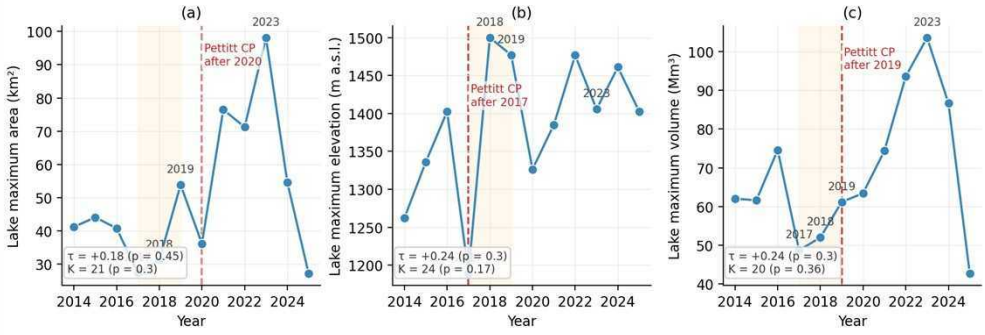

Figure 22. Petermann lake-maxima behavior and proposed shift indicators. Shows JJA lake-maximum area (a), elevation (b), and volume (c) at Petermann with Pettitt change-point markers, Mann-Kendall τ and Pettitt K in bottom-left of each panel. All three lake maxima variables show positive τ and change points concentrated after 2017. No individual test reaches $p < 0.05$ at $n = 12$, but the cross-variable and directional agreement is presented as supporting a shift in lake dynamics.

The lake-maximum elevation anomaly series is dampened by the 2017–2019 baseline window choice. The baseline value for 2018 is 1499.9 m, which is directly against the 1500 m AOI ceiling. While this value is counter-weighted by 2017, the lowest Petermann elevation in the series, the positive anomaly is nevertheless negatively biased compared to volume and area. Excluding 2018 from the baseline would produce wider anomaly spreads for the post-baseline period, and that sensitivity is documented in the appendix. The Pettitt change point after 2017 (Section 5.4) therefore carries more weight as evidence of the elevation shift than do the percent-anomaly magnitudes in panels (m)-(r) of Fig. 8.

The 2017 shift corresponds with a period of change in Petermann glacial dynamics observed in the literature (Ciracì et al., 2023; Li et al., 2021; Millan et al., 2022; Washam et al., 2020; Prakash et al., 2025) and summarized in Section 3.2. The documented changes over this period include the 2017 calving event, central grounding-zone retreat onto a retrograde bed, the ~15% velocity increase across 2015–2018, and the approximate doubling of channel subglacial discharge between 2001 and 2022. A direct link between this dynamic adjustment and the increase in lake-maximum area, elevation, and volume is not tested here. However, the temporal coincidence supports the validity of the change point in lake behavior identified by this study.

Two physical mechanisms could carry the 2017–2020 surface signal. A firn-state pathway through wetting, aquifer charging, or ice-slab growth would alter how meltwater is stored and partitioned at the surface (Forster et al., 2014; Miège et al., 2016; MacFerrin et al., 2019). A dynamic pathway, in which increased velocity and thinning near the grounding zone concentrate surface change at lower elevations and transmit up-glacier with reduced magnitude through diffusive thinning processes, would redistribute the elevation profile and shift the basins capable of holding lakes (Schoof, 2007; Schoof and Hewitt, 2013; Joughin et al., 2012; Pritchard et al., 2009). The two pathways are not mutually exclusive and either or both could operate. Each is inferred from the surface record rather than measured here. Satellite-altimetry hypsometry and direct firn measurements from radar or cores would adjudicate between them, or confirm that both contribute.

6.6 The 2023 melt anomaly

Of the 132 within-AOI year pairs screened across the two glaciers, 2023 reads as anomalously wet relative to its forcing in four of the five most-flagged pairs and in eight of the top fifteen (Fig. 23, Table 14). 2023 is the largest melt year of the record at both glaciers, which sets it apart from the otherwise glacier-specific signals discussed above (See Figs. 15, 14). Petermann combined-maximum area reached 1495 km^2, 1227 % of the algorithm-selected baseline (×13.3) and the single largest annual area at either glacier, while Ostenfeld reached a record high the same year at 474 km^2 (×4.85),(Table 5, Table 10, Fig. 8 panels (a - h)).

Slush carries essentially all of the anomaly at both sites (Fig. 8, panels (c), (d), (g), (h)). The Petermann slush-maximum anomaly of 1595 % (×17.0) dwarfs the lake-maximum anomaly of 196 % (×2.96), and Ostenfeld shows a split with smaller magnitude (409 % slush against 185 % lake). 2023 was also the warmest year of the Petermann record, at a JJA maximum air temperature of 4.6 °C against a record range of 0.7 to 4.6 °C (Fig. 9), so the peak-temperature coupling referred to in Section 6.3 (R^2 = 0.85 for Petermann combined-maximum area) already accounts for much of the response. The analog-pair signal remains once that coupling is removed, however.

The 2023 anomaly is dominated by slush rather than ponded lake water. Petermann combined-maximum area is +1227% of baseline while Petermann lake-maximum volume is +77%. The contrast indicates a slush-driven area expansion rather than a pond-volume expansion.

The 2023 combined-mean elevation signal at Petermann is near twice its baseline (106 % in 2023, ×2.06), with slush-mean elevation at 894 m a.s.l. (Table 12, Fig. 8, panels (m)–(r)). Slush footprint and elevation limit increase in the warmest record year is reported

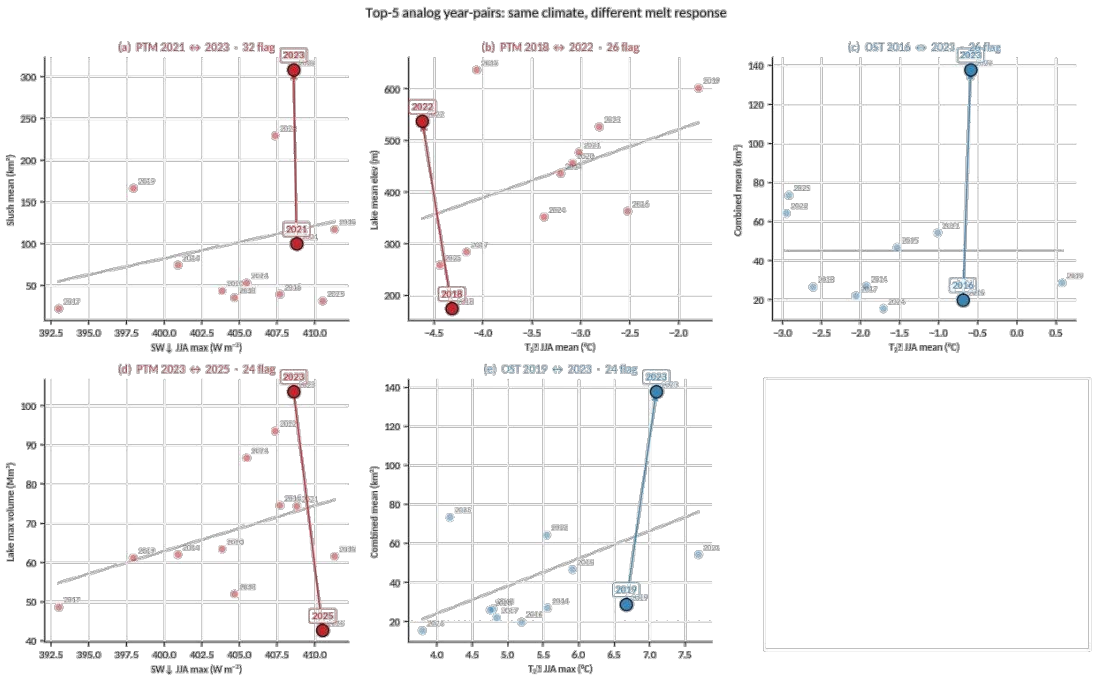

Figure 23. Top five most-flagged analog pairs across the 56 (predictor, response) combinations screened per AOI. Each panel plots the climate predictor (x-axis) against the melt response (y-axis), with arrows connecting paired years. 2023 appears in four of the five pairs shown.

elsewhere in Greenland (Machguth et al., 2023; Fitzpatrick et al., 2014; Poinar et al., 2015).

The Petermann magnitude is the most baseline-sensitive number in the dataset, from ×3.1 under a full-record-mean baseline to ×13.3 under the algorithm-selected baseline (Table 9). The standing of 2023 as the record anomaly is consistent across every baseline, but the absolute fold-change should be interpreted with that range in view.

6.7 Drainage volume and the routing of surface melt

Lake persistency on the Petermann floating ice tongue covers a wider area, and is generally lower scoring compared to the lake persistency on the grounded portion of the study area (Fig. 24, panel (b)). The floating ice tongue is not in contact with the bed, which separates melt from topographic control and explains the both the large lake persistency coverage and low slush score diversity. Likewise, lateral steaks at regular intervals indicate the down fjord progression of transverse fractures with ice flow at ~ 1090 to 1100 m yr^{-1} (Hill et al., 2017, 2018a). The highest lake scores on the Petermann tongue form in flow parallel lines, interpreted as surface water collecting in the full length fractures discussed in Section 6.5. The persistence of lakes within tongue fractures, suggests vertical drainage from the tongue is an additional source of surface runoff to the fjord, besides subglacial discharge from the grounding line. The distribution of persistent melt water on the tongue (Fig. 24), and the drainage counts of persistent lakes (Fig 16) presented here provide a spatial control on the location of vertical drainage.

The drainage detection algorithm resolved 1,744 rapid drainage events over the record, 908 at Petermann and 836 at Ostenfeld (Table 17). Petermann exhibits greater variation than Ostenfeld. Petermann full-drainage (> 80% volume loss) count runs from 10 in the

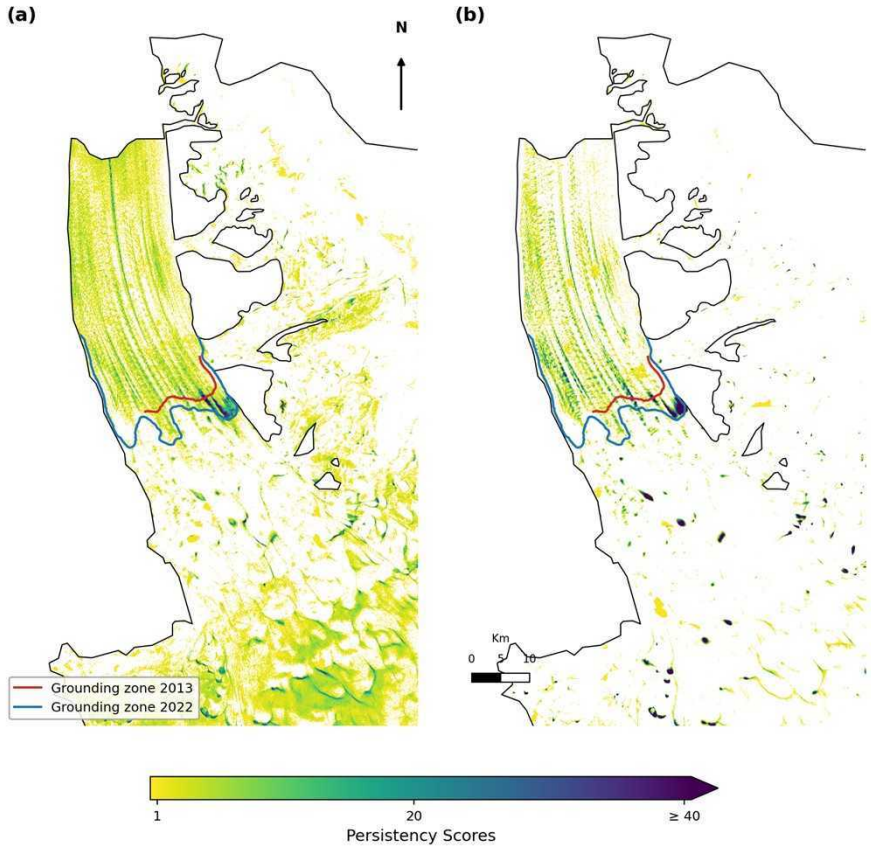

Figure 24. Petermann ice-tongue persistency heatmap for slush (a) and lakes (b), with grounding-zone locations from 2013 (red line) and 2022 (blue line). Pixel value is the count of 2-day windows in 2014–2025 in which the pixel was classified as that class. Values are normalized to 40 and symbolized yellow (low) to purple (high). *(CRS: EPSG:3413, WGS 84 / NSIDC Sea Ice Polar Stereographic North)*

cool 2017 season to a record 69 in 2024, and its partial-drainage (40% – 80% volume loss) count peaks at 74 in 2022, while Ostenfeld stays within a narrower band across the record (Fig. 17) This is interpreted as a dual result of Petermann's larger area and the high variation in lake number on the flat surface of the ice tongue between years.

GZ proximate lakes are noted as prone to rapid drainage from tidal flexing (Trusel et al., 2022). However, no full or partial drainage was identified for the largest persistent lake in the study, which is positioned above the eastern end of the Petermann GZ (Fig. 24, Fig. 16). Barring accuracy assessment, this result should be interpreted as omission error arising from the lakes' proximity to the fjord wall. Two error pathways are possible. The first is fjord-wall shadowing or darkening of the water surface that leads to artificially low reflectance values. The second is bed-albedo proxy values contaminated with fjord-wall or shadowed-ice pixels that lead to artificially high volume estimates.

The separation between drainage volume and melt area in individual years is a notable result. Following the extreme 2023 melt response at Petermann, 2024 had a near-baseline combined-maximum area (×1.47) yet produced the largest aggregate drainage volume of the record (Fig. 25), the highest full-drainage count at either glacier (Section 5.10.2, Fig. 17), and the third-highest lake-maximum volume of the record (48 %, ×1.48) in a low-slush year (Table 11, Fig. 3). Both the aggregated-drained and static-maximum volume rankings indicate that 2024 is not comparative to record low years in terms of melt production. The large drained volume in 2024 from a near-record-low melt area is consistent with a more connected drainage network developed during three prior years of high melt.

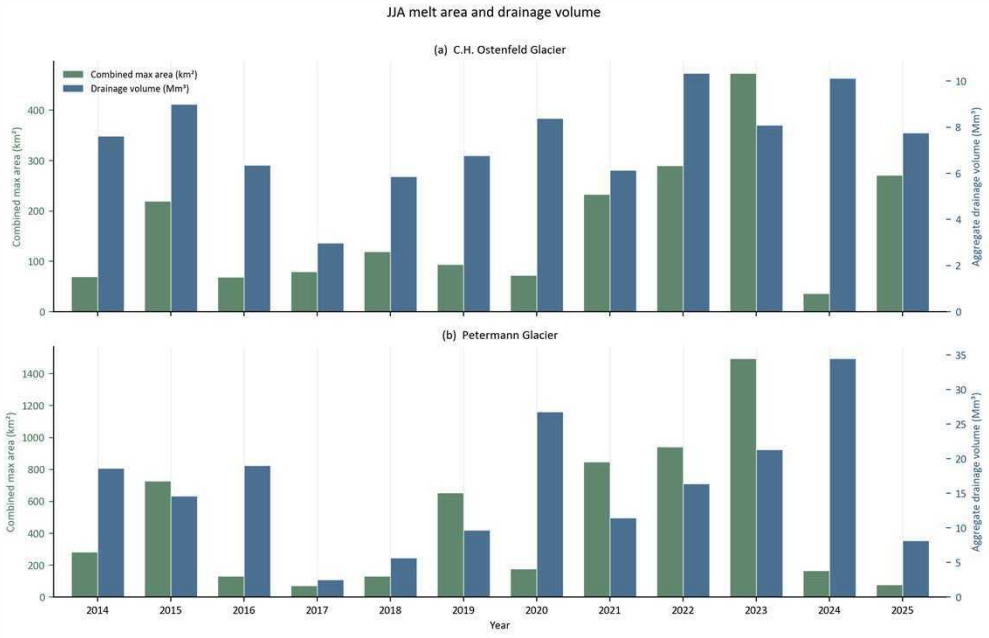

Figure 25. Annual JJA combined-maximum area (green, left axis km^2) and aggregated drainage volume (blue, right axis, Mm^3) for Ostenfeld (top) and Petermann (bottom). Figure shows years 2014–2025. Note 2019-2020, 2023-2024 drainage volumes relative to melt areas. Volume unit is millions of cubic meters.

The 2024 Ostenfeld combined-maximum area of 36.3 km^2 is half the next-lowest year of the record (Ostenfeld 2016, 69.2 km^2) and one-thirteenth of the Ostenfeld 2023 peak (473.5 km^2, Fig. 25). The Ostenfeld 2024 slush anomaly is the deepest single-year slush deficit in the record at either AOI. This pattern is consistent with the Ostenfeld area Pettitt

change point after 2020 reported in Section 5.2.1. Ostenfeld 2023 drainage volume dips slightly compared to consistent drainage maximum both directly preceding and following the 2023 area peak (Section 5.10.1), while Ostenfeld melt area collapses to the lowest observed area in 2024.

The 2024 decoupling is not isolated. Both glaciers in 2020 display the same dynamic, characterized by a near-baseline melt area year with a high drainage volume (Fig. 25). Both 2020 and 2024 immediately follow high-melt years, in 2019 and 2023. The area and volume separation is noted elsewhere without a slush area component. Fitzpatrick et al. (2014) show that many small lakes can occupy less than 2 % of a catchment while temporarily storing or releasing 7 to 13 % of discharge.

The per-window drainage volumes concentrate in mid-July to mid-August, and the two largest windows by drained volume of the Petermann record both fall in 2020 and 2024, reaching roughly 4 Mm^3 in early August 2020 and late July 2024 (Fig. 18). The drainage timing distribution envelope does not move between seasons, however. Mann-Kendall tests on the timing metrics return no significant trend at either glacier, with first-event timing essentially flat and only a weak tendency for the Petermann median to fall later in the season ($\tau = +0.32$, $p = 0.16$, Fig. 26).

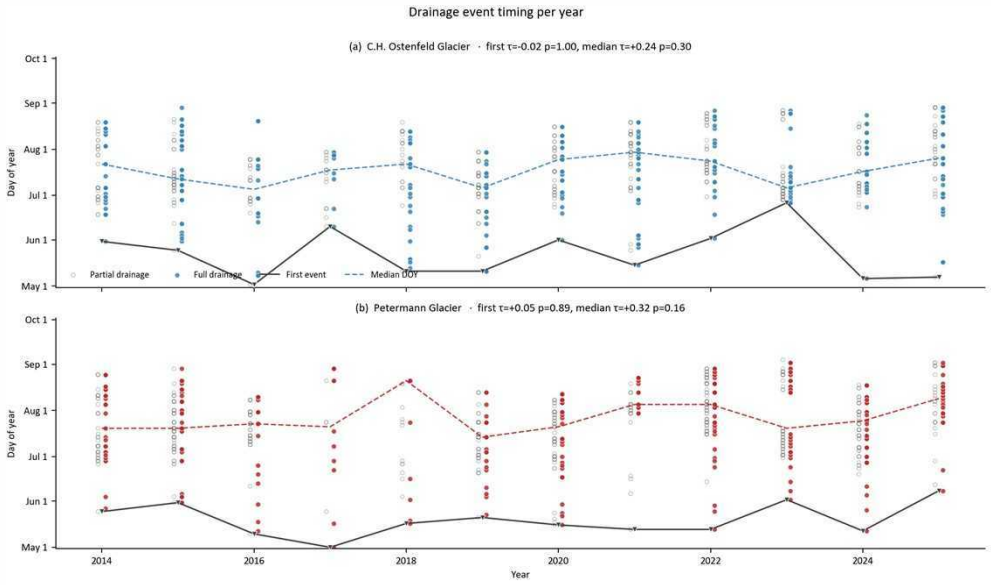

Figure 26. Annual drainage-event timing metrics for (a) Ostenfeld and (b) Petermann, 2014–2025. Full drainage events (Ostenfeld in blue dots, Petermann in red dots) and partial drainage events (grey circles) are plotted by drainage timing, with the x-axis showing the melt season (1 May to 1 October) and the y-axis showing study years. Metrics tracking the timing of the first drainage event per year (grey solid line) and the median drainage event per year (Ostenfeld in blue dashed line, Petermann in red dashed line) are overlaid as time series. Kendall τ and p values for first and median drainage timing are listed beside panel titles for each AOI.

A high-melt year can leave behind a changed set of basins, moulins, firn conditions, and drainage pathways that alter how the next year's melt input is stored and routed. Efficient drainage as a surface memory mechanism can account for 2020 and 2024 drainage behavior. A drainage network left more connected by the preceding high-melt season is supported by the persistent-lake inventory in that the basins which drain at the highest rates across the record are spatially clustered within the western melt sectors of both study areas rather than spread across the area of interest (Fig. 16). At Petermann the most frequently draining basins, with up to 21 rapid events over the record, sit in a

southwest cluster, and 29 of the 57 persistent lakes drain at least once. At Ostenfeld the draining lakes form a more spatially compact west-central group (22 of 46), with individual basins reaching 33 events (Fig. 16). This clustering is consistent with the coupled drainage reported elsewhere in Greenland, where stress transfer links neighboring lakes and a small number of lakes open a large share of the moulins (Christoffersen et al., 2018; Williamson et al., 2018).

The decoupling of volume from area also speaks to an assumption built into the subglacial-discharge literature. Discharge estimates and projections for Petermann and similar margins generally take essentially all modelled surface melt to reach the bed within the season it is produced (Section 2.2, Ciracì et al. 2023; Cai et al. 2017; Prakash et al. 2025).

The aggregate observed drainage volumes at Petermann can be set against modelled subglacial discharge for the same glacier to bound the contribution of rapid lake drainage to that assumption. The Mankoff et al. (2020) and Slater et al. (2022) estimates put Petermann mean JJA subglacial discharge at 877 $m^3\ s^{-1}$, which integrates to roughly 6970 Mm^3 over a 92-day JJA season (Table 1). The mean observed per-year drainage from persistent lakes at Petermann is 15.7 Mm^3, the 12-year aggregate is 188.8 Mm^3, and the 2024 record reached 34.5 Mm^3. Observed lake-drainage volumes therefore account for approximately 0.2 % to 0.5 % of one modelled JJA season at Petermann. Rapid lake drainage is a small fraction of the modelled total. The bulk of modelled subglacial discharge must reach the bed through supraglacial streams, moulins, and lateral flow through slush, which the present optical record does not resolve as delivery pathways. The assumption that essentially all modelled surface melt reaches the bed within the season it is produced is therefore neither confirmed nor refuted by the present surface-hydrology record.

6.8 Limitations and future work

The main limitation is the length of the record. At $n = 12$ the trend and change-point tests have low power, which is why effect sizes and the agreement of independent measures have been treated as primary throughout (Section 5.2.1). The 1500 m cap on the areas of interest saturates the Ostenfeld elevation series and limits what the elevation results can say at that glacier. Per-lake volumes carry a systematic uncertainty of roughly 15 % to 25 % from the depth-retrieval constants (Fig. 5), and the dominant classification error is the slush-to-other boundary (Fig. 4, Table 4), a known difficulty in optical mapping of slush (Dell et al., 2024). Footprint coverage varies between years, with Petermann 2017 and 2021 the weakest (Table 3). The main text reports observed values throughout, and the projected scaling with its sensitivity is given in the appendix. The firn state that several arguments here depend on is inferred from the surface record rather than measured. The recovery-rate cycle slopes at $n = 3$–4 years per cycle are descriptive comparisons rather than significance tests, and bootstrap confidence intervals are wide. Seven alternative trough-to-peak window combinations satisfy the candidate criteria per AOI, and sensitivity to cycle-boundary choice is documented in the appendix. The 40% and 80% drainage-event thresholds were not subject to sensitivity testing in the present work.

These limitations point to specific next steps. The convergence of the three Petermann lake-maximum measures could be tested against a null model to estimate how often three

independent measures would align by chance, which Section 5.4 does not address. A longer record, or a higher-resolution slush product from Sentinel-2 (Glen et al., 2025a), would raise the power of the trend tests and sharpen the slush results. Direct firn measurements from radar or cores would test the firn and ice-slab reading of the slush-to-lake partitioning. Coupling the measured drainage volumes to a subglacial-discharge or plume model would turn the routing question from a qualitative observation into a quantitative test (Prakash et al., 2025). The nested Petermann FVCOM framework of Prakash et al. (2022) provides a natural starting point for that step. Ice-velocity data would let the dynamic reading of the Petermann shift be separated from the climatic and hydrological readings, especially if paired with event-scale drainage detections like those resolved at 79°N Glacier by Neckel et al. (2020). A comparison across the wider sector, taking in Ryder and 79N, would set the two-glacier contrast found here in a regional context (Otto et al., 2022; Humbert et al., 2023).

7 Conclusions

This work characterized supraglacial lake and slush area, elevation, lake volume, and rapid lake-drainage events on Petermann and Ostenfeld glaciers across the 2014–2025 melt seasons. The present record is the first published surface-hydrology dataset for Ostenfeld Glacier (Section 3.3). The four aims set out in Section 1.1 are revisited below.

(i) Variability and structural shifts. Both glaciers are dominated by inter-annual variability over the twelve-year record rather than a monotonic trend, and no Mann-Kendall test reaches $p < 0.05$ at $n = 12$. The single multi-variable signal in the dataset is at Petermann, where lake-maximum area, elevation, and volume converge on a 2017-2020 period of interest contemporaneous with documented dynamic change at the grounding zone (Section 6.5). 2023 is the largest melt year of the record at both glaciers, with combined-maximum area reaching ×13.3 the algorithm-selected baseline at Petermann and ×4.9 at Ostenfeld (Section 6.6).

(ii) Rapid lake-drainage events. 1,754 drainage events were detected across both glaciers over the record (913 Petermann, 841 Ostenfeld). Petermann 2024 produced the highest aggregate drainage volume of the record (34.5 Mm^3) despite a near-baseline combined-melt area. The year-to-year decoupling of melt area from drainage delivery is discussed in Section 6.7. When set against modelled subglacial-discharge magnitudes for Petermann, the aggregate observed drainage from persistent lakes accounts for less than 1% of one modelled JJA season, indicating that lake-drainage events are a small fraction of the surface runoff routed to the bed.

(iii) Climate forcing. JJA single-day maximum 2 m air temperature explains $R^2 = 0.85$ of Petermann combined-maximum and slush-maximum area, the strongest statistical result in the dataset (Section 6.3). The seasonal-mean predictor explains almost none of the same variance, indicating that peak warm excursions rather than accumulated warmth drive the surface-melt response. Petermann remains below 0 °C in JJA mean across the entire record.

(iv) Inter-glacier asymmetry. The same temperature regression at Ostenfeld returns $R^2 = 0.25$. Ostenfeld is the warmer of the two glaciers in both JJA mean and JJA maximum, yet its melt area is less sensitive to that forcing. Part of this asymmetry is an AOI-ceiling artifact at 1500 m, and a second contribution comes from inter-glacier

differences in slush dominance (median slush-to-lake ratio 8.8 at Ostenfeld against 4.9 at Petermann, see Section 6.4). Pooling the two glaciers in a single regression washes out both signals.

Outlook. Two leads stand out for follow-on work. The Petermann 2017–2020 period of interest would benefit from satellite-altimetry hypsometry and direct firn observations that could adjudicate between dynamic and firn-state mechanisms. The routing-efficiency assumption underlying NGrIS subglacial-discharge estimates would benefit from coupling the present surface record to a process-based runoff or plume model. A regional comparison with Ryder and 79N would set the two-glacier contrast established here in a wider NGrIS context.

Acknowledgements

I am deeply grateful to my supervisors, Nina Kirchner and Abhay Prakash, for their guidance, patience, and critical feedback throughout the development of this thesis. I also thank the Master's programme in Polar Landscapes and Quaternary Climate and the Department of Physical Geography at Stockholm University for providing the academic setting in which this work was carried out. I also want to thank my classmates, and peers of the geospatial lab for support and company without which this project would have been more difficult.

I am grateful to Rebecca Dell and co-authors for the detailed supporting documentation for slush classification attached to their work, and to Rebecca Dell for advice during classifier development.

Additionally, this study relies on openly available Landsat 8 and Landsat 9 data, courtesy of the U.S. Geological Survey and contains modified Copernicus Climate Change Service information (ERA5-Land, Muñoz-Sabater et al. 2021); neither the European Commission nor ECMWF is responsible for any use that may be made of the information it contains. Classification and per-window mosaicking were carried out in the Google Earth Engine platform (Gorelick et al., 2017). I gratefully acknowledge the USGS and NASA Landsat programme, Google Earth Engine, ECMWF/Copernicus ERA5-Land, and the MEaSUREs Greenland data products used in the analysis. The post-processing and analysis workflow was built with open-source tools, especially Python, pandas, and GeoPandas.

Data and code availability

The supplementary data and code archive is available at `https://stockholmuniversity-my.sharepoint.com/:f:/g/personal/luur4790_win_su_se/IgA3_anPDYUISYQ4xAYoSRqMAbRP5bm3BWJrrhtWScZb9bE?e=Ufauje`. Classified rasters are hosted as Earth Engine assets and are accessible with an Earth Engine account at `https://code.earthengine.google.com/?asset=projects/vernal-signal-270100/assets/ClassifiedMosaics`. A complete inventory of scripts, CSV outputs, vector shapefiles, raster products, and Earth Engine collections is provided in Appendix D.

AI usage

Claude (Anthropic, model Claude Opus 4.7), accessed via Claude Code, was used for editing, batch updating and debugging code and provided inline comments for readability.

References

Alley K, Scambos T, Miller J, Long D, MacFerrin M. 2018. Quantifying vulnerability of Antarctic ice shelves to hydrofracture using microwave scattering properties. Remote Sensing of Environment 210:297–306. doi:10.1016/j.rse.2018.03.025.

Bamber JL, Siegert MJ, Griggs JA, Marshall SJ, Spada G. 2013. Paleofluvial Mega-Canyon Beneath the Central Greenland Ice Sheet. Science 341:997–999. doi:10.1126/science.1239794.

Banwell AF, MacAyeal DR, Sergienko OV. 2013. Breakup of the Larsen B Ice Shelf triggered by chain reaction drainage of supraglacial lakes. Geophysical Research Letters 40:5872–5876. doi:10.1002/2013GL057694. _eprint: https://onlinelibrary.wiley.com/doi/pdf/10.1002/2013GL057694.

Bell RE, Chu W, Kingslake J, Das I, Tedesco M, Tinto KJ, Zappa CJ, Frezzotti M, Boghosian A, Lee WS. 2017. Antarctic ice shelf potentially stabilized by export of meltwater in surface river. Nature 544:344–348. doi:10.1038/nature22048.

Benn DI, Warren CR, Mottram RH. 2007. Calving processes and the dynamics of calving glaciers. Earth-Science Reviews 82:143–179. doi:10.1016/j.earscirev.2007.02.002.

Boers N. 2018. Early-warning signals for Dansgaard-Oeschger events in a high-resolution ice core record. Nature Communications 9:2556. doi:10.1038/s41467-018-04881-7.

Boers N, Rypdal M. 2021. Critical slowing down suggests that the western Greenland Ice Sheet is close to a tipping point. Proceedings of the National Academy of Sciences 118:e2024192118. doi:10.1073/pnas.2024192118.

Bowling JS, McMillan M, Leeson AA, Livingstone SJ, Sole AJ, Ng FSL, Karlsson NB, Nienow P, Boxall K, Noël B, van den Broeke MR, Slater T, Maddalena J, Sandberg Sørensen L, Simonsen SB, Mouginot J, Millan R, Melling L, Taylor L, Humbert A. 2025. Outburst of a subglacial flood from the surface of the Greenland Ice Sheet. Nature Geoscience 18:740–746. doi:10.1038/s41561-025-01746-9.

Box JE, Decker DT. 2011. Greenland marine-terminating glacier area changes: 2000–2010. Annals of Glaciology 52:91–98. doi:10.3189/172756411799096312.

Brils M, Munneke PK, Jullien N, Tedstone AJ, Machguth H, van de Berg WJ, van den Broeke MR. 2024. Climatic Drivers of Ice Slabs and Firn Aquifers in Greenland. Geophysical Research Letters 51:e2023GL106613. doi:10.1029/2023GL106613. _eprint: https://agupubs.onlinelibrary.wiley.com/doi/pdf/10.1029/2023GL106613.

Cai C, Rignot E, Menemenlis D, Nakayama Y. 2017. Observations and modeling of ocean-induced melt beneath Petermann Glacier Ice Shelf in northwestern Greenland. Geophysical Research Letters 44:8396–8403. doi:10.1002/2017GL073711. _eprint: https://agupubs.onlinelibrary.wiley.com/doi/pdf/10.1002/2017GL073711.

Christoffersen P, Bougamont M, Hubbard A, Doyle SH, Grigsby S, Pettersson R. 2018. Cascading lake drainage on the Greenland Ice Sheet triggered by tensile shock and fracture. Nature Communications 9:1064. doi:10.1038/s41467-018-03420-8.

Chudley TR, Christoffersen P, Doyle SH, Bougamont M, Schoonman CM, Hubbard B, James MR. 2019. Supraglacial lake drainage at a fast-flowing Greenlandic outlet glacier. Proceedings of the National Academy of Sciences 116:25468–25477. doi:10.1073/pnas.1913685116.

Ciracì E, Rignot E, Scheuchl B, Tolpekin V, Wollersheim M, An L, Milillo P, Bueso-Bello JL, Rizzoli P, Dini L. 2023. Melt rates in the kilometer-size grounding zone of Petermann Glacier, Greenland, before and during a retreat. Proceedings of the National Academy of Sciences 120:e2220924120. doi:10.1073/pnas.2220924120. Company: National Academy of Sciences Distributor: National Academy of Sciences Institution: National Academy of Sciences Label: National Academy of Sciences.

Clerx N, Machguth H, Tedstone A, Jullien N, Wever N, Weingartner R, Roessler O. 2022. In situ measurements of meltwater flow through snow and firn in the accumulation zone of the SW Greenland Ice Sheet. The Cryosphere 16:4379–4401. doi:10.5194/tc-16-4379-2022.

Cowton TR, Sole AJ, Nienow PW, Slater DA, Christoffersen P. 2018. Linear response of east Greenland's tidewater glaciers to ocean/atmosphere warming. Proceedings of the National Academy of Sciences 115:7907–7912. doi:10.1073/pnas.1801769115.

Das SB, Joughin I, Behn MD, Howat IM, King MA, Lizarralde D, Bhatia MP. 2008. Fracture Propagation to the Base of the Greenland Ice Sheet During Supraglacial Lake Drainage. Science 320:778–781. doi:10.1126/science.1153360.

Dell RL, Banwell AF, Willis IC, Arnold NS, Halberstadt ARW, Chudley TR, Pritchard HD. 2022. Supervised classification of slush and ponded water on Antarctic ice shelves using Landsat 8 imagery. Journal of Glaciology 68:401–414. doi:10.1017/jog.2021.114.

Dell RL, Willis IC, Arnold NS, Banwell AF, de Roda Husman S. 2024. Substantial contribution of slush to meltwater area across Antarctic ice shelves. Nature Geoscience 17:624–630. doi:10.1038/s41561-024-01466-6.

Ehrenfeucht S, Rignot E, Morlighem M. 2024. Seawater Intrusion in the Observed Grounding Zone of Petermann Glacier Causes Extensive Retreat. Geophysical Research Letters 51:e2023GL107571. doi:10.1029/2023GL107571. _eprint: https://agupubs.onlinelibrary.wiley.com/doi/pdf/10.1029/2023GL107571.

Falkner KK, Melling H, Münchow AM, Box JE, Wohlleben T, Johnson HL, Gudmandsen P, Samelson R, Copland L, Steffen K, Rignot E, Higgins AK. 2011. Context for the Recent Massive Petermann Glacier Calving Event. Eos, Transactions American Geophysical Union 92:117–118. doi:10.1029/2011EO140001.

Fitzpatrick AAW, Hubbard AL, Box JE, Quincey DJ, Van As D, Mikkelsen APB, Doyle SH, Dow CF, Hasholt B, Jones GA. 2014. A decade (2002–2012) of supraglacial lake volume estimates across Russell Glacier, West Greenland. The Cryosphere 8:107–121. doi:10.5194/tc-8-107-2014.

Forster RR, Box JE, Van Den Broeke MR, Miège C, Burgess EW, Van Angelen JH, Lenaerts JTM, Koenig LS, Paden J, Lewis C, Gogineni SP, Leuschen C, McConnell JR. 2014. Extensive liquid meltwater storage in firn within the Greenland ice sheet. Nature Geoscience 7:95–98. doi:10.1038/ngeo2043.

Glen E, Banwell AF, Miles KE, Leeson AA, Dell RL, McMillan M, Maddalena J. 2025a. A nine-year record of slush on the Greenland Ice Sheet. doi:10.5194/egusphere-2025-5159.

Glen E, Leeson A, Banwell AF, Maddalena J, Corr D, Atkins O, Noël B, McMillan M. 2025b. A comparison of supraglacial meltwater features throughout contrasting melt seasons: southwest Greenland. The Cryosphere 19:1047–1066. doi:10.5194/tc-19-1047-2025.

Gorelick N, Hancher M, Dixon M, Ilyushchenko S, Thau D, Moore R. 2017. Google Earth Engine: Planetary-scale geospatial analysis for everyone. Remote Sensing of Environment 202:18–27. doi:10.1016/j.rse.2017.06.031.

Greuell W, Knap WH. 2000. Remote sensing of the albedo and detection of the slush line on the Greenland ice sheet. Journal of Geophysical Research: Atmospheres 105:15567–15576. doi:10.1029/1999JD901162. _eprint: https://agupubs.onlinelibrary.wiley.com/doi/pdf/10.1029/1999JD901162.

Hamed KH, Ramachandra Rao A. 1998. A modified Mann-Kendall trend test for autocorrelated data. Journal of Hydrology 204:182–196. doi:10.1016/S0022-1694(97)00125-X.

Hill E, Carr R, Stokes C, Gudmundsson G. 2018a. Dynamic changes in outlet glaciers in northern Greenland from 1948 to 2015. The Cryosphere 12:3243–3263. doi:10.5194/tc-12-3243-2018.

Hill EA, Carr JR, Stokes CR. 2017. A Review of Recent Changes in Major Marine-Terminating Outlet Glaciers in Northern Greenland. Frontiers in Earth Science 4. doi:10.3389/feart.2016.00111.

Hill EA, Gudmundsson GH, Carr JR, Stokes CR. 2018b. Velocity response of Petermann Glacier, northwest Greenland, to past and future calving events. The Cryosphere 12:3907–3921. doi:10.5194/tc-12-3907-2018.

Howat IM, Negrete A, Smith BE. 2014. The Greenland Ice Mapping Project (GIMP) land

classification and surface elevation data sets. The Cryosphere 8:1509–1518. doi:10.5194/tc-8-1509-2014.

Humbert A, Helm V, Neckel N, Zeising O, Rückamp M, Khan SA, Loebel E, Brauchle J, Stebner K, Gross D, Sondershaus R, Müller R. 2023. Precursor of disintegration of Greenland's largest floating ice tongue. The Cryosphere 17:2851–2870. doi:10.5194/tc-17-2851-2023.

Jakobsson M, Hogan KA, Mayer LA, Mix A, Jennings A, Stoner J, Eriksson B, Jerram K, Mohammad R, Pearce C, Reilly B, Stranne C. 2018. The Holocene retreat dynamics and stability of Petermann Glacier in northwest Greenland. Nature Communications 9:2104. doi:10.1038/s41467-018-04573-2.

Jakobsson M, Kirchner N, Nilsson J, Stranne C, Mayer L, Barnett J, Holmes F, Calder B, Deutsch C, de Boer A, Coxall H, Faehnrich K, Hong WL, Hopper J, Ketzer M, Noormets R, O'Regan M, Ross N, Sigray P, Strandell Erstorp E, Weidner E, Wang Z, GEOEO 2024 Shipboard Scientific Party. 2026. Atlantic water access and the break-up of the C.H. Ostenfeld Gletsjer ice tongue, Northwest Greenland. Communications Earth & Environment .

Jakobsson M, Mayer LA, Bringensparr C, Castro CF, Mohammad R, Johnson P, Ketter T, Accettella D, Amblas D, An L, Arndt JE, Canals M, Casamor JL, Chauché N, Coakley B, Danielson S, Demarte M, Dickson ML, Dorschel B, Dowdeswell JA, Dreutter S, Fremand AC, Gallant D, Hall JK, Hehemann L, Hodnesdal H, Hong J, Ivaldi R, Kane E, Klaucke I, Krawczyk DW, Kristoffersen Y, Kuipers BR, Millan R, Masetti G, Morlighem M, Noormets R, Prescott MM, Rebesco M, Rignot E, Semiletov I, Tate AJ, Travaglini P, Velicogna I, Weatherall P, Weinrebe W, Willis JK, Wood M, Zarayskaya Y, Zhang T, Zimmermann M, Zinglersen KB. 2020. The International Bathymetric Chart of the Arctic Ocean Version 4.0. Scientific Data 7:176. doi:10.1038/s41597-020-0520-9.

Jiang T, Shen H, Li H, Zhang C, Xu L, Lin D. 2024. A fast and robust cirrus removal method for Landsat 8/9 images. International Journal of Applied Earth Observation and Geoinformation 128:103691. doi:10.1016/j.jag.2024.103691.

Joughin I, Smith BE, Howat IM, Floricioiu D, Alley RB, Truffer M, Fahnestock M. 2012. Seasonal to decadal scale variations in the surface velocity of Jakobshavn Isbrae, Greenland: Observation and model-based analysis. Journal of Geophysical Research: Earth Surface 117. doi:10.1029/2011JF002110. _eprint: https://agupubs.onlinelibrary.wiley.com/doi/pdf/10.1029/2011JF002110.

Joughin I, Smith BE, Howat IM, Scambos T, Moon T. 2010. Greenland flow variability from ice-sheet-wide velocity mapping. Journal of Glaciology 56:415–430. doi:10.3189/002214310792447734.

Kang Yang, Smith LC. 2013. Supraglacial Streams on the Greenland Ice Sheet Delineated From Combined Spectral–Shape Information in High-Resolution Satellite Imagery. IEEE Geoscience and Remote Sensing Letters 10:801–805. doi:10.1109/LGRS.2012.2224316.

Karlsson NB, Solgaard AM, Mankoff KD, Gillet-Chaulet F, MacGregor JA, Box JE, Citterio M, Colgan WT, Larsen SH, Kjeldsen KK, Korsgaard NJ, Benn DI, Hewitt IJ, Fausto RS. 2021. A first constraint on basal melt-water production of the Greenland ice sheet. Nature Communications 12:3461. doi:10.1038/s41467-021-23739-z.

Khan SA, Bjørk AA, Bamber JL, Morlighem M, Bevis M, Kjær KH, Mouginot J, Løkkegaard A, Holland DM, Aschwanden A, Zhang B, Helm V, Korsgaard NJ, Colgan W, Larsen NK, Liu L, Hansen K, Barletta V, Dahl-Jensen TS, Søndergaard AS, Csatho BM, Sasgen I, Box J, Schenk T. 2020. Centennial response of Greenland's three largest outlet glaciers. Nature Communications 11:5718. doi:10.1038/s41467-020-19580-5.

Lai CY, Kingslake J, Wearing MG, Chen PHC, Gentine P, Li H, Spergel JJ, Van Wessem JM. 2020. Vulnerability of Antarctica's ice shelves to meltwater-driven fracture. Nature 584:574–578. doi:10.1038/s41586-020-2627-8.

Li D, Jiang L, Huang R. 2021. Hydrological and Kinematic Precursors of the 2017 Calving Event at the Petermann Glacier in Greenland Observed from Multi-Source Remote Sensing Data. Remote Sensing 13:591. doi:10.3390/rs13040591.

Li G, Mao Y, Feng X, Chen Z, Yang Z, Cheng X. 2023. Monitoring ice flow velocity of Petermann glacier combined with Sentinel-1 and −2 imagery. International Journal of Applied Earth Observation and Geoinformation 121:103374. doi:10.1016/j.jag.2023.103374.

Li Z, Chong J, Zhao Y, Diao L. 2024. Reconstruction of Petermann glacier velocity time series using multi-source remote sensing images. International Journal of Applied Earth Observation and Geoinformation 135:104307. doi:10.1016/j.jag.2024.104307.

MacFerrin M, Machguth H, As Dv, Charalampidis C, Et A. 2019. Rapid expansion of Greenland's low-permeability ice slabs. Nature doi:10.1038/s41586-019-1550-3.

Machguth H, Tedstone AJ, Mattea E. 2023. Daily variations in Western Greenland slush limits, 2000–2021. Journal of Glaciology 69:191–203. doi:10.1017/jog.2022.65.

Mahagaonkar A, Moholdt G, Glaude Q, Schuler TV. 2024. Supraglacial lake evolution and its drivers in Dronning Maud Land, East Antarctica. Journal of Glaciology 70:e49. doi:10.1017/jog.2024.66.

Mankoff KD, Noël B, Fettweis X, Ahlstrøm AP, Colgan W, Kondo K, Langley K, Sugiyama S, van As D, Fausto RS. 2020. Greenland liquid water discharge from 1958 through 2019. Earth System Science Data 12:2811–2841. doi:10.5194/essd-12-2811-2020.

Mann HB. 1945. Nonparametric Tests Against Trend. Econometrica 13:245–259. doi:10.2307/1907187.

Maritorena S, Morel A, Gentili B. 1994. Diffuse reflectance of oceanic shallow waters: Influence of water depth and bottom albedo. Limnology and Oceanography 39:1689–1703. doi:10.4319/lo.1994.39.7.1689. _eprint: https://aslopubs.onlinelibrary.wiley.com/doi/pdf/10.4319/lo.1994.39.7.1689.

Miles KE, Willis IC, Benedek CL, Williamson AG, Tedesco M. 2017. Toward Monitoring Surface and Subsurface Lakes on the Greenland Ice Sheet Using Sentinel-1 SAR and Landsat-8 OLI Imagery. Frontiers in Earth Science 5. doi:10.3389/feart.2017.00058.

Millan R, Jager E, Mouginot J, Wood MH, Larsen SH, Mathiot P, Jourdain NC, Bjørk A. 2023. Rapid disintegration and weakening of ice shelves in North Greenland. Nature Communications 14:6914. doi:10.1038/s41467-023-42198-2.

Millan R, Mouginot J, Derkacheva A, Rignot E, Milillo P, Ciraci E, Dini L, Bjørk A. 2022. Ongoing grounding line retreat and fracturing initiated at the Petermann Glacier ice shelf, Greenland, after 2016. The Cryosphere 16:3021–3031. doi:10.5194/tc-16-3021-2022.

Miège C, Forster RR, Brucker L, Koenig LS, Solomon DK, Paden JD, Box JE, Burgess EW, Miller JZ, McNerney L, Brautigam N, Fausto RS, Gogineni S. 2016. Spatial extent and temporal variability of Greenland firn aquifers detected by ground and airborne radars. Journal of Geophysical Research: Earth Surface 121:2381–2398. doi:10.1002/2016JF003869. _eprint: https://agupubs.onlinelibrary.wiley.com/doi/pdf/10.1002/2016JF003869.

Mouginot J, Rignot E. 2019. Glacier catchments/basins for the Greenland Ice Sheet. doi:10.7280/D1WT11. Artwork Size: 4156976 bytes Pages: 4156976 bytes.

Mouginot J, Rignot E, Bjørk AA, van den Broeke M, Millan R, Morlighem M, Noël B, Scheuchl B, Wood M. 2019. Forty-six years of Greenland Ice Sheet mass balance from 1972 to 2018. Proceedings of the National Academy of Sciences 116:9239–9244. doi:10.1073/pnas.1904242116. Company: National Academy of Sciences Distributor: National Academy of Sciences Institution: National Academy of Sciences Label: National Academy of Sciences.

Moussavi M, Pope A, Halberstadt ARW, Trusel LD, Cioffi L, Abdalati W. 2020. Antarctic Supraglacial Lake Detection Using Landsat 8 and Sentinel-2 Imagery: Towards Continental Generation of Lake Volumes. Remote Sensing 12:134. doi:10.3390/rs12010134. Number: 1.

Moussavi MS, Abdalati W, Pope A, Scambos T, Tedesco M, MacFerrin M, Grigsby S. 2016. Derivation and validation of supraglacial lake volumes on the Greenland Ice Sheet from high-resolution satellite imagery. Remote Sensing of Environment 183:294–303. doi:10.1016/j.rse.2016.05.024.

Munneke PK, M Ligtenberg SR, van den Broeke MR, van Angelen JH, Forster RR. 2014. Ex-

plaining the presence of perennial liquid water bodies in the firn of the Greenland Ice Sheet. Geophysical Research Letters 41:476–483. doi:10.1002/2013GL058389. _eprint: https://agupubs.onlinelibrary.wiley.com/doi/pdf/10.1002/2013GL058389.

Muñoz-Sabater J, Dutra E, Agustí-Panareda A, Albergel C, Arduini G, Balsamo G, Boussetta S, Choulga M, Harrigan S, Hersbach H, Martens B, Miralles DG, Piles M, Rodríguez-Fernández NJ, Zsoter E, Buontempo C, Thépaut JN. 2021. ERA5-Land: a state-of-the-art global reanalysis dataset for land applications. Earth System Science Data 13:4349–4383. doi:10.5194/essd-13-4349-2021.

Münchow A, Padman L, Fricker HA. 2014. Interannual changes of the floating ice shelf of Petermann Gletscher, North Greenland, from 2000 to 2012. Journal of Glaciology 60:489–499. doi:10.3189/2014JoG13J135.

Münchow A, Padman L, Washam P, Nicholls K. 2016. The Ice Shelf of Petermann Gletscher, North Greenland, and Its Connection to the Arctic and Atlantic Oceans. Oceanography 29:84–95. doi:10.5670/oceanog.2016.101.

Neckel N, Zeising O, Steinhage D, Helm V, Humbert A. 2020. Seasonal Observations at 79°N Glacier (Greenland) From Remote Sensing and in situ Measurements. Frontiers in Earth Science 8. doi:10.3389/feart.2020.00142.

O'Regan M, Cronin TM, Reilly B, Alstrup AKO, Gemery L, Golub A, Mayer LA, Morlighem M, Moros M, Munk OL, Nilsson J, Pearce C, Detlef H, Stranne C, Vermassen F, West G, Jakobsson M. 2021. The Holocene dynamics of Ryder Glacier and ice tongue in north Greenland. The Cryosphere 15:4073–4097. doi:10.5194/tc-15-4073-2021.

Otto J, Holmes FA, Kirchner N. 2022. Supraglacial lake expansion, intensified lake drainage frequency, and first observation of coupled lake drainage, during 1985–2020 at Ryder Glacier, Northern Greenland. Frontiers in Earth Science 10. doi:10.3389/feart.2022.978137.

Pettitt AN. 1979. A Non-Parametric Approach to the Change-Point Problem. Journal of the Royal Statistical Society: Series C (Applied Statistics) 28:126–135. doi:10.2307/2346729. _eprint: https://rss.onlinelibrary.wiley.com/doi/pdf/10.2307/2346729.

Philpot WD. 1989. Bathymetric mapping with passive multispectral imagery. Applied Optics 28:1569–1578. doi:10.1364/AO.28.001569.

Poinar K, Joughin I, Das SB, Behn MD, Lenaerts JTM, van den Broeke MR. 2015. Limits to future expansion of surface-melt-enhanced ice flow into the interior of western Greenland. Geophysical Research Letters 42:1800–1807. doi:10.1002/2015GL063192. _eprint: https://agupubs.onlinelibrary.wiley.com/doi/pdf/10.1002/2015GL063192.

Pons X, Cea C, González-Guerrero , Cristóbal J. 2025. Landsat Collection 2: Key Information and recommendations for data users and product developers. Revista de Teledetección doi:10.4995/raet.2025.23510.

Pope A, Scambos TA, Moussavi M, Tedesco M, Willis M, Shean D, Grigsby S. 2016. Estimating supraglacial lake depth in West Greenland using Landsat 8 and comparison with other multispectral methods. The Cryosphere 10:15–27. doi:10.5194/tc-10-15-2016.

Prakash A, Zhou Q, Hattermann T, Bao W, Graversen R, Kirchner N. 2022. A nested high-resolution unstructured grid 3-D ocean-sea ice-ice shelf setup for numerical investigations of the Petermann ice shelf and fjord. MethodsX 9:101668. doi:10.1016/j.mex.2022.101668.

Prakash A, Zhou Q, Hattermann T, Kirchner N. 2023. Impact of the Nares Strait sea ice arches on the long-term stability of the Petermann Glacier ice shelf. The Cryosphere 17:5255–5281. doi:10.5194/tc-17-5255-2023.

Prakash A, Zhou Q, Hattermann T, Kirchner N. 2025. Enhanced subglacial discharge amplifies Petermann Ice Shelf melting when ocean thermal forcing saturates. Nature Communications 16:4213. doi:10.1038/s41467-025-59469-9.

Pritchard HD, Arthern RJ, Vaughan DG, Edwards LA. 2009. Extensive dynamic thinning on the margins of the Greenland and Antarctic ice sheets. Nature 461:971–975. doi:10.1038/nature08471.

Reilly BT, Stoner JS, Mix AC, Walczak MH, Jennings A, Jakobsson M, Dyke L, Glueder A,

Nicholls K, Hogan KA, Mayer LA, Hatfield RG, Albert S, Marcott S, Fallon S, Cheseby M. 2019. Holocene break-up and reestablishment of the Petermann Ice Tongue, Northwest Greenland. Quaternary Science Reviews 218:322–342. doi:10.1016/j.quascirev.2019.06.023.

Richardson BA, Rehfeldt GE, Sáenz-Romero C, Milano ER. 2024. A climate analog approach to evaluate seed transfer and vegetation transitions. Frontiers in Forests and Global Change 7:1325264. doi:10.3389/ffgc.2024.1325264.

Rignot E, Steffen K. 2008. Channelized bottom melting and stability of floating ice shelves. Geophysical Research Letters 35. doi:10.1029/2007GL031765. _eprint: https://agupubs.onlinelibrary.wiley.com/doi/pdf/10.1029/2007GL031765.

Rignot EJ, Gogineni SP, Krabill WB, Ekholm S. 1997. North and Northeast Greenland Ice Discharge from Satellite Radar Interferometry. Science 276:934–937. doi:10.1126/science.276.5314.934.

Rückamp M, Neckel N, Berger S, Humbert A, Helm V. 2019. Calving Induced Speedup of Petermann Glacier. Journal of Geophysical Research: Earth Surface 124:216–228. doi:10.1029/2018JF004775.

Saydi M, Ding Jl. 2020. Impacts of topographic factors on regional snow cover characteristics. Water Science and Engineering 13:171–180. doi:10.1016/j.wse.2020.09.002.

Scambos T, Fricker HA, Liu CC, Bohlander J, Fastook J, Sargent A, Massom R, Wu AM. 2009. Ice shelf disintegration by plate bending and hydro-fracture: Satellite observations and model results of the 2008 Wilkins ice shelf break-ups. Earth and Planetary Science Letters 280:51–60. doi:10.1016/j.epsl.2008.12.027.

Schoof C. 2007. Ice sheet grounding line dynamics: Steady states, stability, and hysteresis. Journal of Geophysical Research: Earth Surface 112. doi:10.1029/2006JF000664. _eprint: https://agupubs.onlinelibrary.wiley.com/doi/pdf/10.1029/2006JF000664.

Schoof C, Hewitt I. 2013. Ice-Sheet Dynamics. Annual Review of Fluid Mechanics 45:217–239. doi:10.1146/annurev-fluid-011212-140632.

Slater DA, Carroll D, Oliver H, Hopwood MJ, Straneo F, Wood M, Willis JK, Morlighem M. 2022. Characteristic Depths, Fluxes, and Timescales for Greenland's Tidewater Glacier Fjords From Subglacial Discharge-Driven Upwelling During Summer. Geophysical Research Letters 49:e2021GL097081. doi:10.1029/2021GL097081.

Slater DA, Straneo F, Felikson D, Little CM, Goelzer H, Fettweis X, Holte J. 2019. Estimating Greenland tidewater glacier retreat driven by submarine melting. The Cryosphere 13:2489–2509. doi:10.5194/tc-13-2489-2019.

Smith T, Boers N. 2023. Global vegetation resilience linked to water availability and variability. Nature Communications 14:498. doi:10.1038/s41467-023-36207-7.

Straneo F, Heimbach P. 2013. North Atlantic warming and the retreat of Greenland's outlet glaciers. Nature 504:36–43. doi:10.1038/nature12854.

Tedstone A, Machguth H, Clerx N, Jullien N, Picton H, Ducrey J, van As D, Colosio P, Tedesco M, Lhermitte S. 2025. Concurrent superimposed ice formation and meltwater runoff on Greenland's ice slabs. Nature Communications 16:4494. doi:10.1038/s41467-025-59237-9.

Tedstone AJ, Machguth H. 2022. Increasing surface runoff from Greenland's firn areas. Nature Climate Change 12:672–676. doi:10.1038/s41558-022-01371-z.

Tinto KJ, Bell RE, Cochran JR, Münchow A. 2015. Bathymetry in Petermann fjord from Operation IceBridge aerogravity. Earth and Planetary Science Letters 422:58–66. doi:10.1016/j.epsl.2015.04.009.

Trusel L, Pan Z, Moussavi M. 2022. Repeated Tidally Induced Hydrofracture of a Supraglacial Lake at the Amery Ice Shelf Grounding Zone. Geophysical Research Letters 49. doi:10.1029/2021GL095661.

Tuckett PA, Sole AJ, Livingstone SJ, Jones JM, Lea JM, Gilbert E. 2025. Continent-wide mapping shows increasing sensitivity of East Antarctica to meltwater ponding. Nature Climate Change 15:775–783. doi:10.1038/s41558-025-02363-5.

USGS. 2024. Landsat Collection 2 Known Issues | U.S. Geological Survey.

Van Der Veen C. 1998. Fracture mechanics approach to penetration of surface crevasses on glaciers. Cold Regions Science and Technology 27:31–47. doi:10.1016/S0165-232X(97)00022-0.

Vandecrux B, Mottram R, Langen PL, Fausto RS, Olesen M, Stevens CM, Verjans V, Leeson A, Ligtenberg S, Kuipers Munneke P, Marchenko S, Van Pelt W, Meyer CR, Simonsen SB, Heilig A, Samimi S, Marshall S, Machguth H, MacFerrin M, Niwano M, Miller O, Voss CI, Box JE. 2020. The firn meltwater Retention Model Intercomparison Project (RetMIP): evaluation of nine firn models at four weather station sites on the Greenland ice sheet. The Cryosphere 14:3785–3810. doi:10.5194/tc-14-3785-2020.

Veraart AJ, Faassen EJ, Dakos V, van Nes EH, Lürling M, Scheffer M. 2012. Recovery rates reflect distance to a tipping point in a living system. Nature 481:357–359. doi:10.1038/nature10723.

Washam P, Münchow A, Nicholls KW. 2018. A Decade of Ocean Changes Impacting the Ice Shelf of Petermann Gletscher, Greenland. Journal of Physical Oceanography 48:2477–2493. doi:10.1175/JPO-D-17-0181.1.

Washam P, Nicholls KW, Münchow A, Padman L. 2020. Tidal Modulation of Buoyant Flow and Basal Melt Beneath Petermann Gletscher Ice Shelf, Greenland. Journal of Geophysical Research: Oceans 125:e2020JC016427. doi:10.1029/2020JC016427. _eprint: https://agupubs.onlinelibrary.wiley.com/doi/pdf/10.1029/2020JC016427.

Weertman J. 1969. Can a water-filled crevasse reach the bottom surface of a glacier? In: Symposium on the Hydrology of Glaciers. volume Publication no. 95. Cambridge: International Association of Scientific Hydrology. p. 139–145.

White HJ, Gaul W, Sadykova D, León-Sánchez L, Caplat P, Emmerson MC, Yearsley JM. 2020. Quantifying large-scale ecosystem stability with remote sensing data. Remote Sensing in Ecology and Conservation 6:354–365. doi:10.1002/rse2.148.

Williamson AG, Banwell AF, Willis IC, Arnold NS. 2018. Dual-satellite (Sentinel-2 and Landsat 8) remote sensing of supraglacial lakes in Greenland. The Cryosphere 12:3045–3065. doi:10.5194/tc-12-3045-2018.

Wilson N, Straneo F, Heimbach P. 2017. Satellite-derived submarine melt rates and mass balance (2011–2015) for Greenland's largest remaining ice tongues. The Cryosphere 11:2773–2782. doi:10.5194/tc-11-2773-2017.

Xi L, Liming J, Daan L, Yi L, Andrew S, Stephen J L. 2026. Ice front positions for Greenland glaciers (2002–2021): a spatially extensive seasonal record and benchmark dataset for algorithm validation. doi:10.5281/zenodo.19181770.

Yegorova SV, Dobrowski SZ, Yung L, Parks SA, Bocinsky RK, Davis KT, Littlefield C, Maneta MP, Wyborn C, Wurster P, Rank R, Brinkerhoff D, Colligan T. 2025. Spatial climate analogs in climate change research, impact assessment, and decision-making. BioScience 75:362–378. doi:10.1093/biosci/biaf031.

Zhou Q, Liang Q, Xiao W, Li T, Zheng L, Cheng X. 2025. Supraglacial Lake Depth Retrieval from ICESat-2 and Multispectral Imagery Datasets. Journal of Remote Sensing 5:0416. doi:10.34133/remotesensing.0416.

Åkesson H, Morlighem M, Nilsson J, Stranne C, Jakobsson M. 2022. Petermann ice shelf may not recover after a future breakup. Nature Communications 13:2519. doi:10.1038/s41467-022-29529-5.

Appendix

Some appendix TOC content goes here one day

A Training Data

Table A1. Cluster counts used to compose the final training classes.

Class	Total clusters	PTM clusters	OST clusters
Lake	14 main + 0 sub	7 main + 0 sub	7 main + 0 sub
Slush	11 main + 18 sub	7 main + 9 sub	4 main + 9 sub
Blue ice	22 main + 18 sub	6 main + 7 sub	16 main + 11 sub

B ERA5-Land variables vs. melt metrics scatter plots

C Footprint coverage

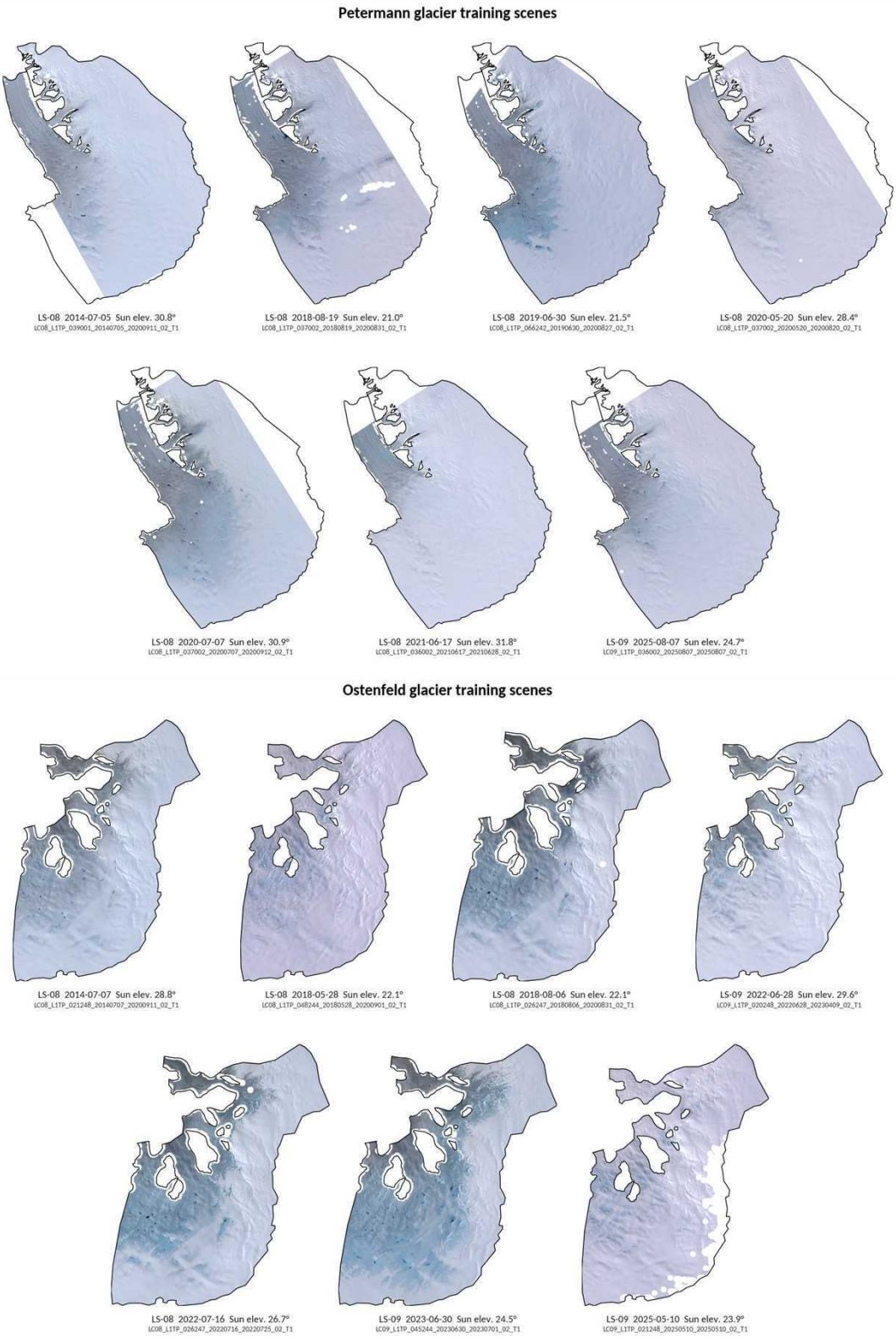

Figure A1. Visible bands from the preprocessed Landsat-8, -09, TOA, collection 2, level 1, training scenes used for Petermann (top) and Ostenfeld (bottom). Training scenes are displayed within the study area boundary and below each the sensing platform, date, solar elevation, and USGS Landsat scene ID is printed. Scenes are preprocessed with a threshold based rock mask Moussavi et al. (2020) and QA_bit cloud mask. Training clustered with k-means and manually classified to generate training data for the RF classifier.

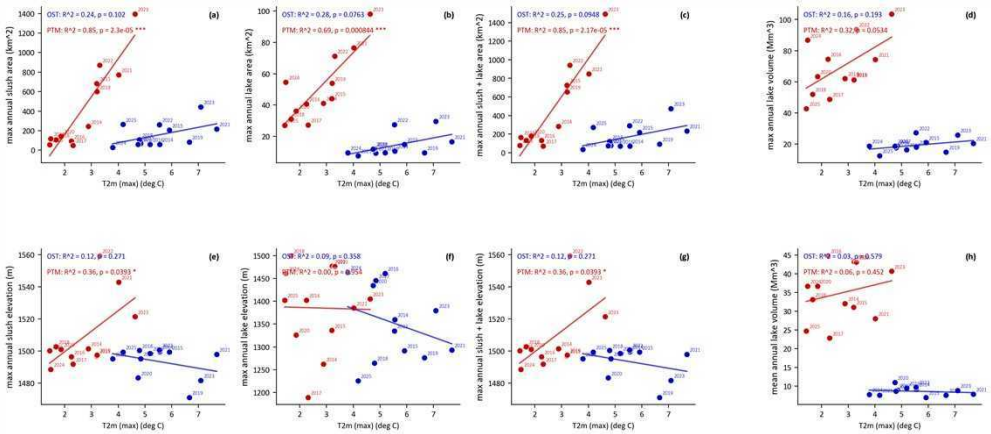

Figure A2. Ostenfeld (blue) + Petermann (red) scatter of JJA maximum 2 m temperature against JJA maximum annual (a) slush area, (b) lake area, (c) combined area, (d) lake volume, (e) slush elevation, (f) lake elevation, (g) combined elevation, (h) mean lake volume.

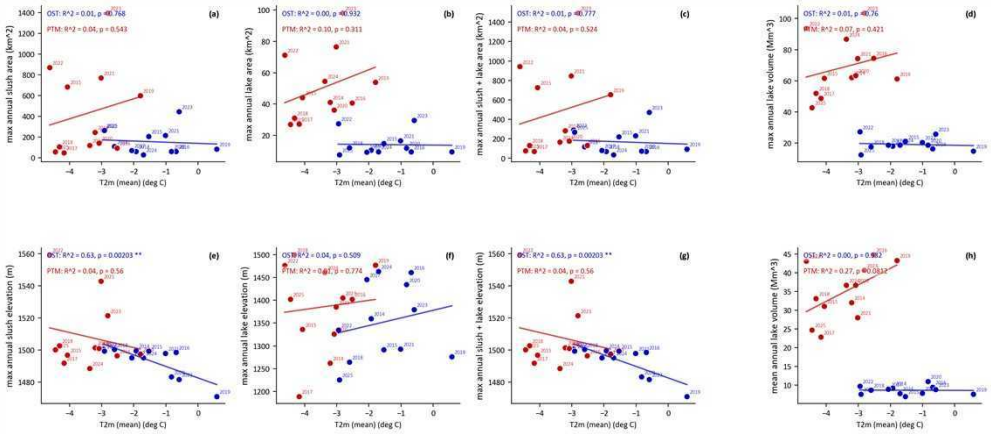

Figure A3. Ostenfeld (blue) + Petermann (red) scatter of JJA mean 2 m temperature against JJA maximum annual (a) slush area, (b) lake area, (c) combined area, (d) lake volume, (e) slush elevation, (f) lake elevation, (g) combined elevation, (h) mean lake volume.

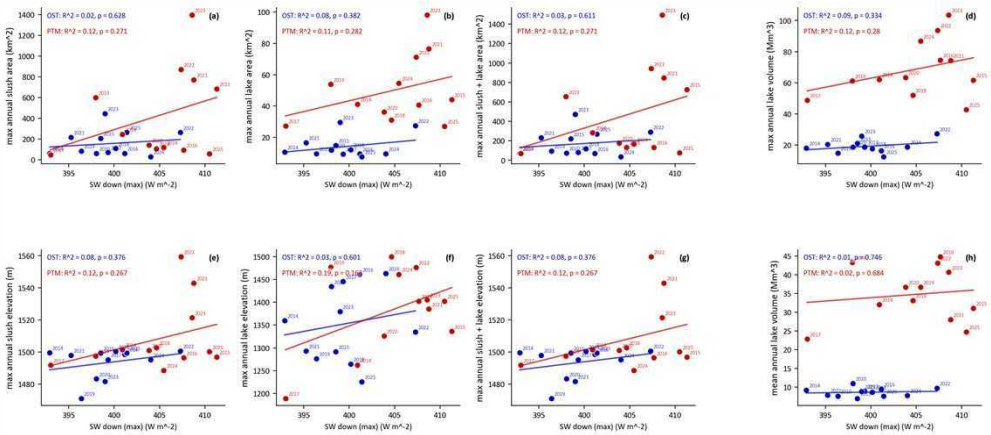

Figure A4. Ostenfeld (blue) + Petermann (red) scatter of JJA maximum short wave down welling radiation against JJA maximum annual (a) slush area, (b) lake area, (c) combined area, (d) lake volume, (e) slush elevation, (f) lake elevation, (g) combined elevation, (h) mean lake volume.

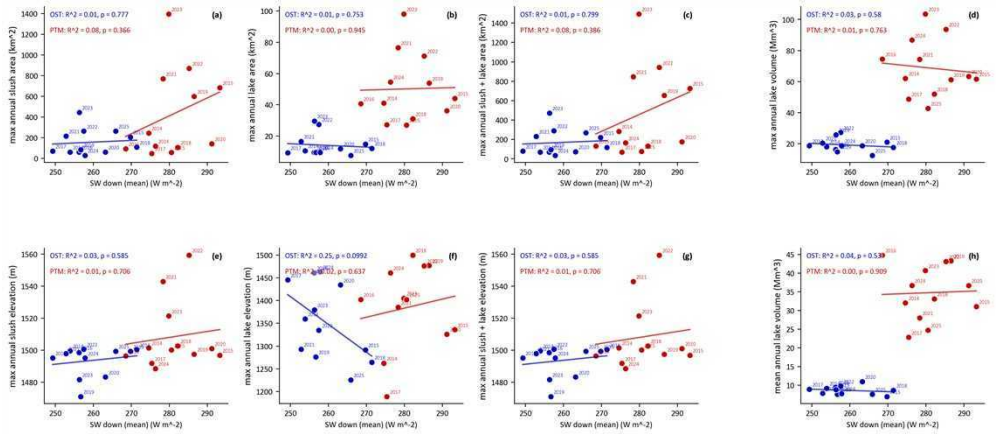

Figure A5. Ostenfeld (blue) + Petermann (red) scatter of JJA mean short wave down welling radiation against JJA maximum annual (a) slush area, (b) lake area, (c) combined area, (d) lake volume, (e) slush elevation, (f) lake elevation, (g) combined elevation, (h) mean lake volume.

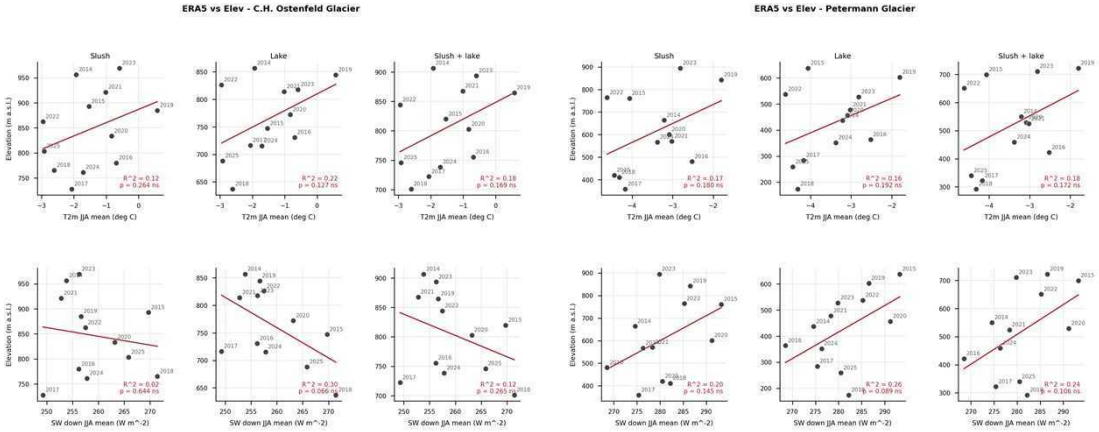

Figure A6. Annual melt elevation metrics at Ostenfeld (left) and Petermann (right) against ERA5-Land JJA mean 2 m temperature (top row) and JJA mean downwelling shortwave radiation (bottom row).

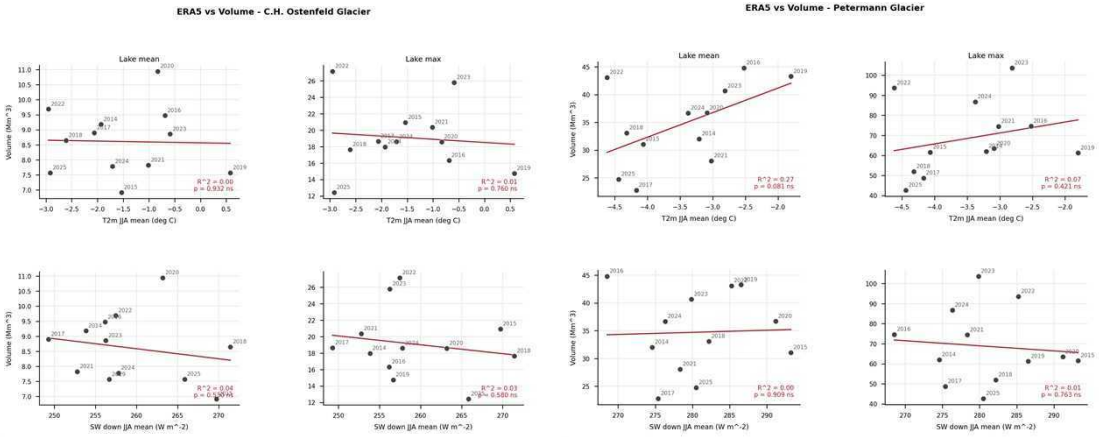

Figure A7. Annual volume metrics at Ostenfeld (left) and Petermann (right) against ERA5-Land JJA mean 2 m temperature (top row) and JJA mean downwelling shortwave radiation (bottom row).

Figure A8. Observed Landsat footprint coverage for 2-day classified windows and anchored 10-day blocks over C.H. Ostenfeld Glacier and Petermann Glacier. Panels (a) and (b) show C.H. Ostenfeld Glacier and Petermann Glacier, respectively, for the 2014–2025 analysis period. Within each year, the upper thin band represents individual 2-day observation windows and the lower thicker band represents contiguous five-window blocks anchored to 1 May; only observed footprint coverage is shown. Color indicates the fraction of the AOI footprint observed, from red for low coverage to green for near-complete coverage; grey cells indicate no observation. The June-July-August (JJA) analysis window is enclosed by the black outline, while May and September observations are retained as semi-transparent melt-season context. Dashed vertical lines mark the regular 10-day anchored block boundaries. Hatched block segments identify JJA blocks with less than 80% AOI footprint coverage. Panels (c) and (d) summarize C.H. Ostenfeld Glacier and Petermann Glacier, respectively, by plotting annual JJA mean footprint coverage for the 2-day windows (blue circles) and anchored 10-day blocks (green squares). Vertical reference lines mark the 10% minimum window coverage threshold used for annual inclusion and the 80% low-block-coverage flag used in this figure. The purple dash-dot horizontal line marks the boundary before the 2022 JJA rows, the first JJA season after Landsat 9 data entered the analysis-period catalog. Labels at the right of each summary panel give the number of valid JJA windows and valid JJA blocks for each year, formatted as windows/blocks.

D Data and code list

All scripts, CSV outputs, vector shapefiles, and raster products referenced in Section 4 are listed below by category, in the order in which they appear in the processing pipeline. Earth Engine collections that are too numerous to list individually (per-window classified raster collections, per-window vector shapefile collections) are listed as a single line item. The supplementary data and code archive can be accessed here: https://stockholmuniversity-my.sharepoint.com/:f:/g/personal/luur4790_win_su_se/IgA3_anPDYUISYQ4xAYoSRqMAbRP5bm3BWJrrhtWScZb9bE?e=Ufauje
Classified rasters are hosted as EE assets and accessible with an Earth Engine account here: https://code.earthengine.google.com/?asset=projects/vernal-signal-270100/assets/ClassifiedMosaics

D.1 Earth Engine scripts (stage 1)

Table A2. Earth Engine JavaScript scripts used in processing stage-1 (training-data generation, mosaicking, classification, depth retrieval, validation, climate, and spatial-product export). All scripts appear in data supplement with `gee_js/` path prefix.

Script	Methods section	Role
`k_means_class_def_v05.js`	4.3.2, 4.3.3	K-means cluster definition on the 14 training scenes; manual-classing UI and per-cluster $\mathrm{NDWI}_{\mathrm{ice}}$ readouts.
`export_v06.js`	4.4.1, 4.4.2	Per-AOI per-year run: 2-day $\mathrm{NDWI}_{\mathrm{ice}}$-medoid mosaicking, RF classification, per-window classified raster export.
`deepwater_lookup.js`	4.5	Builds the per-AOI R_∞ lookup table from open-ocean polygons in Nares Strait and Victoria Fjord.
`export_rinf_lut_csv.js`	4.5	Exports the per-AOI R_∞ lookup table as CSV.
`volume_v06.js`	4.5	Per-AOI run: Pope/Moussavi two-band depth retrieval; per-window lake, slush, footprint vector exports.
`volume_sensitivity_v01.js`	4.5	$\pm 20\,\%$ perturbation tests on g_{red}, g_{pan}, A_d^{B4}, A_d^{B8} for six representative lakes.
`validation_classifier.js`	4.4.3	Runs the deployed classifier on the 10 validation scenes.
`rf_error_metrics_by_validation_scene.js`	4.4.3	Per-validation-scene holdout precision, recall, F_1, support, accuracy, κ.
`rf_error_metrics_by_window.js`	4.4.3	Per-window holdout metrics for selected AOI-year scenes.
`export_max_melt_medoids.js`	4.6.5	Per-AOI per-year max-melt-block RGB medoid TIF export.
`era5/era5_land_aoi_export.js`	4.1, 4.6.4	Per-AOI daily ERA5-Land T_{2m} and $\mathrm{SW}_{\downarrow}$, 2013–2025, May–September.
`era5/era5_land_bin_export.js`	4.1, 4.6.4	Per-aspect-elevation-bin daily ERA5-Land T_{2m} and $\mathrm{SW}_{\downarrow}$.
`drainage_event_viewer.js`	4.6.6	Interactive viewer for inspecting per-event pre- and post-drainage volumes.

D.2 Python scripts (stage 2)

Table A3. Python scripts used in stage-2, post-processing workflow. All scripts appear in the data supplement with `python/` path prefix.

Script	Methods section	Role
`add_elevation_to_shapefiles.py`	4.6.1	Adds $\mathrm{elev}_{\mathrm{mean,min,max}}$ attributes to per-window slush, lake, footprint shapefiles from the MEaSUREs DEM.
`create_elevation_bins.py`	4.6.1	100 m elevation-band shapefiles per AOI from the MEaSUREs DEM, capped at 1500 m.
`split_elevation_bins_by_aspect.py`	4.6.1	NW/NE aspect subdivision of the five largest elevation bands per AOI.
`add_bin_id_to_aspect_elevation_bins.py`	4.6.1	Adds the per-bin `bin_id` field used by the ERA5 per-bin export and the selectors.
`fix_ptm_bins.py`	4.6.1	Fixes orphan low-elevation bin patches in the Ptm. elevation-bin shapefile.

Table A3 continued.

Script	Methods section	Role
summary_table.py	4.6.1	Per-window AOI totals: footprint area, slush area, lake area, lake volume, lake count.
footprint_table.py	4.6.1	Per-window footprint area and proportion.
analyze_raw_summary.py	4.6.1	IQR-based outlier-window detection on slush- and lake-relative area.
footprint_area_by_aspect_elev_bins.py	4.6.1, 4.6.1	Per-window footprint area per aspect-elevation bin.
melt_area_by_aspect_elev_bins.py	4.6.1	Per-window slush and lake area per aspect-elevation bin.
create_lake_volume_csv_data.py	4.6.1	Per-window lake volume per aspect-elevation bin.
project_melt_area_by_aoi.py	4.6.1	Per-AOI projection (scaled = observed + projected) for slush and lake area.
project_melt_area_by_aspect_elev_bins.py	4.6.1	Per-aspect-elevation-bin projection used in the deployed pipeline.
select_by_aspect_elev_bins.py	4.6.1	Method A window selector by per-bin coverage.
create_n_day_blocks.py	4.6.1	5-window anchored block creation, 1 May fixed start.
create_n_block_csv_data.py	4.6.1	Wrapper that runs the per-block area, volume, and elevation aggregators.
create_n_block_area_csv_data.py	4.6.1	Per-block slush and lake area aggregation.
create_n_block_volume_csv_data.py	4.6.1	Per-block lake volume aggregation.
create_n_block_elevation_csv_data.py	4.6.1	Per-block elevation summary.
plot_mean_max_area.py	4.6.2	Annual JJA mean and maximum area, Mann-Kendall, Pettitt.
plot_mean_max_elev.py	4.6.2	Annual JJA mean and maximum elevation, Mann-Kendall, Pettitt.
plot_mean_max_volume.py	4.6.2	Annual JJA mean and maximum lake volume, Mann-Kendall, Pettitt.
run_hamed_rao_mann_kendall.py	4.6.2	Hamed-Rao variance-corrected MK across all 28 series.
plot_jja_area_anomalies.py	4.6.3	Algorithm-selected baseline window construction and per-year area anomalies.
compute_anomalies_all.py	4.6.3	Applies the selected baseline to elevation and volume metrics for cross-family comparability.
plot_era5_timeseries.py	4.6.4	Annual JJA mean and maximum ERA5 T_{2m} and $SW_{\downarrow}$.
plot_era5_r2_hysteresis.py	4.6.4	Per-AOI Pearson R^2 scatters, analog-pair flagging, lag-1 residual correlation.
rate_of_change_analysis.py	4.6.4	Trough-to-peak recovery slopes, bootstrap CIs, climate-corrected refits.
rate_of_change_per_aoi_correction.py	4.6.4	Per-AOI residual regressions for the climate-corrected slopes.
plot_table_rf_error_metrics.py	4.4.3	Validation-scene RF holdout metric tables and per-scene plot.
build_rf_confusion_matrices.py	4.4.3	Macro and per-scene confusion matrices.
plot_volume_sensitivity.py (+ _2x2.py, _bars.py)	4.5	Volume sensitivity visualisations from the ± 20 % perturbation outputs.
add_depth_band.py	4.6.5, 4.6.6	Reapplies Pope/Moussavi depth retrieval locally; produces classified-with-depth rasters.
create_30m_persistency_rasters.py	4.6.5	30 m per-class persistency rasters.
create_persistent_lake_vectors.py	4.6.5, 4.6.6	Persistent-lake polygon and point construction with buffer and min-area merge.
create_per_lake_volume_csv_data.py	4.6.6	Per-lake per-window volume, mean depth, observed pixels, observed fraction.
create_per_lake_delta_volume_csv_data.py	4.6.6	Per-lake delta-volume between consecutive observations.
analyze_drainage_events.py	4.6.6	Drainage-event detection with 40 % / 80 % thresholds, ≤ 5 window gap, chain-event flagging.
plot_30m_heatmap.py	4.6.5	30 m persistency heatmap plotting.
plot_max_melt_blocks.py	4.6.5	Annual max-melt block categorical maps.
plot_max_melt_mosaics.py	4.6.5	Annual max-melt RGB medoid mosaic plotting.
plot_lakes_by_drainage_count.py	4.6.5	Persistent-lake polygons symbolised by full-drainage event count.
plot_drainage_counts_per_year.py	4.6.6	Per-year drainage event counts (full, partial).
plot_drainage_volume_by_season.py	4.6.6	Per-year aggregate drainage volume.

D.3 CSV data

Table A4. CSV outputs of the stage-2 post-processing workflow. All files appear in the data supplement with the `csv_outputs/` path preffix.

File	Methods section	Contents
`total_summary_raw.csv`	4.6.1	Per-window AOI totals (footprint, slush, lake area, lake volume, lake count).
`footprint_summary.csv`	4.6.1	Per-window footprint area and proportion.
`select_by_apect_elev_bin_coverage.csv`	4.6.1	Per-window per-bin coverage selector.
`footprint_area_by_aspect_elev_bins.csv`	4.6.1	Per-window footprint area per bin.
`slush_area_by_aspect_elev_bins.csv`	4.6.1	Per-window per-bin slush and lake area.
`lake_area_*`*above*	4.6.1	*see above*
`lake_volume_by_aspect_elev_bins.csv`	4.6.1	Per-window per-bin lake volume.
`projected_*`*above*`.csv`	4.6.1	Per-bin and per-AOI projected (scaled) and totalled area and volume.
`total_*`*above*`.csv` (8 files)	4.6.1	*see above*
`5_window_block/*.csv` (15 files)	4.6.1	Per-block aggregates of slush area, lake area, lake volume, elevation, plus selector and projected variants.
`ERA5Land_T2m_SWdown_OST_PTM_2013_2025_MaySep.csv`	4.1, 4.6.4	Per-AOI daily ERA5-Land T_{2m} and $\mathrm{SW}_{\downarrow}$.
`ERA5Land_T2m_SWdown_ElevBins_OST_PTM_2013_2025_MaySep.csv`	4.1, 4.6.4	Per-aspect-elevation-bin ERA5-Land.
`timeseries/area_jja_summary.csv`	4.6.1, 4.6.2	Annual JJA mean and maximum per AOI for each family.
`timeseries/elev_jja_summary.csv`	4.6.1, 4.6.2	*see above*
`timeseries/volume_jja_summary.csv`	4.6.1, 4.6.2	*see above*
`timeseries/area_mann_kendall.csv`	4.6.2	Mann-Kendall τ, p, Sen slope per series.
`timeseries/elev_*`*above*	4.6.2	*see above*
`timeseries/volume_*`*above*	4.6.2	*see above*
`timeseries/area_pettitt.csv`	4.6.2	Pettitt K, change-point year, p per series.
`timeseries/elev_*`*above*	4.6.2	*see above*
`timeseries/volume_*`*above*	4.6.2	*see above*
`timeseries/hamed_rao_mk_results.csv`	4.6.2	Hamed-Rao variance-corrected MK per series.
`timeseries/area_jja_baseline_candidates.csv`	4.6.3	Baseline-window candidates, selection, and per-year anomalies.
`timeseries/area_jja_baseline_candidates_summary.csv`	4.6.3	*see above*
`timeseries/area_jja_baseline_candidates_anomalies.csv`	4.6.3	*see above*
`timeseries/anomalies_combined_all.csv`	4.6.3	Cross-family anomaly extension (area, elevation, volume).
`timeseries/baselines_used.csv`	4.6.3	*see above*
`timeseries/obs_vs_scaled_diffs.csv`	4.6.3	*see above*
`timeseries/extreme_year_ranks_top3.csv`	4.6.3	*see above*
`timeseries/era5_jja_mean_max_summary.csv`	4.6.4	Annual JJA mean and max ERA5 predictors per AOI.
`timeseries/era5_r2_summary.csv`	4.6.4	Per-AOI and pooled Pearson R^2 for each climate–melt-response pair.
`timeseries/era5_r2_pooled_summary.csv`	4.6.4	*see above*
`timeseries/era5_hysteresis_analog_pairs.csv`	4.6.4	Flagged analog pairs.
`timeseries/era5_hysteresis_lag_corr.csv`	4.6.4	Lag-1 residual correlation per AOI-metric.
`timeseries/era5_rate_of_change_cycles.csv`	4.6.4	Trough-to-peak cycles and climate-corrected slopes.
`timeseries/era5_rate_of_change_cycles_candidates.csv`	4.6.4	*see above*
`timeseries/rate_of_change_per_aoi_models.csv`	4.6.4	*see above*
`timeseries/rate_of_change_per_aoi_cycles.csv`	4.6.4	*see above*
`volume_sensitivity/{ost,ptm}_sensitivity_g_Ad.csv`	4.5	$\pm 20\,\%$ perturbation outputs for g and A_d on six representative lakes.
`rf_error_metrics/rf_holdout_metrics_by_validation_scene.csv`	4.4.3	Per-scene and aggregate holdout metrics and confusion matrices.
`rf_error_metrics/rf_confusion_per_scene.csv`	4.4.3	*see above*

Table A4 continued.

File	Methods section	Contents
`rf_error_metrics/rf_confusion_macro.csv`	4.4.3	*see above*
`drainage_events/drainage_events.csv`	4.6.6	Drainage-event records (full ≥ 80 %, partial 40 to 80 %).
`drainage_events/per_lake_per_window.csv`	4.6.6	Lake-id by window status table.
`drainage_events/per_lake_volume.csv`	4.6.6	Per-lake per-window observed volume, depth, and observability.
`drainage_events/per_lake_mean_depth.csv`	4.6.6	*see above*
`drainage_events/per_lake_obs_pixels.csv`	4.6.6	*see above*
`drainage_events/per_lake_obs_fraction.csv`	4.6.6	*see above*
`per_lake_delta_volume_OST.csv`	4.6.6	Per-lake delta-volume between consecutive observations.
`per_lake_delta_volume_PTM.csv`	4.6.6	*see above*
`deepwater_rinf_lookuptables/Rinf_LUT_{AOI}_L8L9_v1.csv`	4.5	Per-AOI R_∞ lookup table for $B4$ and $B8$.

D.4 Vector products (shapefiles)

Table A5. Shapefile products used as inputs or generated as outputs of the methods pipeline.

File	Methods section	Contents
`aoi/PTM_AOI_1500m.shp`, `OST_AOI_1500m.shp`	4.1	AOI polygons capped at 1500 m, fjord margins redrawn, nunataks excluded.
`aoi/PTM_elevation_bins.shp`, `OST_elevation_bins.shp`	4.6.1	100 m elevation-band shapefiles per AOI.
`aoi/PTM_aspect_elevation_bins.shp`, `OST_aspect_elevation_bins.shp`	4.6.1	Aspect-subdivided elevation bins for the five largest bands per AOI.
`aoi/PTM_1000m_bisector.shp`, `OST_1000m_bisector.shp`	4.6.1	Aspect-bisector polygons derived from a per-pixel DEM aspect calculation in ArcGIS Pro and manually adjusted to follow the principal flow divide.
Per-window vector exports: `{AOI}_TEST_GEE_volume_v6_vectors/{footprint,slush,lake}.shp` (3803 files across both AOIs)	4.4.1, 4.5, 4.6.1	Per-window classified vector outputs with lake area, lake volume, mean depth, and lake-bed albedo proxies attached as attributes.
`blocks/5_window/all_{AOI}_files_anchored/` (5-window block shapefile collection)	4.6.1	Block-aggregated per-AOI slush, lake, and footprint shapefiles for the 1 May anchored 5-window block scheme.
`drainage/persistent_lakes_shapefiles/{AOI}_persistent_lake_polygons.shp`, `{AOI}_persistent_lake_points.shp`	4.6.5, 4.6.6	Per-AOI persistent-lake polygons (57 at Ptm., 46 at Ost.) and centroid points.
`drainage/persistent_lakes_shapefiles/drainage_events_points.shp`, `per_lake_per_window_points.shp`	4.6.6	Per-event and per-lake-per-window point vector outputs for drainage detection.

D.5 Raster products

Table A6. Raster products used as inputs or generated as outputs of the methods pipeline.

File	Methods section	Contents
MEaSUREs Greenland Ice Mapping Project DEM, 30 m (Howat et al., 2014)	4.1, 4.3.1, 4.4.1, 4.6.1, 4.6.1	Elevation reference for the 1500 m AOI cap, per-feature elevation attributes, slope-mask derivation, and per-bin elevation binning.
Earth Engine asset collections `projects/.../ClassifiedMosaics/{AOI}{YEAR}/` (per-window classified rasters)	4.4.1, 4.5, 4.6.5	Per-window 4-band rasters: classification, A_d^{B4}, A_d^{B8}, mosaic_footprint. 30 m, EPSG:3995.

Table A6 continued.

File	Methods section	Contents
`raster_data/with_depth_band/all_{AOI}_classified_depth_rasters/`	4.6.5, 4.6.6	Per-window classified-with-depth rasters lifted from Earth Engine for local raster operations.
`raster_data/30_persistency_rasters/{prefix}_{lake,slush,combined}_persistency.tif`	4.6.5	Per-class persistency rasters at 30 m.
`figures/plot_max_melt_blocks/` (12 categorical PNGs)	4.6.5	Annual maximum-melt 5-window block categorical maps per AOI.
`figures/plot_max_melt_mosaics/` (12 RGB PNGs)	4.6.5	Annual maximum-melt-block RGB medoid mosaics per AOI.

E Scaling sensitivity

The deployed processing chain produces two annual time-series products. The first is *observed*, the direct per-window aggregate of classified slush and lake area within the AOI footprint. The second is *scaled*, the observed value plus an aspect-elevation-bin-resolved projection (`project_melt_area_by_aspect_elev_bins.py`) that fills the unobserved portion of the AOI within each window. Observed values are reported as primary throughout Section 5 because they carry the smaller modelling-assumption load. This appendix documents the methodology of the scaled processing chain and summarises the comparison between the two processings.

E.1 Coverage-correction methodology

Each AOI is split into 100 m elevation bands derived from the MEaSUREs DEM. The five largest elevation bands per AOI are sub-divided along an aspect-bisector polygon into northwest and northeast facing sub-units, the bisector derived from a per-pixel aspect calculation from the MEaSUREs DEM and then manually adjusted to follow the principal flow divide of each AOI. The lower elevation bands are not split because their per-bin pixel counts do not support a stable per-aspect estimate. The resulting aspect-elevation bins are the spatial units used for the coverage-corrected scaling described below.

Two parallel processing sets of the per-window slush, lake, and lake-volume products are produced, mirroring the "raw" and "scaled" treatment introduced by Williamson et al. (2018) and adopted by Dell et al. (2022) for Antarctic ice shelves. The observed processing set reports, per window and per bin, the direct sum of pixels classified as slush or lake within the visible footprint. The scaled processing set additionally projects, per aspect-elevation bin, the per-bin observed wet density onto the non-visible portion of the bin, so that

$$\text{area}_{\text{scaled},b} = \text{area}_{\text{observed},b} \cdot \frac{A_{b,\text{total}}}{A_{b,\text{visible}}}$$

when the per-bin visible fraction exceeds the per-bin selector threshold. Per-AOI scaled area and volume are the sum of per-bin scaled values across bins. Elevation summaries are reported in observed form only because elevation is a per-polygon attribute rather than a per-bin density and is not amenable to the same projection step.

E.2 Comparison summary

The largest absolute divergence between the two processings occurs for the Petermann combined-maximum area series in 2023 (observed 1227 % versus scaled 907 % relative to the algorithm-selected baseline of Section 4.6.3). The equivalent Ostenfeld divergence at maximum is below 10 percentage points. Across the 12 years the mean observed-scaled gap for Petermann combined-max area is 75 percentage points, with a maximum gap of 320 percentage points at Petermann 2023. At Ostenfeld every metric has a mean processing gap below 6 percentage points. The processing choice therefore matters most for the Petermann headline magnitudes, while the Ostenfeld headlines and the qualitative findings at both AOIs are processing-invariant.

Direction consistency is high. Across the 144 metric × AOI × year cells in Section 5.5, the observed and scaled processings produce the same sign in 135 of 144 cells (93.75 %). The 9 sign flips are listed in Table A7. All occur at small absolute anomaly (max |value| = 17.8 %) and none crosses the 50 % or ×2 thresholds used to flag headline anomalies.

Full per-year scaled values for all area, volume, and anomaly metrics are stored in the CSV outputs listed in Appendix D.3 (`projected_*`, `5_window_block/` projected variants, `timeseries/obs_vs_scaled_diffs.csv`).

Table A7. Observed–scaled sign flips across the 144 metric × AOI × year cells in Section 5.5. All flips occur at small absolute anomaly (max |value| = 17.8%) and none crosses the 50% / ×2 thresholds used to flag headline anomalies. Direction-consistency is 135/144 cells (93.75%).

Family	Metric	AOI	Year	Observed (%)	Scaled (%)
Area	combined_mean	Ost	2018	+3.18	−0.48
Area	combined_mean	Ost	2020	+0.26	−5.73
Area	combined_max	Ptm	2016	+17.82	−0.35
Area	slush_max	Ptm	2016	+11.93	−6.03
Area	slush_max	Ptm	2024	+44.39	−3.36
Volume	lake_max	Ptm	2019	+4.71	−1.26
Volume	lake_mean	Ost	2018	+3.28	−2.67
Volume	lake_mean	Ost	2023	+5.80	−1.83
Volume	lake_mean	Ptm	2024	+9.24	−3.87